

NUMERICAL MODELING AND ANALYSES OF ANISOTROPIC DIFFUSION
AND STRESSES IN POLYMER ELECTROLYTE FUEL CELL

A THESIS SUBMITTED TO
THE GRADUATE SCHOOL OF NATURAL AND APPLIED SCIENCES
OF
MIDDLE EAST TECHNICAL UNIVERSITY



BY

MEHDI MEHRTASH

IN PARTIAL FULFILLMENT OF THE REQUIREMENTS
FOR
THE DEGREE OF DOCTOR OF PHILOSOPHY
IN
MECHANICAL ENGINEERING

AUGUST 2017

Approval of the thesis:

**NUMERICAL MODELING AND ANALYSES OF ANISOTROPIC
DIFFUSION AND STRESSES IN POLYMER ELECTROLYTE FUEL CELL**

submitted by **MEHDI MEHRTASH** in partial fulfillment of the requirements for
the degree of **Doctor of Philosophy in Mechanical Engineering Department,**
Middle East Technical University by,

Prof. Dr. M. Gülbin Dural Ünver
Dean, Graduate School of **Natural and Applied Sciences**

Prof. Dr. Raif Tuna Balkan
Head of Department, **Mechanical Engineering**

Prof. Dr. İlker Tari
Supervisor, **Mechanical Engineering Dept., METU**

Examining Committee Members:

Prof. Dr. Derek K. Baker
Mechanical Engineering Dept., METU

Prof. Dr. İlker Tari
Mechanical Engineering Dept., METU

Prof. Dr. Ayhan Yılmazer
Nuclear Engineering Dept., Hacettepe University

Prof. Dr. Serhat Yeşilyurt
Mechatronics Engineering, Sabanci University

Asst. Prof. Dr. Kerem Bayar
Mechanical Engineering Dept., METU

Date: 23.08.2017



I hereby declare that all information in this document has been obtained and presented in accordance with academic rules and ethical conduct. I also declare that, as required by these rules and conduct, I have fully cited and referenced all material and results that are not original to this work.

Name, Last name : MEHDI MEHRTASH

Signature :

ABSTRACT

NUMERICAL MODELING AND ANALYSES OF ANISOTROPIC DIFFUSION AND STRESSES IN POLYMER ELECTROLYTE FUEL CELL

Mehrtash, Mehdi

Ph.D., Department of Mechanical Engineering

Supervisor: Prof. Dr. İlker Tari

August 2017, 118 pages

A two dimensional, half-cell, non-isothermal, multi-phase model of a polymer electrolyte fuel cell (PEFC) is developed. The model accounts for the acting clamping force on the cell with accompanying effects on gas transport properties and contact resistances. Spatial variations of anisotropic structural and physical properties of gas diffusion layers (GDLs) in both in-plane and through-plane directions are considered. The developed mechanistic model is validated by comparing its results with the experimental data for voltage-current characteristics and channel-rib current density distribution for the first time in literature. Significant changes are observed in local gas and water concentrations as well as current density profiles with respect to cell compression and humidity ratios of entrant gases. Compression exacerbates the liquid saturation under the rib as a consequence of porosity and permeability reduction. Under compression, phase change rate increases in the cell; degree of supersaturation under the channel escalates leading to a higher condensation rate while degree of undersaturation under the rib increases leading to a higher evaporation rate.

Low durability of membranes is one of the major barriers for wide spread commercialization of PEFCs. The swelling effect on durability is one of the key challenges for the fabrication of the catalyst-coated membrane at the heart of the PEFC. Presented in this study were three main contributions that provide insight into the probable locations of failure in the membrane under hygrothermal cycle and external applied force, and the realistic conditions where a combination of both these loadings were applied. Mechanical response of the membrane, subjected to conjugate hygro-thermo-mechanical loadings are observed during fuel cell operation. The effects of different operating parameters as well as individual contributing factors on the local stresses induced in the membrane are identified.

Keywords: Polymer electrolyte fuel cell; Clamping force; Effective diffusivity; Local current distribution; Phase change rate; Liquid water saturation; Nafion; Hygrothermal cycling; Mechanical degradation; Elasto-plasticity

ÖZ

POLİMER ELEKTROLİT YAKIT HÜCRESİNDE ANİZOTROPİK DİFÜZYON VE STRESLERİN SAYISAL MODELLEMESİ VE ANALİZLERİ

Mehrtash, Mehdi

Doktora, Makina Mühendisliği Bölümü

Tez Yöneticisi: Prof. Dr. İlker Tarı

Ağustos 2017, 118 sayfa

İki boyutlu, yarı hücreli, izotermal olmayan, çok fazlı bir polimer elektrolit yakıt hücresi modeli (PEFC) geliştirildi. Model, hücreye uygulanan sıkıştırma kuvvetinin gaz taşıma özellikleri ve temas direnci üzerine etkilerini hesaba katmaktadır. Gaz difüzyon katmanlarının (GDL'ler) anizotropik yapısal ve fiziksel özelliklerinin hem düzlem içi hem de düzlem yönündeki uzaysal değişimleri göz önüne alınmaktadır. Geliştirilen mekanistik model, literatürde ilk kez, elde edilen sonuçlar voltaj-akım karakteristikleri ve kanal-kaburga akım yoğunluğu dağılımı için olan deneysel verilerle karşılaştırılarak doğrulanmıştır. Hücre sıkıştırma kuvveti ve giren gazların nem oranlarına göre yerel gaz ve su konsantrasyonlarında ve akım yoğunluğu profillerinde önemli değişiklikler gözlenmiştir. Gözeneklilik ve geçirgenlik azalmasının sonucu olarak sıkıştırma kaburga altındaki sıvı doymamışlığını artırır. Sıkıştırma altında faz değişim hızı hücrede artar; kanal altındaki aşırı doygunluk derecesi artarak yoğunlaşma oranının yükselmesine neden olurken, kaburga altındaki doymamışlık derecesi artarak buharlaşma oranının yükselmesine neden olur.

Membranların düşük dayanıklılığı, PEFC'lerin geniş çapta ticarileşmesinin önündeki başlıca engellerden biridir. Dayanıklılık üzerindeki şişme etkisi, PEFC'nin kalbindeki katalizör kaplı membran imalatı için en önemli zorluklardan biridir. Bu çalışmada, higrotermal döngü ve uygulanan dış kuvvet altında ve bu yüklemelerin bir kombinasyonunun uygulandığı gerçekçi koşullar altında, membranda hasara uğraması olası yerlerle ilgili bilgi sağlayan üç temel katkı sunulmuştur. Yakıt hücresi çalışması sırasında eşlenik higro-termo-mekanik yüklemelere maruz bırakılan membranın mekanik tepkisi gözlemlenmiştir. Farklı çalışma parametrelerinin etkilerinin yanı sıra membranda indüklenen yerel streslere bireysel katkıda bulunan faktörler tanımlanmıştır.

Anahtar Kelimeler: Polimer elektrolit yakıt hücresi; Sıkıştırma kuvveti; Etkin difüzyon; Lokal akım dağılımı; Faz değişim oranı; Sıvı su doygunluğu; Nafyon; Higrotermal döngü; Mekanik degradasyon; Elasto-plastisite



To My Family

ACKNOWLEDGMENTS

I would like to express my gratitude to Prof. Dr. İlker Tarı and Prof. Dr. Serhat Yeşilyurt for their support and supervision throughout this study.

I would like to express my deepest appreciation to my family and friends for their love, support and faith in me.

I gratefully acknowledge the financial support provided by TUBITAK through BİDEB 2215 Scholarship program.



TABLE OF CONTENTS

ABSTRACT.....	v
ÖZ	vii
ACKNOWLEDGMENTS	x
TABLE OF CONTENTS	xi
LIST OF TABLES	xiv
LIST OF FIGURES	xv
LIST OF SYMBOLS	xviii
CHAPTERS	
1 INTRODUCTION	1
1.1 PEFC components	2
1.1.1 Polymer electrolyte.....	2
1.1.2 Catalyst layer.....	3
1.1.3 Gas diffusion layer	3
1.1.4 Bipolar plate	3
1.2 Fundamentals of PEFC	4
1.2.1 Working principles	4
1.2.2 Thermodynamics	5
1.2.3 Kinetics.....	6
1.2.4 PEFC overpotentials.....	7
1.3 Transport in PEFC	8
1.3.1 Mass transport in porous media.....	8
1.3.2 Multiphase transport in porous media	10
1.3.3 Charge transport	13
1.3.4 Heat generation and transport.....	14
1.4 Polymer electrolyte degradation	15
1.4.1 Chemical degradation.....	15
1.4.2 Mechanical degradation	16
1.4.3 Thermal degradation.....	17

1.4.4	Hygroscopic swelling	17
1.4.5	Combined degradation	18
2	LITERATURE REVIEW	19
2.1	Physical properties and characterization in GDLs	19
2.2	Compression impacts on multiphase flow in GDL	25
2.3	Polymer electrolyte degradation	29
3	EXPERIMENTAL STUDY ON PERFORMANCE EVALUATION OF PEFC UNDER CLAMPING TORQUE	35
3.1	Assembly method	35
3.2	Pressure distribution	36
3.3	Voltage-current and power-current curves	38
3.4	Results and discussions	38
4	CHANNEL-RIB MULTIPHYSICS MODEL	41
4.1	Model description	41
4.2	Governing equations	43
4.2.1	Transport of gas species in GDMs	43
4.2.2	Transport of energy	44
4.2.3	Conservation of charge	45
4.2.4	Transport of water in the membrane	46
4.2.5	Transport of liquid water	46
4.2.6	Deformation	48
4.3	Boundary conditions	48
4.3.1	Mass fractions in the Maxwell-Stefan equation	48
4.3.2	Conservation of charge	49
4.3.3	Conservation of membrane water	50
4.3.4	Deformation	50
4.4	Parameters	51
4.4.1	Physical properties and base operating conditions	51
4.4.2	Mechanical properties	52
4.4.3	Effective diffusivity and permeability	57
4.4.4	Contact resistance	59
4.4.5	Reaction kinetics	59
4.5	Numerical approach	61

5	RESULTS AND DISCUSSIONS	63
5.1	Preliminary results	63
5.1.1	Force field.....	63
5.1.2	Porosity distribution	64
5.1.3	Permeability distribution	65
5.1.4	In-plane and through-plane effective relative diffusivity distributions.....	66
5.1.5	Temperature distribution in an operating cell	68
5.1.6	Water distribution in an operating cell	69
5.1.7	Concentration distribution	70
5.1.8	Liquid water distribution	72
5.2	Parameter sensitivity analyses	72
5.3	Model validation	79
5.4	Influence of operating parameters on local performance	82
5.4.1	Effect of compression on porosity and effective relative diffusivity distributions.....	82
5.4.2	Effect of compression on in-plane local properties.....	83
5.4.3	Effect of inlet relative humidity on local cell performance.....	86
5.4.4	Effect of compression on liquid water formation.....	87
5.4.5	Effect of liquid water flooding on cell performance	89
5.5	Influence of operating parameters on membrane's local mechanical degradation	90
5.6	Effect of clamping force	91
5.7	Effect of the load current	94
5.8	Effect of inlet relative humidity.....	96
6	CONCLUSION	103
6.1	Concluding remarks.....	103
6.2	Future work.....	105
	REFERENCES.....	107
	CURRICULUM VITAE	117

LIST OF TABLES

TABLES

Table 1 Summary of studies done to estimate the effective diffusivity of the GDLs.	23
Table 2 Summary of governing equations.	43
Table 3 Source terms used in the governing equations.	45
Table 4 Physical properties and base operating conditions.	51
Table 5 Young's modulus values at various temperatures and relative humidities for Nafion 112 [58].	53
Table 6 Physical properties of different cell components.	55
Table 7 Parameters in kinetic and agglomerate models [35,36].	60
Table 8 Simulation cases for the analyses on the effect of different parameters on the mechanical degradation.	91

LIST OF FIGURES

FIGURES

Figure 1 Working principle diagram of PEFC.....	5
Figure 2 Polarization curve for PEFC illustrating the contributions of each charge transfer polarization [2].....	7
Figure 3 GDL representation using (a) pore network model, (b) stochastic model and (c) X-ray computed tomography (adapted from [6]).	20
Figure 4 Disassembled components of the tested fuel cell.	36
Figure 5 Test setup for experiments on PEFC.	37
Figure 6 Pressure distribution results over the pressure films. From the left to right the torques applied on the cell are 5, 10 and 15 Nm.	38
Figure 7 (a) Performance curves and (b) power curves at three different applied torques.	39
Figure 8 Schematic of the computational domain created based on [2].	42
Figure 9 Compressive strain in terms of compressive stress given in [2].....	56
Figure 10 Effective relative diffusivity as a function of porosity for TGP-H-060 (adapted from [5]).	58
Figure 11 Cell configuration under compressive force (a) obtained from simulation and (b) given in [2].....	64
Figure 12 Porosity distribution in the GDMs.....	65
Figure 13 Permeability contour in GDMs (m^2).....	66
Figure 14 (a) In-plane and (b) through-plane effective relative diffusivity distributions.	67
Figure 15 Temperature contour (K) [$I=1.2 \text{ A/cm}^2$, $\text{RH}_c=0.6$, $\text{RH}_a=0.4$].....	68
Figure 16 Water concentration distribution in a sample operating cell (mol/m^3). ...	69
Figure 17 Hydrogen mass fraction distribution in anode.....	71
Figure 18 Oxygen mass fraction distribution in the cathode.	71

Figure 19 Liquid water distribution in the cathode GDM.	72
Figure 20 Polarization curves for different inlet pressures at anode and cathode.	74
Figure 21 Polarization curves for different cell operating temperatures.	74
Figure 22 Polarization curves for various inlet humidification conditions.	75
Figure 23 Polarization curves for different porosity values assumed in GDL and MPL.	76
Figure 24 Polarization curves for different permeability values assumed in GDL and MPL.	76
Figure 25 Performance comparison between cases with anisotropic effective relative diffusion and Bruggeman assumption assumed in GDLs.	78
Figure 26 Performance curves for different cases of diffusivities in GDLs.	78
Figure 27 (a) Performance curves and (b) in-plane current density distributions for different current loads and comparison with experimental data [1,2]. The in-plane current density distribution is probed at the membrane-GDM interface in the anode side ($RH_c=RH_a=0.4$).	81
Figure 28 Porosity (lines), in-plane (dashed lines) and through-plane (dotted lines) effective relative diffusivity distributions for three different compression cases. Data are extracted over the mid-plane section of GDL.	82
Figure 29 In-plane oxygen mass fraction distribution for three different current loads with and without compression ($I=0.75 \text{ A/cm}^2$, $RH_c=0.7$, $RH_a=0.4$).	84
Figure 30 In-plane current density and phase change rate distributions for the case with compression (normal lines) and the case free from compression (dashed lines) ($I=0.75 \text{ A/cm}^2$, $RH_c=0.7$, $RH_a=0.4$).	85
Figure 31 In-plane current distribution for different air stream relative humidities ($I=0.65 \text{ A/cm}^2$, $RH_a=0.4$, compression ratio=35%).	86
Figure 32 Compression effect on liquid water saturation and phase change rate distribution in cathode GDM ($I=0.75 \text{ A/cm}^2$, $RH_c=0.7$, $RH_a=0.4$, compression ratio=35%).	88
Figure 33 Liquid water generation effects on cell performance.	89
Figure 34 (a) Strain distribution along the membrane's interface with cathode and (b) von Mises stress distribution in the membrane for study cases 1-3.	93

Figure 35 (a) Local current density distribution and (b) strain distribution along the membrane's interface with cathode for different operating current loads. 95

Figure 36 (a) Water distribution in the cell and (b) in-plane strain distribution along the membrane's interfaces with the cathode and anode for the study case 7..... 98

Figure 37 (a) Water distribution in the cell and (b) in-plane strain distribution along the membrane's interfaces with the cathode and anode for study case 8. 99

Figure 38 (a) Water distribution in the cell and (b) in-plane strain distribution along the membrane's interfaces with the cathode and anode for study case 9. 100



LIST OF SYMBOLS

<i>A</i>	area, m ²
<i>a</i>	water activity
<i>c</i>	concentration, mol m ⁻³
<i>c_p</i>	specific heat, J kg ⁻¹ K ⁻¹
<i>D</i>	diffusivity, m ² s ⁻¹ , diameter, m
\underline{D}	elasticity matrix
<i>E</i>	Young's modulus, MPa
<i>EW</i>	equivalent weight, kgmol ⁻¹
<i>F</i>	Faraday's constant, Cmol ⁻¹ , force, kg m s ⁻²
<i>G</i>	shear modulus, MPa
<i>H</i>	Henry's constant, Pa m ³ mol ⁻¹
<i>h</i>	mass transfer coefficient, m s ⁻¹ ; enthalpy of vaporization, J kg ⁻¹
<i>J</i>	current density, A cm ⁻²
<i>j</i>	reaction rate, A cm ⁻²
<i>K</i>	permeability, m ²
<i>k</i>	thermal conductivity, W m ⁻¹ k ⁻¹ ; rate constant, s ⁻¹
<i>l</i>	length, m
<i>N</i>	number of bolts
<i>n_d</i>	electro-osmotic drag coefficient, H ₂ O per H ⁺
<i>P</i>	pressure, atm
<i>R</i>	universal gas constant, J mol ⁻¹ K ⁻¹
<i>r</i>	radius
RH	relative humidity
<i>S</i>	source term; deviatoric stress tensor
<i>s</i>	liquid water saturation
<i>Sh</i>	Sherwood number
<i>T</i>	temperature, K; torque, N m

u	velocity, m s^{-1}
w	mass, kg; displacement vector
$wt\%$	wettability
x	molar fraction

Greek symbols

α	charge transfer coefficient; coefficient of thermal expansion, K^{-1}
δ	thickness, m; Kronecker delta
ε	porosity
λ	membrane water content, mol m^{-3}
ν	stoichiometric factor
σ	electric conductivity, S m^{-1} ; surface tension, N m^{-1} ; stress, MPa
μ	dynamic viscosity, $\text{kg m}^{-1} \text{s}^{-1}$, friction coefficient
η	overpotential, V
ϕ	electric potential, V
ϵ	strain
ξ	x component of displacement vector
ζ	y component of displacement vector
ψ	shear stress, MPa
ν	Poisson's ratio
ϑ	molar volume of species, $\text{m}^3 \text{mol}^{-1}$
ρ	density, kg m^{-3}
τ	tortuosity
θ	contact angle, $^\circ$

Subscripts

a	anode
act	activation
b	bolt
c	capillary; cathode

<i>ch</i>	channel
clamp	clamping
<i>cond/evp</i>	condensation/evaporation
<i>cr</i>	contact resistance
<i>e</i>	electronic charge
<i>eff</i>	effective value in the porous region
<i>el</i>	elastic
<i>eq</i>	equilibrium
<i>f</i>	force, yield function
<i>g</i>	gas phase
<i>i</i>	species index
<i>ip</i>	in-plane direction
<i>j</i>	species index
<i>kk</i>	volumetric
<i>l</i>	liquid phase
<i>lg</i>	phase transfer between liquid and gas
<i>m</i>	ionic phase; mass; membrane
<i>mix</i>	mixture
<i>ohm</i>	ohmic
<i>pell</i>	pellet
<i>pl</i>	plastic
<i>rev</i>	reversible
<i>s</i>	solid phase
<i>sat</i>	saturation
<i>sw</i>	swelling
<i>th</i>	thermal
<i>tp</i>	through-plane direction
<i>xx</i>	x direction
<i>yy</i>	yy direction
<i>wv</i>	water vapor
<i>0</i>	standard temperature, 298.15 K and pressure, 101.325 kPa

superscripts

<i>l</i>	liquid phase
<i>Naf</i>	Nafion
<i>ox</i>	oxidation
<i>rd</i>	reduction
<i>ref</i>	reference value
<i>Y</i>	yield





CHAPTER 1

INTRODUCTION

Fuel cells and hydrogen technologies are the favorable path in progressively evolving sustainable energy systems. They offer zero emission power generation to be used in our daily life, from transportation to manufacturing applications. However, transition from formerly used technologies to these advanced technologies is not an easy task.

For the automotive applications, polymer electrolyte fuel cell (PEFC) is considered as the best option due to its low operating temperature and high efficiency. PEFC, despite several advantages compared to conventional power sources, has some challenges hindering its commercialization. In addition, especially PEFC deployment in automotive industry is a challenging task due to durability, reliability and economic constraints while the internal combustion engines have been developed for more than a century and excelled in these. Currently, a better understanding of basic interactions as well as water management in the PEFC system is required for improving the system in terms of durability and reliability.

A large number of studies exploring the transport phenomena in PEFC exists in literature. There are also several structural models of PEFCs. However, studies combining these two aspects with all related details are limited. Coupling these two essential aspects, which is one of the goals of this study, can give us the opportunity to investigate how they interact and influence each other during cell operation in a way cannot be achieved by experimental studies.

Another objective in this study is to illustrate the conjugate hygro-thermo-mechanical influences on membrane of an operating fuel cell under cyclic changes.

Inhomogeneous compression force as well as spatial hydration and temperature gradients in the cell induce a non-uniform mechanical degradation. Knowing the individual contributions to the total degradation and also the locations of the hotspots can help us design a durable cell.

The developed PEFC numerical model is based on the experimental study performed by Reum et al. [1]. In this chapter, the details of a typical PEFC construction and operation are given together with the involved phenomena and the related governing equations used in the numerical model. The information presented here forms a background for the literature review in Chapter 2.

1.1 PEFC components

A typical PEFC is composed of a membrane, catalyst layers, gas diffusion layers and bipolar plates. In this section, each component of a cell will be described in terms of structure and functionality.

1.1.1 Polymer electrolyte

Commonly used membrane in PEFC is produced by DuPont with the name Nafion which is a perfluorinated copolymer. While it is an ion conductor, it resists electrons to pass through. It also separates the supplied hydrogen and oxygen in anode and cathode sides, respectively. The sulfonic acid groups ($SO_3^-H^+$) are the fixed charge sites on polytetrafluoroethylene (PTFE) polymer chains in Nafion. The weight of the polymer per sulfonic acid group is defined as the equivalent weight (EW) of the membrane. The charge site concentration is expressed as

$$c_{SO_3^-} = \frac{\rho}{EW} \quad (1)$$

where ρ is the dry density of Nafion. Water in the membrane combines with the protons and form hydroniums, H_3O^+ , which are mobile in the electrolytes. Therefore, the conductivity of the polymer electrolyte is in direct relation with its water content. Increasing the water content improves the charge mobility of the membrane.

1.1.2 Catalyst layer

Catalyst layers (CLs) are used in both electrodes to promote the electrochemical reactions. They are usually coated over the membrane. These layers are composed of carbon particles impregnated with electrolyte to improve the proton conductivity. Since they are saturated with the electrolyte their electric resistance is high thus the minimum thickness for the CL is desirable. Typical thickness of the CL is about 10 to 30 μm . From the cost stand point, it is desirable to minimize the catalyst loadings in CLs.

1.1.3 Gas diffusion layer

Gas diffusion layers (GDLs) are responsible for multiple tasks. The most important one is to ease the access of the reactant gases to the catalyst layers and also the removal of product water from the active sites. They are also created in such a way to be conductive for electric charge and heat, developing a homogenized current density in channel-rib scale. GDLs are made of carbon fibers randomly dispersed as a fiber paper or woven as carbon cloth. Due to the orientation of fibers, these layers are highly anisotropic in every aspect such as mechanical stability, electrical conductivity and heat transport. In order to improve the water removal capability of these layers, they are impregnated with PTFE that adds a hydrophobic nature to the structure. Also in some cases, an additional micro porous layer (MPL) is deposited on GDL.

1.1.4 Bipolar plate

Bipolar plates (BPs), besides providing mechanical stability to the cell, are used to perform some additional tasks. They ensure the drain of electrons and dissipation of heat from the inner cell. They have to be impermeable, chemically stable and have good electrical conductivity. Their layout also influences the distribution of reactants and accordingly the operating parameters and resulting current distribution at channel-rib scale. Furthermore, in a stack, the BP is working as a component for connecting the single membrane electrode assemblies (MEAs).

1.2 Fundamentals of PEFC

1.2.1 Working principles

In Figure 1, a schematic of PEFC, which is composed of BPs, GDLs, CLs and membrane (MEM) is presented along with its working principles throughout the cell. Reactant gases are supplied to the anode side pass through the GDL and reach the CL where they dissociate into electrons and protons. Protons cross the membrane and electrons move through the external circuit. Electrons reach the CL on the cathode side where they react with the oxygen supplied from the cathode channel and protons passed through the membrane.

PEFC is a galvanic cell where oxygen and hydrogen react and produce water in an acidic environment:



However, to keep the reaction running in the fuel cell, the gases should be provided continuously to the CLs and the product water has to be removed from the cell.

In the anode, hydrogen oxidation reaction (HOR) happens where hydrogen is oxidized as



This reaction takes place with the adsorption of hydrogen molecules at the electrode surface and formation of two protons, resulting from the breakage of the hydrogen-hydrogen bonding.

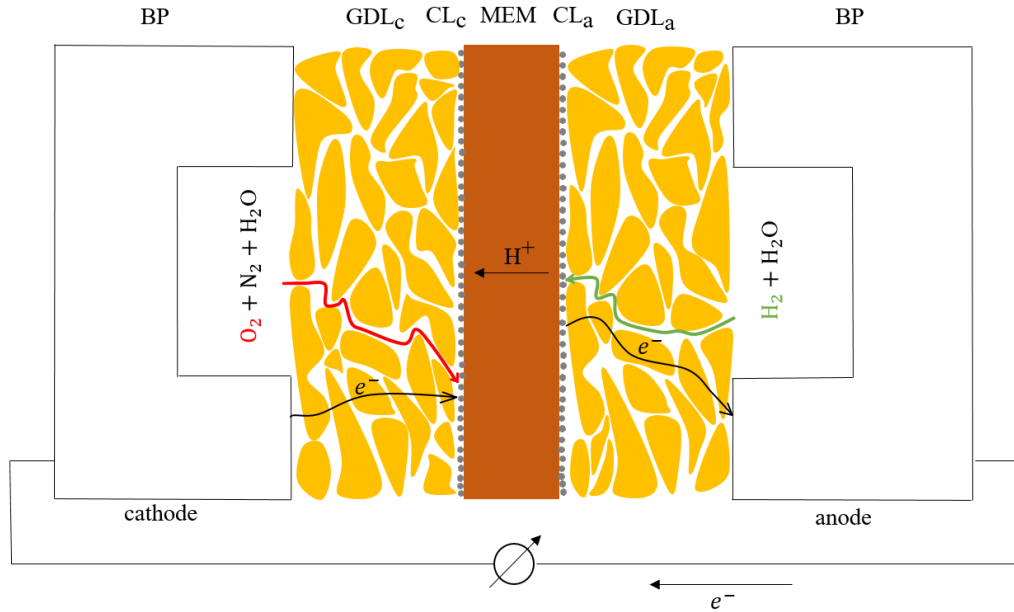


Figure 1 Working principle diagram of PEFC.

In the cathode, the oxygen reduction reaction (ORR) happens as



where the oxygen and hydrogen molecules have a reaction with electrons and produce water as a byproduct.

The CLs are usually made of platinum nanoparticles. These layers are necessary to break or make the bonding between gas molecules in both reactions (HOR and ORR).

Polymer electrolyte membrane prevents electrons to cross over while it allows protons to freely pass through. The electrons pass through an external electrical circuit, where they can be used to power electrical devices.

1.2.2 Thermodynamics

The conversion of chemical energy into electrical energy can be explained by thermodynamics. According to the first law of thermodynamics, subtracting work from the heat supplied gives the internal energy. Also, the heat added to the system itself can be described by the entropy change. Therefore, we have:

$$\Delta U = \Delta Q - \Delta W = T\Delta S - \Delta W \quad (5)$$

Gibbs free energy describes the electrical energy produced in the cell which can be obtained by subtracting the entropy change from the enthalpy change:

$$\Delta G = \Delta H - T\Delta S \quad (6)$$

The resulting standard cell voltage can be calculated from

$$E_{00} = -\frac{\Delta G}{nF} \quad (7)$$

where n is the number of moles of electrons exist in the reaction. Voltage difference between two electrodes gives the standard cell voltage. Anode electrode potential is equal to 0 V and the cathode electrode potential is equal to 1.229 V. Concentration dependency of the equilibrium cell potential is also described by the Nernst equation given as

$$E_0 = E_{00} + \frac{RT}{nF} \ln \frac{\sum_i (a_{i,products})^{v_{products}}}{\sum_i (a_{i,educts})^{v_{educts}}} \quad (8)$$

where R is the ideal gas constant, a is the activity, and v is the stoichiometric factor.

1.2.3 Kinetics

When currents are present at the electrodes the situation of distributed electrochemical equilibrium is described by electrode kinetics. There are many proposed kinetic mechanisms for each half cell reaction. The redox-reaction can be expressed as



where S_{red} is the reduced species, and S_{ox} is the oxidized species. The reaction has the forward and backward directions that are controlled by the rate constant k . The current densities for reductive and oxidative reactions are then defined as:

$$j_{ox} = -nF c_{ox} k \exp \left[-\frac{\Delta G_{act} + \alpha_a n F \eta_{act}}{RT} \right] \quad (10)$$

$$j_{red} = -nF c_{red} k \exp \left[-\frac{\Delta G_{act} - \alpha_c n F \eta_{act}}{RT} \right] \quad (11)$$

where c is the concentration of the oxidized or reduced species, ΔG_{act} is the activation energy, α is the transfer coefficient and η is the activation overpotential.

The exchange current density is defined as

$$j_0 = -nF c_{ox} k \exp \left[-\frac{\Delta G_{act}}{RT} \right] = nF c_{red} k \exp \left[-\frac{\Delta G_{act}}{RT} \right] \quad (12)$$

Combining Equations (10), (11) and (12) leads to Butler-Volmer equation:

$$j = j_{ox} + j_{red} = j_0 \left(\exp \left[\frac{\alpha_a n F}{RT} \eta_{act} \right] - \exp \left[\frac{\alpha_c n F}{RT} \eta_{act} \right] \right) \quad (13)$$

Butler-Volmer equation expresses the overall current density as a function of the electrode activation overpotential η_{act} .

1.2.4 PEFC overpotentials

When there is an electric current flow in the system, the output potential is less than the thermodynamically predicted one. Increasing the electric current drops the overall potential resulting in the current-voltage characteristics shown in Figure 2.

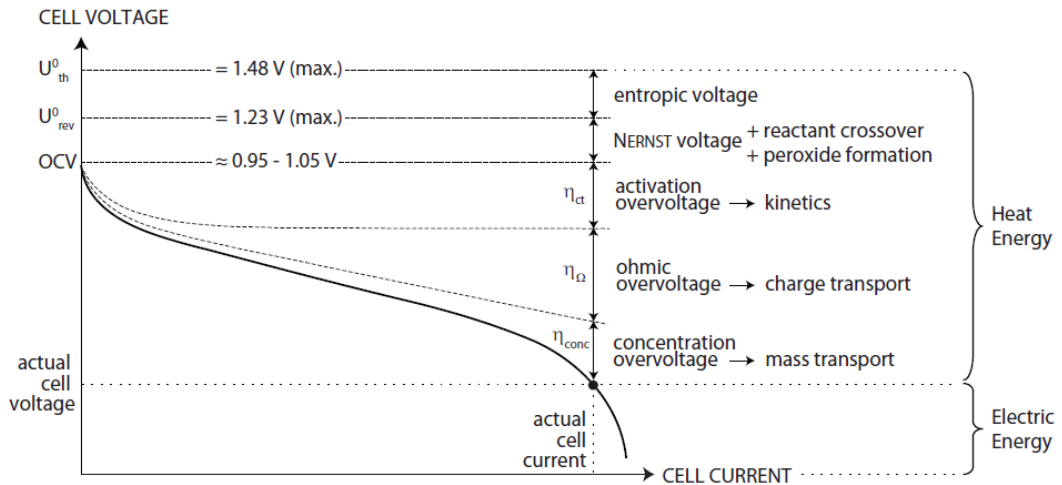


Figure 2 Polarization curve for PEFC illustrating the contributions of each charge transfer polarization [2].

There are three major overpotentials exist in the fuel cell namely the activation overpotential, ohmic overpotential and concentration overpotential. Subtracting these overpotentials from the equilibrium voltage gives the operating cell voltage:

$$U = E - \eta_{act} - \eta_{ohm} - \eta_{conc} \quad (14)$$

The activation overpotential has the dominating effect on cell voltage loss in PEFC. This process mostly happens at low current densities. This loss is attributed to the potential required to transfer the charge at both anode and cathode electrodes. The ohmic overpotential which is the second most influential loss in PEFC dominates at moderate current densities. This mode of overpotential is attributed to the electrical resistances in all components of PEFC. However, the magnitude of ionic resistance is higher compared to the electronic resistances. While the ohmic resistance in membrane depends on its water content, ohmic resistance increases linearly with current. Third potential loss mode is the concentration overpotential that dominates at high current densities due to limited reactant transport to the active sites. This can be the result of low reactant concentration in the channels or presence of liquid water over the active areas.

1.3 Transport in PEFC

In this section, the basics of transport mechanisms occurring in PEFC are summarized. The parameters and corresponding equations are also described.

1.3.1 Mass transport in porous media

GDLs, MPLs, CLs are porous materials in PEFC. The transport of reactants and products in these layers are characterized by both diffusive and convective processes. Due to existence of water and gases in the cell all domains are usually subject to two-phase flow. Gas transport from the channel to the CLs happens by both diffusion and convection driven by concentration gradient and pressure gradient, respectively. The driving force for the water which is dragged with protons crossing the membrane are concentration and pressure gradients.

1.3.1.1 Diffusive transport

This mode of transport is the dominant mode of transport in porous domains of PEFC. In continuum mechanics, relative motion of different gases can be described by diffusion. This mode of transport is governed by Fick's first law:

$$N_k = -cD_{kl}\nabla w_k = -\frac{1}{RT}D_{kl}\nabla p_k \quad (15)$$

where N_k is the mass flux vector of species k in species l , D_{kl} is the binary diffusion coefficient, w_k is the weight function and p_k is the partial pressure.

The binary diffusion coefficient is defined as follows:

$$D_{kl} = \frac{1}{p} a \left(\frac{T}{\sqrt{T_{cr,k}T_{cr,l}}} \right)^b (p_{cr,k}p_{cr,l})^{1/3} (T_{cr,k}T_{cr,l})^{5/12} \sqrt{\left(\frac{1}{M_k} + \frac{1}{M_l} \right)} \quad (16)$$

where P_{cr} and T_{cr} are the critical pressure and temperature of the gases, respectively and M is the molar mass of the mixture.

In cases where the mixture is composed of more than two species, the Maxwell-Stefan equation is generally employed as:

$$N_k = -\rho w_k \sum_{l \neq k} D_{kl,eff} \frac{M}{M_l} \left(\nabla w_l + w_l \frac{\nabla M}{M} \right) \quad (17)$$

1.3.1.2 Convective transport

The driving force in convective transport is the pressure gradient which mostly happens along the channel. Conservation of momentum for flow of an incompressible fluid can be modeled using the Navier-Stokes equation as:

$$\rho \left(\frac{\partial v}{\partial t} + v \nabla v \right) = -\nabla p + \mu \nabla^2 v \quad (18)$$

where v , p , and μ are the velocity vector, fluid pressure and dynamic viscosity, respectively. For the flow in the porous media, we can assume creeping flow with low velocity and therefore the acceleration term can be neglected leading to Darcy law as:

$$0 = -\nabla p + \mu \nabla^2 v \quad (19)$$

The fluid velocity is thus can be obtained from:

$$v = -\frac{kK}{\mu} \nabla p \quad (20)$$

where k and K represent the relative permeability and the absolute permeability, respectively.

1.3.2 Multiphase transport in porous media

The actual transport mechanism happening in PEFCs is multiphase mass transport since the water produced in cathode which passes through a porous media can be in liquid phase or vapor phase at any instant. Presence of water in normally open pores blocks the reactants to flow towards the reaction sites and reduce the cell performance causing a phenomenon which is known as flooding. Water liquid phase in PEFC flows due to several phenomena but the important ones which will be used in this thesis are:

1. Capillary action due to pressure difference between the phases.
2. Evaporation/Condensation which results in liquid removal and motion.
3. Interfacial effects which happens in the interfaces and has a significant impact over the accumulation and removal of liquid water in porous media.

In this section some of the basic parameters and relationships that are used for modeling the multiphase flow in PEFC will be discussed.

Porosity

The porous media is composed of two sections; one is the solid backbone and the other one is the void pores. The porosity of a medium is defined as the ratio of void spaces to its total volume as:

$$\varepsilon = \frac{\text{void volume}}{\text{total volume}} \quad (21)$$

Tortuosity

This parameter describes the ratio of the path between two points in a porous medium to the straight path connecting these two points. Tortuosity is generally different for in-plane and through-plane directions and should be considered separately. It is common in literature to experimentally obtain the effective relative diffusivity (porosity to tortuosity ratio) in terms of local porosity for a given porous medium under compressive clamping force.

Wettability

In the case that the void spaces of the porous media occupied with two or more fluids, one of the fluids will be absorbed on the surface stronger than the others and cause them to displace. The absorbed fluid is called wetting fluid and the displaced ones are the non-wetting phases. The solid phase generally imbibe the wetting phase while displacing the non-wetting phase. In a porous media impregnated with hydrophobic material wetting phase will be the gas and the non-wetting phase will be the water. Wetting angle is an essential parameter in the multiphase transport which affects capillary pressure and liquid transport and therefore the nature of the media, whether it is hydrophobic or hydrophilic, is an important aspect.

Saturation

This parameter shows the volume fraction of the pore filled by a specific phase. It can be expressed as:

$$S_j = \frac{\text{volume taken by phase } j}{\text{total pore volume}} \quad (22)$$

In PEFCs, it is generally used for the liquid phase saturation, where it shows how much of the local pores is filled with the liquid water and what fraction of the pores is still open for the gas to pass through.

Contact angle

The angle at the interface between different phases is known as contact angle. It is a measure to show the wetting capability of a solid surface by a liquid phase. It depends on the surface temperature, and surface roughness. Depending on the angle whether

it is higher or lower than 90° , the surface is respectively called hydrophobic or hydrophilic. Usually the gas diffusion media is created in such a way to have both hydrophilic and hydrophobic characteristics to reach the desired two phase flow. This is done by adding hydrophobic PTFE to the naturally hydrophilic structure of the diffusion media.

Capillary transport

Pressure difference at the interfaces between two or more fluids due to the imbalance of the molecular forces is referred to as the capillary pressure and defined by

$$P_c = P_{nw} - P_w = \gamma \left(\frac{1}{r'} + \frac{1}{r''} \right) = \frac{2\gamma}{r^*} \quad (23)$$

where the subscript nw stands for the non-wetting surface while w refers to the wetting surface. r' and r'' are the two principle radii of the interface between the liquid and solid pore surface. r^* is the mean radius of the curvature and γ is the surface tension. In order to model the two-phase flow in porous media in PEFCs, it is conventional to assume the pores as capillary tubes of different radii where capillary pressure is defined as:

$$P_c = P_{nw} - P_w = \frac{2\gamma \cos \theta}{r^*} \quad (24)$$

where θ is the contact angle.

In hydrophobic media, the non-wetting phase pressure is larger than the wetting phase pressure and the capillary pressure is larger than zero, while in hydrophilic media the wetting phase pressure is higher than the non-wetting phase pressure and the resulting capillary pressure is lower than zero. This difference in pressure causes the fluid flow in the porous media. The capillary pressure is in direct connection with the pore radius. The higher the radius the lower the capillary pressure.

Leverett function

This function gives a relation between the liquid saturation and the capillary pressure to be used on calculation of the two-phase (liquid-gas) transport in the diffusion

media. However, it has been adopted from the soil science and used in modeling fluid flow in GDLs with the similar characteristics of flow in soil. In an attempt by Udell [3], Leverett approach was utilized to establish for capillary pressure as follows:

$$P_c = \gamma \cos \theta \left(\frac{\varepsilon}{k} \right)^{\frac{1}{2}} J(s) \quad (25)$$

where $J(s)$ expresses the Leverett function:

$$J(s) = \begin{cases} 1.42(1-s) - 2.12(1-s)^2 + 1.26(1-s)^3 & \theta < 90^\circ \\ 1.42s - 2.12s^2 + 1.26s^3 & \theta > 90^\circ \end{cases} \quad (26)$$

The term $\left(\frac{\varepsilon}{k} \right)^{\frac{1}{2}}$ takes into account the interfacial tension in the Leverett function.

1.3.3 Charge transport

Charges in the cell should be transported into and away from the catalyst active surface areas. Due to anisotropic nature of porous media the in-plane and through plane conductivities of porous media are different. Transport of ions are similar to transport of electrons but with some complexity. Both charge transports are the results of the potential gradient and both follow the ohm's law. Current per cross sectional area can be given by Ohm's law as:

$$j = -\sigma \nabla \phi \quad (27)$$

where σ is the electric conductivity. Similar to effective diffusivity, the effective electric conductivity is also proportional to porosity to tortuosity ratio, ε/τ , of the medium. Applying volume averaging, differential equation for charge conservation results in Laplace's equation for potential field as:

$$\nabla^2 \phi = 0 \quad (28)$$

Ionic transport follows the same rules as electrical transport mentioned above.

1.3.4 Heat generation and transport

PEFC is a system that operates at low temperatures and therefore heat rejection is challenging due to low temperature difference between the system and the environment. Heat generation in PEFC can be expressed using the cell voltage and thermal voltage as:

$$\dot{q} = i(E_{th} - E_{cell}) \quad (29)$$

where E_{th} represents the thermal voltage, and i is the current density. Difference between the thermal and Nernst voltages gives us the reversible heat generation known as Peltier heating:

$$\dot{q}_{heat,rev} = i(E_{th} - E_0) = i \left(-\frac{\Delta H}{nF} - \frac{\Delta G}{nF} \right) = -i \frac{T\Delta s}{nF} \quad (30)$$

Heat generated by ohmic and activation polarizations are the irreversible form of generated heat:

$$\dot{q}_{heat,irr} = i(E_0 - E_{cell}) = i(\eta_{act} + \eta_{ohm} + \eta_{conc}) \quad (31)$$

Combining the reversible and irreversible heat generations gives the total heat generation as:

$$\dot{q}_{total} = -i \frac{T\Delta s}{nF} + i(\eta_{act} + \eta_{ohm} + \eta_{conc}) \quad (32)$$

There are two main heat transfer modes in PEFC which are conduction and convection. Conduction is the result of intermolecular collisions. Conduction heat transfer can be explained using Fourier's law:

$$\dot{q}_{heat,i} = -k_i \frac{\partial T}{\partial x_i} \quad (33)$$

Convection heat transfer happens in many instances in PEFC most notably in places where there is a motion of fluid especially in fuel cell flow channels. The heat flux between a surface and a fluid can be defined as:

$$\dot{q}_{heat} = h(T_s - T_m) \quad (34)$$

where h is the local convective coefficient and T_m is the mean temperature of the fluid. The mean temperature can be calculated analytically using the relationships given for the flow in channels in the reference books such as Bergman et al. [4].

1.4 Polymer electrolyte degradation

One of the main obstacles in commercialization of PEFCs is the degradation of components which limits its service life. It seems that since there are no moving parts in PEFC, it should be durable and not degrade over time. However, these devices are architected precisely and small defects can create dramatic changes in its performance. PEFC durability depends strongly on the operating conditions and how the device is used. The performance degradation is small in magnitude but once it starts, it continues steadily because of high humidity conditions existing in PEFCs. This degradation can be exacerbated in special environments such as:

1. Operating at high temperature or low humidified conditions.
2. Large load cycling between low to high values.
3. Aggressive humidity or temperature swings in the environment.

PEFC is prone to a broad range of possible degradation mechanisms that can be caused by mechanical degradation, chemical degradation, or combination of both stresses. Thus, studying the PEFC durability is a large and complex field. In this section, various aspects of degradation that can happen in the membrane will be discussed.

1.4.1 Chemical degradation

Chemical degradation is known to be the primary life-limiting degradation mechanism in the membrane. In this mechanism of degradation, the radical species which are formed during fuel cell operation attacks the bonds and side chains of the polymer structure. Hydroxyl, hydroperoxyl and hydrogen peroxide are the radical species that are formed and they degrade the membrane chemically. Perfluorosulfonic Acid (PFSA) membranes are usually used in fuel cells since they are relatively

chemically stable. Chemical degradation shows itself by thinning in membrane thickness and emission of fluoride and CO_2 and H_2SO_4 in the exhaust stream. Thinning in the membrane increases the rate of gas cross over and ultimately cause failure. The rate of chemical degradation often monitored by determining the fluoride emission using in-situ monitoring devices. Based on the past studies, factors increasing the rate of chemical degradation are the higher operating temperature and low inlet relative humidity of reactants.

1.4.2 Mechanical degradation

Fuel cell stacks are normally compressed to minimize the electronic contact resistances in the cells. Low stack clamping is highly susceptible to experience performance loss and leakages while it can significantly reduce the risk of shortening. Mechanical stress can be classified into three different categories namely temperature induced, humidity induced and system induced stresses. Clamping force can be placed in the system induced stresses. Clamping force which is necessary to some extent to seal the cell components and reduce the contact resistance can be problematic if it is over a specific range. The pressure gradient between anode and cathode electrode sides can also cause a mechanical stress but it is usually not substantial as much as the clamping force.

Mechanical stress is the main cause of mechanical degradation in the membrane. Nafion is an elastic material that has an elastic modulus ranging between 45 and 145 MPa, with ultimate stress between 2.5 and 4.5 MPa. Also, its visco-plastic properties depend on the temperature and humidity as well. The membrane integrity degrades once the mechanical stress exceeds the local yield strength. This effect can show itself with the reduction in membrane thickness, membrane creeping and induced crazing sites that can end up as cracks or pinholes. These processes increase the chance of gas crossover in the cell and the delamination of the CL.

1.4.3 Thermal degradation

Membrane in PEFC shrinks or expands in volume depending on the local temperature of the cell. Increasing the cell temperature above a special value will damage the polymer chains in the membrane, decompose the polymer backbone and change its nanostructure integrity irreversibly. However, the PEFC usually works in low temperatures (below 100 °C), and also the thermal expansion coefficient of the membrane is low. Therefore, the thermal membrane degradation is not expected to have substantial impact on the whole degradation process in PEFC. Only in case where there is a defect in the membrane, local hot spots can be created causing a thermal decomposition of the membrane. But still that has been predicted not to have a large impact on the system and the temperature rise in local hot spots could be dissipated effectively through the porous media and by evaporation of the liquid water.

1.4.4 Hygroscopic swelling

Durability of the membrane generally improves by increasing hydration. Water can be taken into or taken out of Nafion causing the membrane to shrink or expand depending on the hydration rate. Membrane swelling is therefore a result of fluctuation in its relative humidity. Since the GDL has a lower through plane Young's modulus, membrane is not constrained in this direction. However, in the in-plane direction the elastic modulus is high for GDL creating a constraint in this direction for the membrane. The mechanical properties as well as operating parameters and their distributions are anisotropic, therefore the mechanical stresses and degradation processes induced are highly localized. The distribution of membrane hydration as well as water distribution inside the GDL, especially at its boundary with membrane, are the reasons for occurring membrane swelling or shrinking processes. In addition to in-plane direction, non-uniform distribution of water across the membrane also creates stress gradients in the through-plane direction.

1.4.5 Combined degradation

Chemical and mechanical degradation processes have a collaborative impact on the creation and evolution of the defects in the membrane. Once a defect forms in the membrane, different degradation mechanisms come into effect, synergistically. These combined mechanisms cause an exponential increase in the degradation rate. Knowing the initiating factor in the specific degradation mechanism and mitigating that specific process, can significantly reduce the overall rate of degradation. Many parameters such as pressure gradient between two electrodes, the feed rate, gas crossover and the oxygen concentration affect the overall degradation rate. For instance, gas crossover that is assumed to be a degradation accelerating factor, shows itself by crossing of hydrogen from the anode to the cathode or oxygen from the cathode to the anode, former to have the superior effect. Hydrogen crossover intensifies the pinhole growth and thermal degradation. On the other hand, oxygen crossover increases the chemical degradation by facilitating the formation of hydrogen peroxide.

CHAPTER 2

LITERATURE REVIEW

Literature survey is categorized in three different sections. First, the studies related to the characterization of the GDL and its anisotropic nature will be discussed. In the second part, the literature attributed to both water management and structural deformation under clamping force will be reviewed in detail. In the last section, the mechanical degradation phenomena in the fuel cell and studies in which analyses were done in this area will be presented.

2.1 Physical properties and characterization in GDLs

GDLs are composed of randomly distributed carbon fibers. Figure 3 presents different GDL configurations obtained by different approaches. Anisotropic orientation of the underlying fibers in GDLs, causes different transport coefficients in the in-plane and through-plane directions which directly affects the cell performance [5,6]. Therefore, how anisotropic transport properties of GDL affect cell performance of PEFC becomes an important issue.

The prevailing transport mode for the gases in GDLs is diffusion due to low permeability of these layers. What matters a lot in a fuel cell performance is its ability to diffuse the oxygen in an optimum form to the CL in all ranges of current densities. There are several investigations available in the literature evaluating the diffusion resistance of GDLs by estimating their effective diffusivity. Effective diffusivity is expressed as follows:

$$D_{eff} = f(\varepsilon)g(s)D \quad (35)$$

where D is the bulk diffusivity, ε is the porosity, s is the saturation of liquid water, and $f(\varepsilon)$ is a relative function of porosity and $g(s)$ is a relative function of liquid saturation.

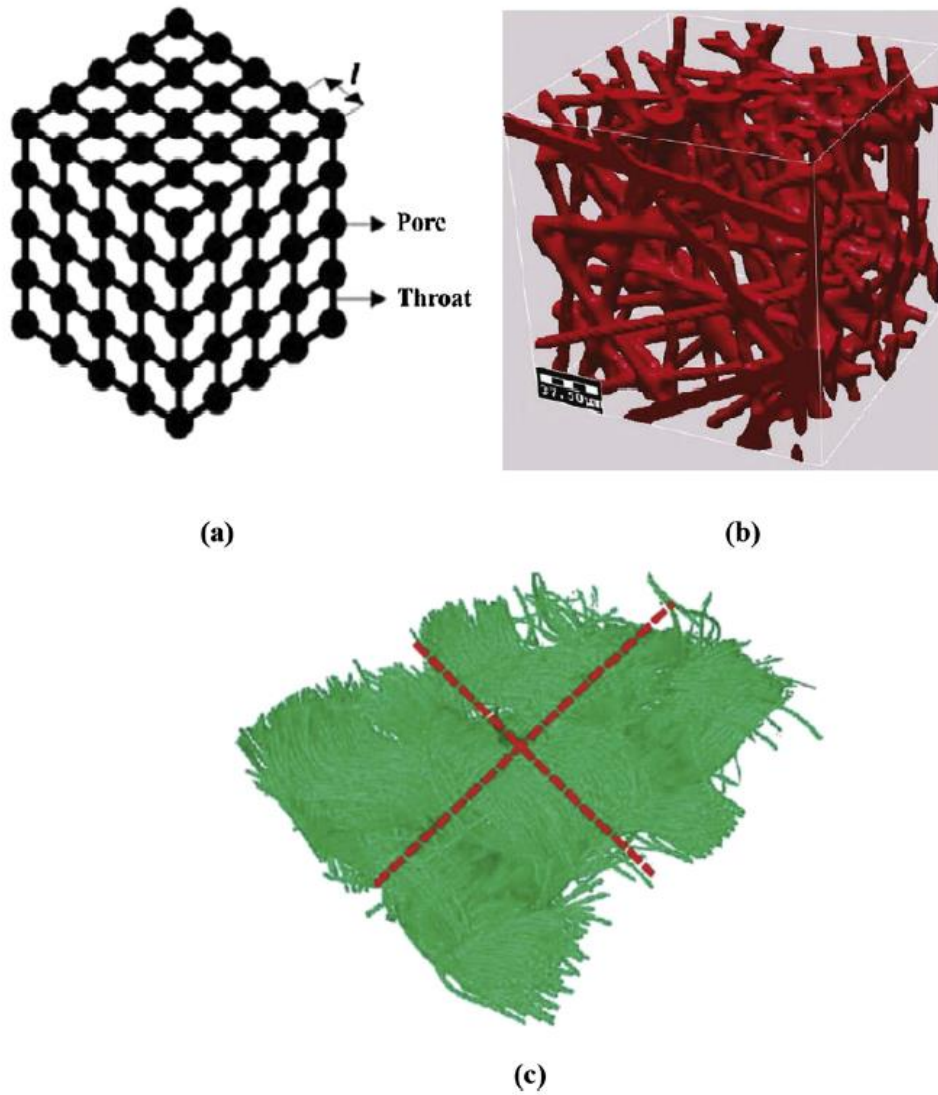


Figure 3 GDL representation using (a) pore network model, (b) stochastic model and (c) X-ray computed tomography (adapted from [6]).

The influence of GDL compression on water management is also important. Changing proportion of hydrophilic and hydrophobic surface areas is found to improve the water removal and to decrease the quantity of liquid holdup in the porous structure. The decrease of free pore volume is affecting the cell performance

predominantly in the mass transport regime. It is incorporated in the effective diffusivity in Fick's first law which is given as:

$$J = -D_{kl,eff} \nabla c \quad (36)$$

where J , c and $D_{kl,eff}$ represent the molar flux, gas concentration and the effective diffusion coefficient tensor, respectively. $D_{kl,eff}$ is composed of two components:

$$D_{kl,eff} = \frac{\varepsilon}{\tau} D_{kl} \quad (37)$$

where $\frac{\varepsilon}{\tau}$ is a form factor and D_{kl} is bulk diffusivity. Clamping force over a fuel cell mainly influences the GDL structural properties, because this component has the lowest Young's modulus of all other parts and therefore experiences the highest deformation upon application of compressive stress. Compression influences the porosity and tortuosity as well as the electrical properties of the GDL. Compressive strain increases the electrical conductivity of the GDL predominantly under the rib areas where the stress and deformation is highest and coactively decreases the contact resistance to the rib. However, the effective diffusivity of the porous medium is impaired upon compression by reducing porosity and increasing tortuosity. The compressed porosity ε at the compressed thickness d can be defined as:

$$\varepsilon = 1 - \frac{d_0}{d} (1 - \varepsilon_0) \quad (38)$$

where d_0 , ε_0 are measured uncompressed thickness and porosities. Inspection of the equations above clarifies that decreasing porosity and increasing tortuosity diminish the rate of reactant transport through the compressed region. The decrease of electric resistance in the GDL and at interfaces upon compression of the fuel cell is an expected impact on the cell performance. However, in conclusion, the dominating effect upon cell compression for a wide range of conditions is the decrease of the effective GDL diffusivity.

To evaluate the effect of porosity on the effective diffusivity of the GDL experimentally, one has two approaches; (i) to change its PTFE content and (2) to

compress the GDL with different ratios. This study will give us the chance to evaluate the second case where there is an acting clamping force over a cell with accompanying deformation in the structure of the GDL. Moreover, a literature survey has not unveiled any numerical study utilizing the data given in [6] for effective diffusivities in in-plane and through plane directions under a compressive force. By this study we will not only implement and investigate the anisotropic nature of the GDL media and its impact on fuel cell performance using those data but also will observe the compressive force and its influence on all other parameters in a PEFC as well as its overall cell performance.

Limited number of studies exist in the literature considering the effective diffusion properties of GDLs and their dependencies for analyses. Great portion of the studies are based on idealized morphology models where they assume that the porous medium is composed of commonly used spherical particles. (e.g. one of the most employed one in the literature is the Bruggeman assumption where the effective diffusivity is taken as $f(\varepsilon) = \varepsilon^{1.5}$). Table 1 illustrates a summary of the previous works done in this field presenting their contributions and outcome of the studies.

Table 1 Summary of studies done to estimate the effective diffusivity of the GDLs.

Researcher	Type of study	Effective relative diffusivity	GDL	Employed technique
Fluckiger et al. [5]	Exp.	Set of values for both in-plane and through-plane rel. eff. diff.	Toray-060	Electrochemical impedance spectroscopy
Nam and Kaviany [7]	Num.	$f(\varepsilon)_{th} = f(\varepsilon)_{in}$ $= \varepsilon \left(\frac{\varepsilon - 0.11}{1 - 0.11} \right)^{0.785}$	Toray	Pore network model
Zamel et al.[8]	Num.	$f(\varepsilon)_{th}$ $= 1$ $- 2.76\varepsilon \cosh(3\varepsilon$ $- 1.92) \left(\frac{3(1 - \varepsilon)}{3 - \varepsilon} \right)$ $f(\varepsilon)_{in}$ $= 1$ $- 1.72\varepsilon \cosh(2.07\varepsilon$ $- 2.11) \left(\frac{3(1 - \varepsilon)}{3 - \varepsilon} \right)$ $\varepsilon \sim 0.33 - 1$	Toray-120	Stochastic models created by GeoDict
Unsworth et al.[9]	Exp.	$f(\varepsilon)_{th}$ $= 1$ $- 2.76\varepsilon \cosh(2.53\varepsilon$ $- 1.61) \left(\frac{3(1 - \varepsilon)}{3 - \varepsilon} \right)$	Toray-120, Toray-060	Loschmidt cell diffusion cell
Kramer et al. [10]	Exp.	$f(\varepsilon)_{th} \sim 0.1 - 0.3$ $f(\varepsilon)_{in} \sim 0.25 - 0.55$ $\varepsilon \sim 0.5 - 0.8$	Toray-060	Electrochemical impedance spectroscopy

Researcher	Type of study	Effective relative diffusivity	GDL	Employed technique
Becker et al. [11]	Num.	$f(\varepsilon)_{th} \sim 0.25 - 0.3$ $f(\varepsilon)_{in} \sim 0.47 - 0.58$ $\varepsilon \sim 0.67 - 0.74$	Toray-060	X-ray computed tomography, GeoDict
Hwang and Weber [12]	Exp.	$f(\varepsilon)_{th} = \varepsilon^{3.6}$	Toray-120	The limiting current
Rosen et al. [13]	Num.	$f(\varepsilon)_{th} = \varepsilon^{3.5}$ $f(\varepsilon)_{in} = \varepsilon^2$	Toray-060	GeoDict, X-ray computed tomography
Wu et al. [14]	Num.	$f(\varepsilon)_{th}$ $= e^{\frac{(\varepsilon-1)}{0.222-0.161\%PTFE}}$	Toray	Pore network model
Gostick [15]	Num.	$f(\varepsilon)_{th} \sim 0.21$ $f(\varepsilon)_{in} \sim 0.45$ $\varepsilon \sim 0.75$	Toray-090	Random pore network
Zhang and Zhang [16]	Num.	$f(\varepsilon)_{th}$ $= \varepsilon \left(\frac{\varepsilon - 0.11}{1 - 0.11} \right)^{1.7}$ $f(\varepsilon)_{in}$ $= \varepsilon \left(\frac{\varepsilon - 0.11}{1 - 0.11} \right)^{0.785}$ $\varepsilon \sim 0.45 - 0.8$	Toray	Micro X-ray computed tomography, Lattice Boltzmann Model
Bruggeman [17]	Analyt.	$f(\varepsilon) = \varepsilon^{1.5}$	-	GDL is assumed as spherical agglomerates
Tomodakis & Sotirchos [18]	Num.	-	Toray	A random fiber model, Monte Carlo simulation

2.2 Compression impacts on multiphase flow in GDL

To avoid leakages and reduce contact resistances, it is customary to compress the fuel cell stack. This mechanical force induces inhomogeneous deformation in the GDL that brings uneven contact resistances as well as locally varying transport properties like porosity and permeability and deteriorates the local cell performance. The effect of mechanical deformation on the transport processes in GDLs creates challenges and motivation for investigation which is reflected in several publications [19]. The effect of compression on the morphology of the GDL is explored by Bazylak et al. [20] using scanning electron microscopy (SEM). They detected the influence of inhomogeneous compression of the GDL on the micro-structure of the material as well as reactant and liquid water diffusion pathways. Zhou et al. [21] studied the compression effect on a cell with interdigitated gas distributors. While low clamping force was seen to increase the interfacial electrical resistance, high clamping force was observed to increase the transport resistance because of reduction in GDL porosity. A two-dimensional model is developed in [22,23] to assess inhomogeneous compression impact on the transport properties and current density distribution. Maximum local current density was found under the rib due to lower contact resistances. Experimental data for porosity and permeability for both compressed and uncompressed GDLs are directly used in a numerical model by Su et al. [24] ignoring the deformation of the porous medium. Cell performance has been examined for the cases with homogenous and non-homogenous GDL properties. They showed that in order to achieve an even local current distribution, proper clamping force should be applied. Zhou et al. [25] implemented a micro-scale contact resistance model between BP and GDL and demonstrated that there is an optimal compressive force which improves the cell performance. Although findings of these studies are enlightening, many of them ignores some of the relevant issues in their models and therefore their results are subject to a large uncertainty.

Another challenge is the occurrence of flooding in the cathode that obstructs oxygen transport to reaction sites and causes further material degradation. Flooding occurs at the cathode side when the water removal rate of water by capillary transport,

evaporation, and back diffusion to anode does not keep up with the water generation rate in the cathode side, by the oxidation reaction and electro-osmotic drag from anode [26]. Shedding light on the fundamental process of liquid water evolution and transport in a PEFC at a local scale is still needed to prevent flooding and further enhance cell performance.

Previous efforts in PEFC modeling are mainly focused on transport of reactants and water, and its significance on cell performance [27,28]. There are also several structural models of PEFCs, which are not coupled to electrochemical and transport aspects of PEFC operation [29,30]. Moreover, although there are a number of studies in literature that address the two-phase transport in PEFC numerically [31–37], direct examination of phase change phenomena under inhomogeneous clamping force is almost absent, and if exists it is very rare and it either disregards the effect of compression on all physical properties of the GDL or do not investigate it in detail [38–49]. Further inspections are required to understand how compression alters the key relationships and its influence on local and overall PEFC performance as well as formation and transport of liquid water.

Among the studies which include both phase change phenomena and clamping force, Ihonen et al. [38] found that compression intensifies the cell flooding due to reduction in porosity. A finite element model designed for investigating the GDL deformation was coupled to a two-dimensional two-phase model of PEFC by Zhou and Wu [39]. Variation of porosity and contact resistance under compression was considered in their model. They observed that the detrimental effect of GDL compression on the cell performance aggravates in high current loads and in highly humidified air stream cases due to increase in liquid saturation. Effect of compressive force on the fuel cell performance was numerically studied for a variety of GDL parameters by Shi et al. [40]. GDLs with higher porosity values and higher compressive modulus provided higher current density with lower liquid saturation. Yoon and Huang [41] developed a multiphysics model which couples the gas mass transfer analysis and the micro electrical contact resistance analysis to study the effect of the assembly force on the cell performance. Significant changes in gas transport properties as well as current

density were seen with respect to changes in operating conditions and the degree of compressive force.

Wang and Chen [42] created a model considering spatially varying porosity values in GDLs. They compared their results with the saturation profile taken from neutron radiography data and stated that compressive force reduces the liquid saturation under the rib. A 3D model was developed for the cathode side of a PEFC by Olesen et al. [43] to investigate the GDL deformation on the liquid water and oxygen distribution under the rib and channel. Evaporation was seen to happen under the channel in the CL. As a recent effort, a three-dimensional, two-phase, isothermal PEFC model is presented by Chippar et al. [44]. They applied their computational fluid dynamics (CFD) code on the imported deformed geometry and compared its performance with the uncompressed cell. Multiphase mixture model (M^2) proposed by Wang and Cheng [31] was utilized for two-phase transport in the GDL. Reduction in porosity and permeability in the region under the rib caused higher amount of water accumulation and lower oxygen concentration, leading to lower local current density. Tranter et al. [45] developed a fibrous medium representation model to demonstrate the effect of compression on the single and two-phase flow in the GDL. While the liquid water was seen to spread mainly in the lateral direction for moderate compression, preferential liquid pathways as well as fast water ejection were observed in the case of high compressive force.

While continuum-based models are widely used for simulating water transport in PEFCs, there are also attempts to incorporate pore-scale physics into the simulation of liquid water in only compressed GDLs ignoring many aspects of real operating cell. Schulz et al. [46] simulated the two phase flow in the compressed GDL by developing the full morphology model into the reduced compression model. Porosity distribution, permeability and capillary pressure-saturation curves were reported for various compression levels. Mukherjee et al. [47] applied the compression model developed in [46] to stochastically generated non-woven carbon paper GDLs, and they investigated liquid water distributions at various compression states using a single and two-phase Lattice Boltzmann model. Liquid water transport has been

observed in the form of droplet interactions, flooding front formation and propagation. Using 3D X-ray tomography, images of the GDL samples under compression were obtained and equivalent pore networks were built accordingly by Fazeli et al. [48]. Invasion percolation algorithm has been employed in the models to capture the liquid water distribution. Optimum compressive force is proposed to improve water management and oxygen diffusion in the GDL. Lower saturation levels near the inlet of the compressed samples were seen compared to uncompressed samples.

Except [41] none of the references discussed above [38–40, 42–48] considers the water transport in the membrane which influences all the predicted values especially the liquid water saturation in the GDL. Furthermore, the referred 2D channel-rib models does not include any experimental validation at all not only on the cell scale but also on the channel-rib scale. All model validation to date was performed at the cell scale due to lack of experimental studies at channel-rib submillimeter scales. The integral current voltage validation method is insufficient for a model on the channel-rib scale especially where there is an acting compressive force on the cell creating inhomogeneous distribution of species in the porous media. There are two experimental studies [1,50] available in the literature reporting a set of local rate distribution data across the domain of channels and ribs using embedded Pt wires. The only attempt exists in the literature to validate their channel-rib model so far was carried out by Li et al. [49]. They could approximately explain current density profiles corresponding to the case with low humidified entrant gases. However, anisotropic nature as well as other physical and compression dependent material characteristics of GDL was not considered in their model and therefore their interpretation was not precise.

The model developed in our study is a 2D channel-rib model, based on the experimental study performed by Reum [2], coupling the deformation of components and transport of species and accounting for depletion of reactants and accumulation of products in the direction perpendicular to the flow. In our model, we also consider anisotropic and compression dependent transport of gases and liquid water in the

porous media. With this approach, we address the role of rib and channel on the distribution and transport of species in the GDLs and their direct impacts on local cell performance. The present model is validated with both overall performance curve and the local current density distribution.

2.3 Polymer electrolyte degradation

Considerable amounts of efforts have been dedicated to the development of stable, reliable and durable polymer electrolyte fuel cells (PEFCs). Progress in the mechanical durability of membranes has been remarkable, however the durability still remains an important issue and needs further studies. Performance degradation is unavoidable but its rate can be minimized thorough understanding of the mechanisms that lead to failure. Performance of PEFC deteriorates as the major cell components degrade. The electrolyte membrane, as a primary component, undergoes chemical and mechanical degradations that are not easily detectable with the current monitoring techniques. However, the degradations can lead to destructive membrane failures. Chemical degradation is related to the chemical decomposition of the membrane by the radicals, such as hydroxyl, hydroperoxyl and hydrogen peroxide, against the polymer backbone and side chains. Mechanical degradation is attributed to the gradual reduction in toughness and mechanical strength [51-53]. Mechanical stresses in the membrane originate from three mechanisms; first is the clamping force applied over the plates to prevent the leakages and also reduce the contact resistances. Clamping force brings about inhomogeneous deformation in GDLs and membrane, causing an uneven distribution of thermal and electrical resistances. It also creates non-uniform distribution of porosity under the rib and channel areas, changing the transfer properties for mass and charge in the GDL; second is the swelling and shrinking due to hydration and dehydration as a function of water content; and the third is thermal expansion due to temperature gradients in the membrane.

Load transients in a PEFC effectuate hydration, dry-out and temperature transients in the membrane. Since mechanical properties of the membrane are strongly dependent on temperature and humidity, the membrane is subject to hygro-thermal fatigue

loading during these transients [54]. Temperature/hydration cycling can induce expansion and contraction in the membrane. Since the membrane is constrained in the PEFC by GDLs and BPs, mechanical stresses occur in the form of in-plane compressive and tensile stresses in the membrane. These stresses may exceed the yield strength inducing plastic deformation and can lead to formation of pin-holes, cracks and delamination, resulting in reactant cross-over and cell/stack failure subsequently. Therefore, predicting the local distribution of these stresses is of paramount importance to prevent mechanical failure and to increase the endurance of the membrane by adept control strategies.

Mechanical degradations of PEFC components have become a focus of attention over the last decade. Many researchers have examined the mechanical behavior of fuel cell membranes under humidity and temperature cycling conditions with numerical models based on elasticity or elasticity-plasticity assumptions for material behaviors [51-55]. A preliminary theoretical analysis by Weber and Newman [56] demonstrated that mechanical stress inside the membrane need to be considered in experiments and models as it plays an important role in the water balance in the cell. Tang et al. [29] developed a finite element model to study in-situ stresses in polymer membranes subject to hygro-thermal loading. However, the temperature and relative humidity profiles inside the membrane was assumed to be constant. In-plane stresses were shown to be the dominant stresses in the membrane. Kusoglu et al. [57] performed simulations using previous experimental findings of mechanical properties of PFSA membrane [58], assuming a linear elasto-plastic constitutive behavior for the membrane with isotropic hardening. During hygro-thermal loading membrane experienced compressive stresses due to the cell constraints that prevents it from expansion. However, during the dry-out of the membrane, tensile residual stresses developed in the membrane due to redistribution of stresses induced by plastic deformation. In-plane stresses were observed to be the largest stress component compared to the through-plane stress and shear stresses induced. Stress levels were reported to exceed the yield stress, causing plastic deformation in the polymer membrane. Kusoglu et al. [30] studied the mechanical behavior of Nafion under

hydration–dehydration cycles. The membrane was cycled through various uniformly distributed humidity loads. They showed that membrane swelling has a dominant effect on in-plane stresses depending on the membrane thickness or the assembly conditions. They also suggested that the cathode side of the membrane is more prone to mechanical failure. Bograchev et al. [59] studied the evolution of stress and plastic strains during the start-up in both global and local scales. Hygro-thermo-mechanical load are introduced into the model. The GDL/seal joint interface was shown to be the most sensitive zone in terms of mechanical deformation. They showed that the generated stresses are significant enough to initiate plastic deformation in the membrane. The effect of non-uniform distribution of water in the membrane is studied by Kusoglu et al. [60] with a prescribed water content at the membrane boundaries and the diffusion of water across the membrane. Mechanical constraints were observed to restrict the swelling of the membrane and alter the water distribution in the membrane. Water content was seen to have a greater influence on the mechanical response than temperature.

The swelling-induced stresses and fatigue behavior were determined by Kusoglu et al. [61] utilizing numerical simulations for fuel cell relative humidity cycle tests. Authors report that pinholes, cracks, and delamination are the most probable failure mechanisms in the low compression region such as under the channel whereas at high humidity levels cavitation that leads to craze formation is less likely to occur in the compressed membrane. Higher humidity cycles lead to larger fatigue stresses and lower number of cycles to failure. Khattra et al. [62] created a viscoelastic-plastic constitutive model to capture the transient mechanical response of PFSA membrane. The observed levels of stresses were in direct relationship not only with the humidity and feed rate but also the sorption rate. Uniform humidity ratios in anode and cathode generated larger stresses compared to the non-uniform humidity loading. An elasto-visco-plastic stress model was proposed by Silberstein and Boyce [63] to investigate the effects of uniaxial and biaxial loading on Nafion. The temperature and hydration dependent elastic-plastic stress/strain behavior of Nafion under both monotonic and cyclic loading conditions were characterized. In their subsequent study [64] they

performed a bi-material swelling test on the membrane bonded to a GDL material to measure the membrane stresses and deformation magnitudes under hydration and dehydration loading. The authors incorporated the approach in a simplified fuel cell model to predict the strain evolution and potential failure spots in the membrane and observed negative hydrostatic pressures, which is the onset of cavitation and crazing under the channel.

The rates of fluoride release, membrane crossover and cell resistance as well as decrease in electrochemical surface area (ESA) were correlated to the degradation rate during cell operation by Vengatesan et al. [65]. Using an Infra-Red (IR) camera, they could observe the thermograms for the degraded MEAs with hotspots exhibiting local defects in the membrane. They noticed that the anode inlet is more susceptible to degradation and membrane failures, possibly due to the lower membrane hydration owing to the electro-osmotic drag which carries water from the anode to the cathode. Kreitmeier et al. [66] examined the local mechanical and chemical degradation in PEFC membranes. By analyzing the gas permeation rate through the MEA, the main source of inhomogeneous membrane degradation was identified as the spatial non-uniformities in relative humidity in the membrane and inlet gases.

Numerical models to predict PEFC degradation mechanisms play an important role in improving this technology. In recent years different cell models were proposed usually focusing on certain aspects while neglecting others to simplify the model. However, these simplifications limit the predictability of these models. The degradation mechanisms cannot be considered independently but should be coupled to the detailed cell model to reach the accurate local sources of degradation. There is a limited number of papers discussing membrane stress/strain distribution incorporating the compression effect on all cell components and their physical, electrical and transport properties. Furthermore, most of the existing membrane stress models do not account for transport of water within the membrane to obtain the water distribution across the length and thickness of the membrane for realistic load changes and therefore they use uniform membrane hydration models with the prescribed thermal and hygral boundary conditions. In order to accurately assess the

effect of material properties on the cell performance and its durability it is essential to recognize the location and the transport mechanisms of water throughout the cell.

There are some attempts [67-70] to expand the simplified models towards more rigorous multiphysics models incorporating different aspects of an operating fuel cell from electrochemistry and fluid dynamics to solid mechanics for determining the stress distribution. A three-dimensional model of PEFC with an accompanying stress model has been developed to investigate the displacement, deformation and stresses inside the cell during its operation by Baghdadi [67]. Non-uniform distribution of hygro-thermal stresses were predicted as an important factor contributing to delamination between the membrane and GDL. A 2D time-dependent model of PEFC incorporating the poroelastic deformation approach along with the water transport in the membrane was proposed by Yesilyurt [68]. The effects of load, inlet relative humidity and clamping force on the water distribution and stress evolution in the membrane were analyzed. Clamping force was seen to squeeze the membrane and flatter water distribution within the membrane. Escalating the inlet relative humidity and the load current leads to an increase in the membrane compression. Stress distribution in the membrane as a result of non-uniform membrane hydration was modeled by Serincan and Pasaogullari [69]. Operating voltage and relative humidity of the inlet gases were seen to influence the local water content in the membrane, bringing about inhomogeneous distribution of mechanical stresses. Hygral stresses were seen to be greater than the thermal stresses. The impacts of inlet pressure, relative humidity and stoichiometry as well as load changes on the magnitude of plastic deformation in the membrane were examined by Verma and Pitchumani [70]. Increase in cathode inlet pressure and relative humidity were observed to increase the plastic strain whereas increase in the cathode stoichiometry reduces the strain.

This study presents numerical modeling and simulation results for the mechanical deformation and stress-induced degradation of PEFC membranes. A comprehensive multiphysics model is developed to study stress and strain distributions on the cross-section of the membrane. Clamping pressure applied on the bipolar plates causes a non-uniform compressive stress on the membrane. Similarly, a non-uniform current

density and the water distribution make even more dramatic variations in the distribution of the stresses and the deformation of the membrane. Identification of the individual contributions to mechanical stresses, such as elastic, thermal, hygral and plastic stresses, in the PEFC membrane is of particular interest in this work. To the best of our knowledge, such a study has not been carried out extensively in the literature. This approach provides valuable physical insight on the locations prone to failure in the membrane and the contributions from hygro-thermal loadings, load currents and external forces. Results offer guidance on the design and control of PEFCs.



CHAPTER 3

EXPERIMENTAL STUDY ON PERFORMANCE EVALUATION OF PEFC UNDER CLAMPING TORQUE

The effect of compressive force on the performance of PEFC has been examined experimentally in Prof. Dr. T. Nejat Veziroglu Clean Energy Center at Niğde Ömer Halisdemir University in Turkey. During cell operation, relative humidity is kept constant. The only parameter which has been changed during the experiments is the clamping torque. Clamping torque on the bolts follows [71]:

$$T = F_{clamp}\mu_b D_b / N_b \quad (39)$$

where T is the tightening torque in Nm , F_{clamp} in the clamping force which itself is a function of clamping pressure and cell active area ($F_{clamp} = P_{clamp}A$), μ_b is the friction coefficient, D_b is the bolt nominal diameter and N_b is the number of bolts. The torque values obtained by these calculations give us a range of clamping torque to be applied over the cell.

3.1 Assembly method

Current study is performed on a 50 mm² cell. Three different torques are imposed on the cell and the corresponding performance curves are extracted from the system and optimum clamping force is identified. The clamping force was applied near the edges of the end plates via bolts. The pressure acting on the membrane is investigated using the pressure detection films (Pressurex). The change in color of these films illustrates the degree of the pressure on the membrane component as a result of clamping torque.

Serpentine flow channels are machined on BPs in both anode and cathode sides. For the membrane, Nafion 212 is chosen. Silicon gaskets are also used. In order to distribute the clamping torques evenly over the cell surface, eight bolts are used. Copper sheets are used to collect the currents. For each experiment the assembled cell is compressed under a clamping torque that increases incrementally. Components of the cell are illustrated separately in Figure 4. Test setup used for performing experiments on the fuel cell is demonstrated in Figure 5.

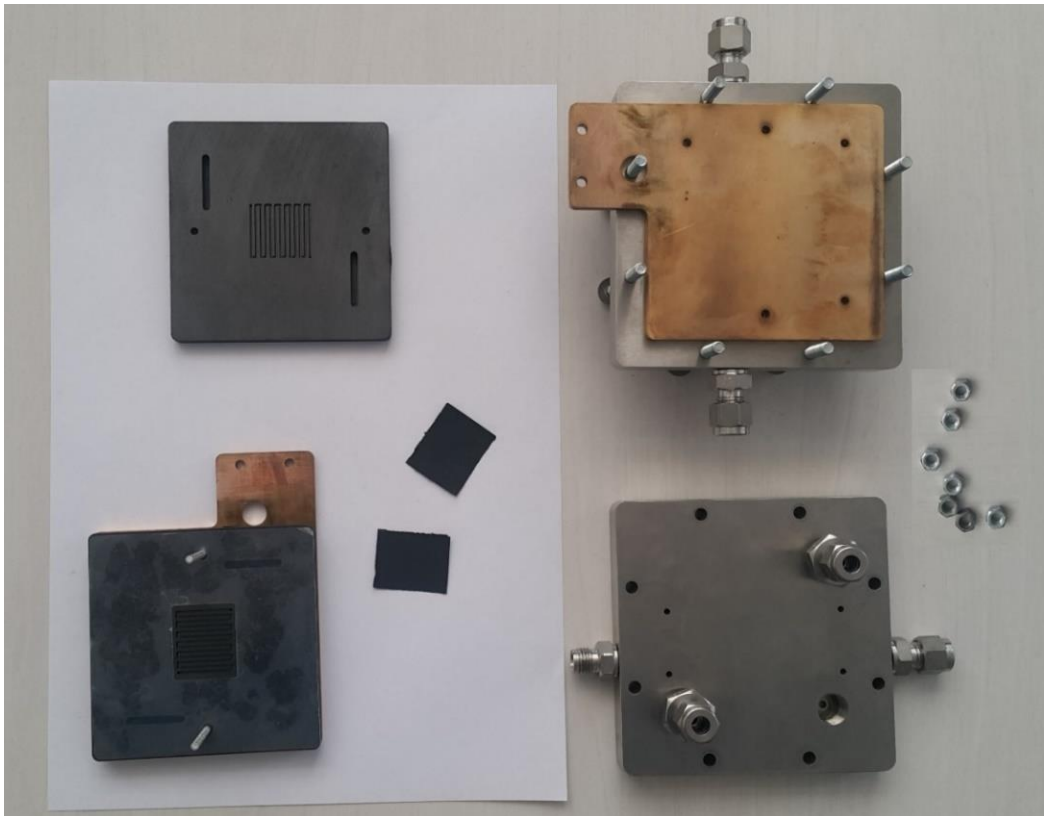


Figure 4 Disassembled components of the tested fuel cell.

3.2 Pressure distribution

Pressure distribution is measured by the pressure films. Before running the setup for a special case, the fuel cell is equipped by pressure films between the GDLs and reactant flow plate and the bolts are fastened using the torque meter to a desired torque value. Then the bolts are unfastened and the film are taken out and analyzed to determine the degree of the pressure locally over the active area. The procedure is

repeated for all three cases and the pressure distributions are observed for each case. Resulting marks on the pressure films for three performed cases are shown in Figure 6. Increasing the compressive pressure by the applied torque results in darker colors on these films.

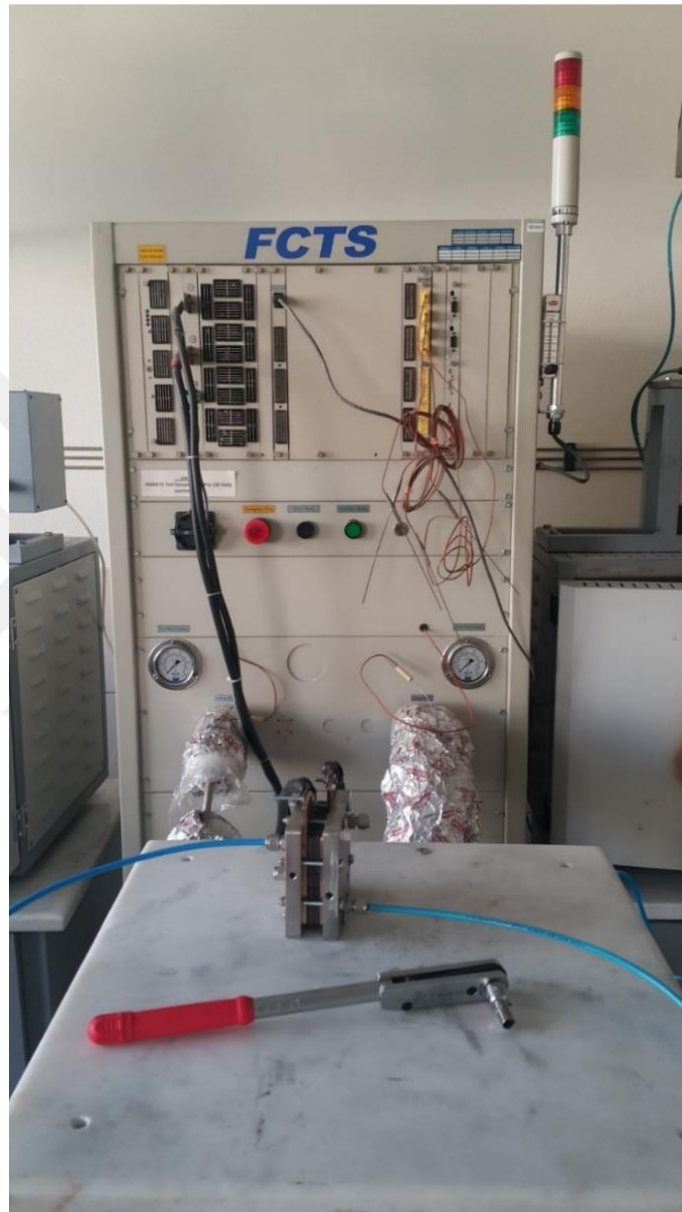


Figure 5 Test setup for experiments on PEFC.

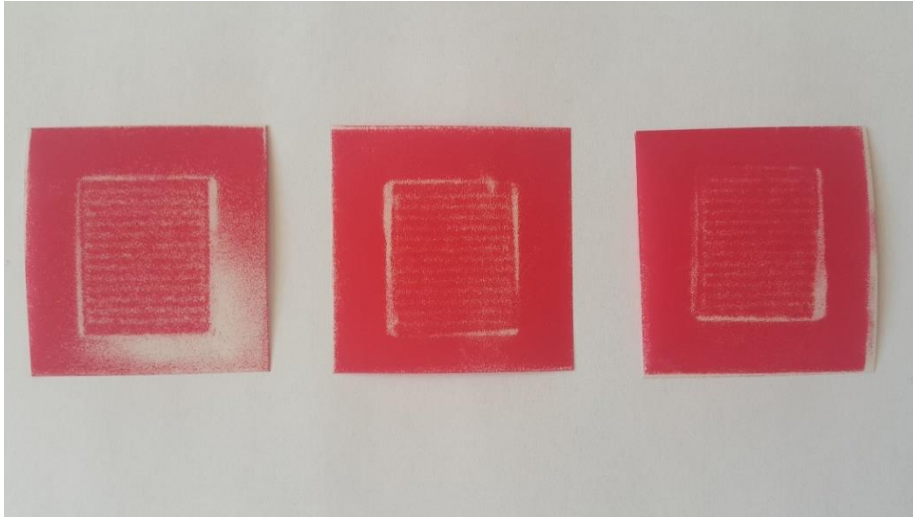


Figure 6 Pressure distribution results over the presssurex films. From the left to right the torques applied on the cell are 5, 10 and 15 Nm.

3.3 Voltage-current and power-current curves

The experiments are done with fully humidified oxygen and hydrogen. The gas flow rates are regulated by the mass flow controllers and kept constant at 0.1 Lmin^{-1} and 0.2 Lmin^{-1} for anode and cathode, respectively. Polarization curves are extracted by drawing current from the cell. These data are recorded after 5 continuous cycles.

3.4 Results and discussions

The experimental setup is shown in Figure 5. In order to identify the influence the compressive force has on the cell performance for different torques, polarization curves are extracted for each case and compared on a single plot as shown in Figure 7. As seen from the figure, cell performance decreases by increasing the torque values. Here we have only three different torque values and between these, increasing the torque from the starting value of 5 Nm upto 15 Nm have shown that compressive force has a detrimental effect on the cell performance.

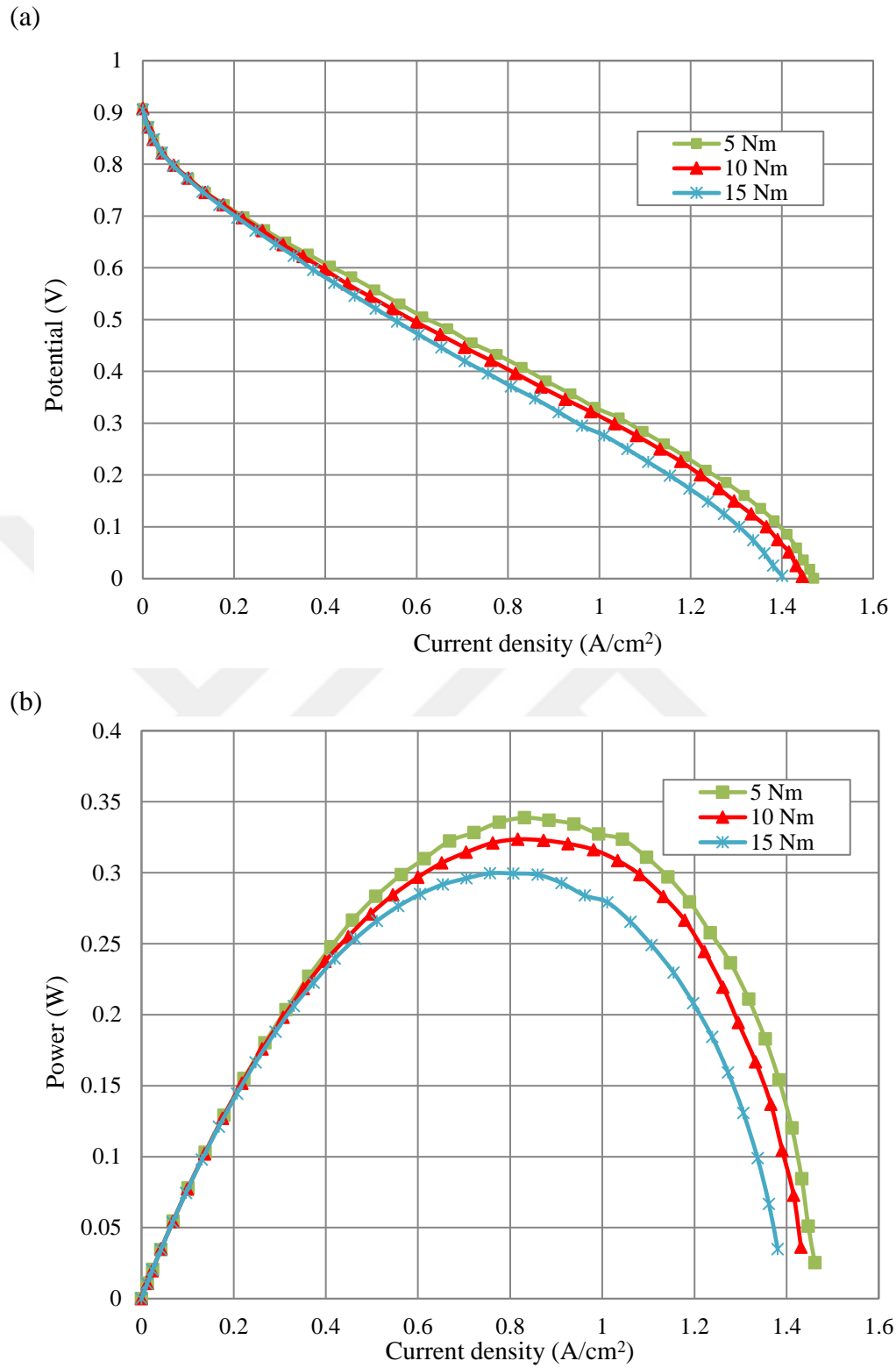


Figure 7 (a) Performance curves and (b) power curves at three different applied torques.

Clamping force is known to have a positive effect on cell performance due to reduction in contact resistances, however in our experiments this impact cannot be distinguished most probably due to low number of experiments. It is expected to see an optimum assembly pressure where the clamping force decreases the contact resistance and improves the cell performance and after that point further compression increases the mass transfer resistance and reduces the cell performance. Examining the Figure 6 where the pressure films are illustrated for those three cases, identifies the over compression in the case with 15 Nm torque. This detrimental effect is also seen in polarization curve where there is a dramatic decline in voltage due to high mass flow resistance in the cell.

At low current densities, the contact resistance is the dominant parameter, while at higher current densities, the mass transport resistance is important and the compressive force detrimental effect shows itself strongly. Overall the higher the compressive force, the higher the negative effect on the cell performance which is the outcome of the damaged GDL with higher mass transport resistivity.

CHAPTER 4

CHANNEL-RIB MULTIPHYSICS MODEL

In this chapter, numerical model built for the analyses is presented. All conservation equations used in the model are explained. Also, boundary conditions, parameters, and material properties considered in the model are given.

4.1 Model description

A two-dimensional numerical model is established based on the experiments conducted by Reum [2] in order to perform simulations and understand the effects of compression on cell performance. The model, shown in Figure 8, is composed of current flow channels, BPs, CLs, membrane and gas diffusion media (GDMs) which include GDLs and MPLs. Clamping force is applied vertically on the cathode side of the model over the BP which influences all parts of the cell structurally.

Without losing the general physical characteristics of a PEFC, some assumptions have been made for the model used in the numerical simulations, including:

- 1) The cell is operated under steady state conditions.
- 2) The flow channel is approximated as a straight channel and therefore the depth of the channel along the flow direction is not included in the model.
- 3) The porous media are treated as morphologically anisotropic in terms of porosity, tortuosity, diffusivity, and permeability.
- 4) Phase change of water and transport of liquid water are considered only at the cathode.
- 5) Each CL is modeled as an ultra-thin layer and the transport of reactants within this layer is neglected.

- 6) The electrochemical reaction rate is described by agglomerate model in the cathode.
- 7) A linear elastic perfectly plastic model, is adopted for the membrane.
- 8) Electrical and thermal contact resistances are taken into account in the model.
- 9) Water transport in the membrane due to pressure gradient is recognized to have a negligible effect and is not considered in the model.
- 10) There is no reactant crossover through the membrane.

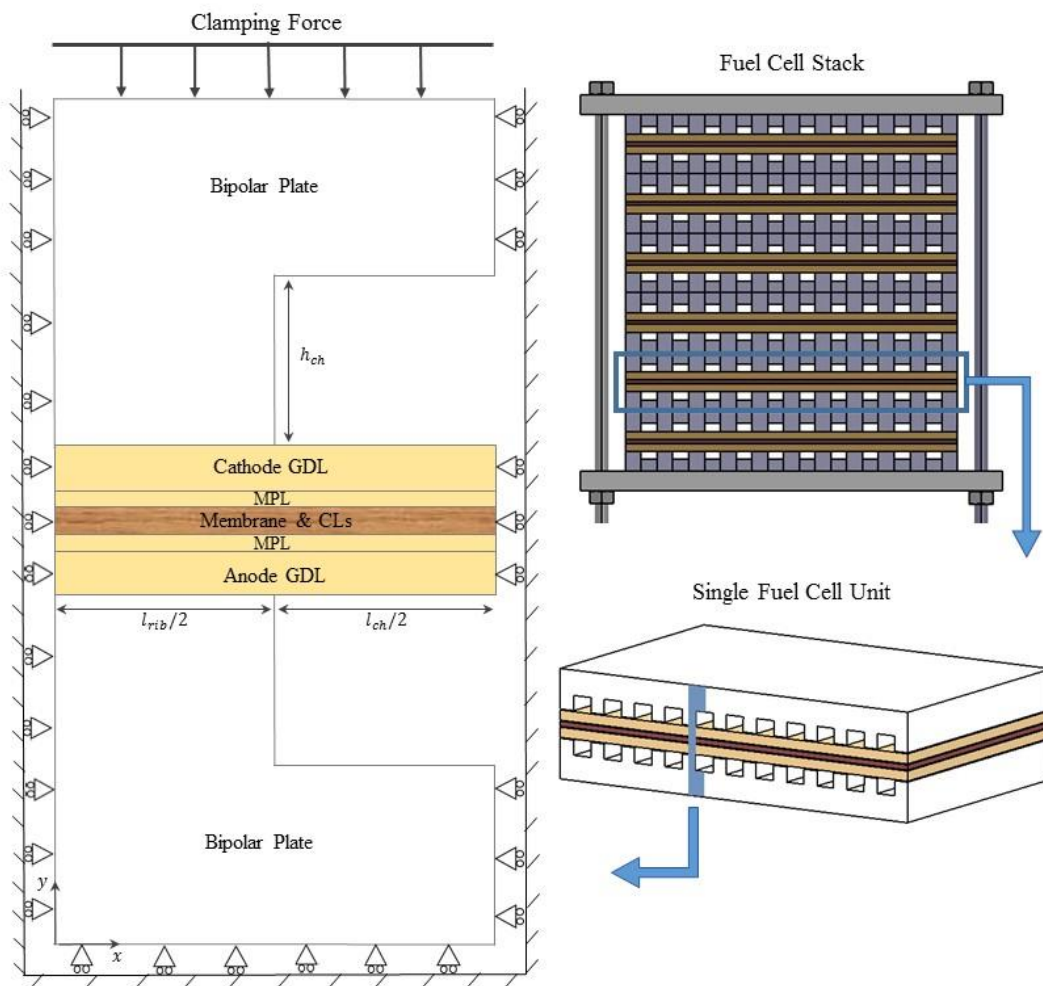


Figure 8 Schematic of the computational domain created based on [2].

4.2 Governing equations

In Table 2, the governing equations used in the model are summarized. Following that, each equation is also explained in detail.

Table 2 Summary of governing equations.

Conservation equations	General form of conservation equation
Mass	$\nabla \cdot (\varepsilon \rho \mathbf{u}) = S_m$
Momentum	$\nabla \left[-\rho w_i \sum_{j=1}^N D_{ij} \left\{ \left(\nabla x_j + (x_j - w_j) \frac{\nabla p}{p} \right) \right\} + \rho w_i \mathbf{u} \right] = S_i$
Electronic charge	$-\nabla \cdot (\sigma_e \nabla \Phi_e) = S_{\Phi_e}$
Ionic charge	$-\nabla \cdot (\sigma_m \nabla \Phi_m) = S_{\Phi_m}$
Energy	$\nabla \cdot (\rho c_p \mathbf{u} T) - \nabla \cdot (k_{eff} \nabla T) = S_T$
Dissolved water	$-\nabla \cdot \left(n_d \frac{\sigma_m}{F} \nabla \Phi_m \right) - \nabla \cdot \left(\frac{\rho^{Naf}}{EW} D_{H_2O}^{Naf} \nabla \lambda \right) = S_\lambda$
Liquid water	$\nabla \cdot (\varepsilon \rho_{H_2O,l} \mathbf{u}_{H_2O,l}) = S_{H_2O}^l$
Force	$-\nabla \cdot \sigma_{ij} = S_f$

4.2.1 Transport of gas species in GDMs

Transport of H_2 and H_2O vapor in the anode GDL and O_2 , N_2 , H_2O in the cathode GDL are governed by Maxwell-Stefan equation as presented in [68]:

$$\nabla \left[-\rho w_i \sum_{j=1}^N D_{ij} \left\{ \left(\nabla x_j + (x_j - w_j) \frac{\nabla p}{p} \right) \right\} + \rho w_i \mathbf{u} \right] = S_i \quad (40)$$

where w is mass and x is molar fraction of the i th species. D_{ij} is the binary diffusion coefficient of species i and j defined as [72]:

$$D_{ij} = 3.16 \times 10^{-8} \left(\frac{T^{1.75}}{P(\vartheta_i^3 + \vartheta_j^3)^2} \right) \left(\frac{1}{M_i} + \frac{1}{M_j} \right)^{1/2} \quad (41)$$

where P is pressure, and T is the temperature. ϑ_i represents the diffusion volume of species i , M_i is the molecular weight of species i and \mathbf{u} is the convective velocity

field. Gas flow in the GDL is modeled using Darcy's law to calculate velocity fields of the mixtures as

$$\mathbf{u} = -\frac{K}{\mu}\nabla P \quad (42)$$

where K is the permeability of GDMs and μ is the viscosity of mixture [72].

4.2.2 Transport of energy

The temperature variation is generally not very large in PEFCs and has been commonly neglected. However, temperature has direct influences on almost all transport and reaction processes. Particularly temperature distribution is essential to reach a realistic saturation measurement in the two-phase flow modeling. In this model, it is assumed that the gas, liquid, and solid phases are always in a thermal equilibrium state. While in BPs and membrane only conduction heat transfer is modeled, in GDMs heat transfer due to conduction and convection is modeled using conservation of energy equation as

$$\nabla \cdot (\rho c_p \mathbf{u} T) - \nabla \cdot (k_{eff} \nabla T) = S_T \quad (43)$$

where c_p is the heat capacity and k_{eff} is the effective conductivity and evaluated based on the volume fraction of each phase as

$$k_{eff} = \varepsilon k_g + (1 - \varepsilon) k_s \quad (44)$$

where ε stands for the porosity of the GDM under compression. S_T in Equation (43) represents the heat source which consists of activation heat generation, reversible heat release from electrochemical reaction, ohmic heating, and latent heat during condensation or evaporation:

$$S_T = S_{T,act} + S_{T,rev} + S_{T,ohm} + S_{T,cond/evp} \quad (45)$$

The heat source used for CLs, GDMs, and the membrane are given in Table 3. In the model, convection heat flux is also considered at GDL-channel and BP-channel interfaces.

Table 3 Source terms used in the governing equations.

Volumetric source terms	Units
$S_m = S_{O_2} + S_{H_2} + S_{wv}$	$\text{Kg m}^{-3} \text{s}^{-1}$
$S_i = \begin{cases} S_{H_2} = -\frac{j}{2F} M_{H_2} & \text{CL}_a \\ S_{O_2} = -\frac{j}{4F} M_{O_2} & \text{CL}_c \\ S_{H_2O} = \begin{cases} \frac{j}{2F} M_{H_2O} + M_{H_2O} S_\lambda - S_{H_2O}^l & \text{CL}_c \\ -S_{H_2O}^l & \text{GDM}_c \\ M_{H_2O} S_\lambda & \text{CL}_a \end{cases} \end{cases}$	$\text{Kg m}^{-3} \text{s}^{-1}$
$S_{\phi_e} = \begin{cases} -j & \text{CL}_a \\ +j & \text{CL}_c \end{cases}$	A m^{-3}
$S_{\phi_m} = \begin{cases} +j & \text{CL}_a \\ -j & \text{CL}_c \end{cases}$	A m^{-3}
$S_T = \begin{cases} j \left(\eta - \frac{T\Delta S}{nF} \right) + \frac{J_i^2}{\sigma_m} + S_{H_2O}^l h_{lg} & \text{CL}_c \\ \frac{J_i^2}{\sigma_e} + S_{H_2O}^l h_{lg} & \text{GDL}_c \\ j (\eta) + \frac{J_i^2}{\sigma_m} & \text{CL}_a \\ \frac{J_i^2}{\sigma_m} & \text{membrane} \end{cases}$	W m^{-3}
$S_\lambda = \begin{cases} k_\lambda (\lambda - \lambda_{eq}) & \text{CL}_a \\ k_\lambda (\lambda - \lambda_{eq}) & \text{CL}_c \end{cases}$	$\text{mol m}^{-3} \text{s}^{-1}$
$S_{H_2O}^l = \begin{cases} k_{evp} \varepsilon \rho_{H_2O,l} (p_g^{H_2O} - p_{sat}^{H_2O}) & p_g^{H_2O} < p_{sat}^{H_2O} \text{ GDM}_c \\ k_{cond} \varepsilon (1-s) \frac{x_{H_2O} M_{H_2O}}{RT} (p_g^{H_2O} - p_{sat}^{H_2O}) & p_g^{H_2O} > p_{sat}^{H_2O} \text{ GDM}_c \end{cases}$	$\text{Kg m}^{-3} \text{s}^{-1}$

4.2.3 Conservation of charge

In GDLs, electrons are the charge carriers. Ohm's law is adopted to express the conservation of charge as follows:

$$-\nabla(\sigma_e \nabla \phi_e) = S_{\phi_e} \quad (46)$$

where σ_e represents the effective conductivity of the medium and ϕ_e is the electric potential. There are no charge sources or sinks since the CLs are assumed as an interface between the membrane and GDL.

Protons are the charge carriers in the membrane. To keep the ionic current in the same direction as the electrons, similar to that of electron, conservation of charge is given as:

$$-\nabla(\sigma_m \nabla \Phi_m) = S_{\Phi_m} \quad (47)$$

where Φ_m is the ionic potential and σ_m is the effective conductivity of the membrane. Ionic conductivity as a function of the membrane water uptake for different temperatures are given in [73] as:

$$\sigma_m = (0.514\lambda - 0.326) \exp \left[1268 \left(\frac{1}{303} - \frac{1}{T} \right) \right] \quad (48)$$

4.2.4 Transport of water in the membrane

Water flux through the membrane is the sum of the two main driving forces namely, the diffusion due to gradient of water concentration and the electro-osmotic drag due to gradient of ionic potential as [74]:

$$-\nabla \left(n_d \frac{\sigma_m}{F} \nabla \Phi_m \right) - \nabla \cdot \left(\frac{\rho^{Naf}}{EW} D_{H_2O}^{Naf} \nabla \lambda \right) = S_\lambda \quad (49)$$

where ρ^{Naf} is the density of Nafion. n_d is the number of dragged water molecules per proton and σ_m is the ionic conductivity of membrane. F is Faraday's constant, Φ_m is the ionic potential, and λ is

$$\lambda = \frac{EW}{\rho^{Naf}} c_{H_2O}^{Naf} \quad (50)$$

where EW is the equivalent weight of Nafion and $c_{H_2O}^{Naf}$ is the volume concentration of dissolved water in Nafion. The mass transfer coefficient in the electrolyte phase, $D_{H_2O}^{Naf}$, is calculated experimentally by Ge et al. [75] as follows:

$$D_{H_2O}^{Naf} = \begin{cases} a_{H_2O} (0.0543 + 0.00336\lambda) \exp \left(2416 \left(\frac{1}{T_0} - \frac{1}{T} \right) \right) & \lambda > 12.08 \text{ at } T = 323 \text{ K} \\ a_{H_2O} (0.0771 + 0.00259\lambda) \exp \left(2416 \left(\frac{1}{T_0} - \frac{1}{T} \right) \right) & \lambda > 9.20 \text{ at } T = 353 \text{ K} \end{cases} \quad (51)$$

4.2.5 Transport of liquid water

Water in PEFC comes from the oxygen reduction reaction (ORR), and water vapor in humid gas. The liquid water in the cathode side GDL forms from water vapor

condensation process. This condensation occurs when the water vapor partial pressure exceeds water saturation pressure. Since the operating temperature in PEFCs is relatively low, condensation is likely, especially at high current densities. In multi-phase flow, the continuity equation for liquid phase within the cathode GDL, based on the approach proposed in [33–36] for water exchange between the gas and liquid phases known as unsaturated flow model, is

$$\nabla \cdot (\varepsilon \rho_{H_2O,l} \mathbf{u}_{H_2O,l}) = S_{H_2O}^l \quad (52)$$

where $\rho_{H_2O,l}$ is the density of liquid water, and $\mathbf{u}_{H_2O,l}$ is the liquid water velocity. $S_{H_2O}^l$ is the condensation-evaporation source term which is implemented in the model as shown in Table 3. In this term, the porosity values take into account the clogging effect of the porous media and the flooding effect of the reaction surface is considered by multiplying it by $(1-s)$. The difference between local vapor pressure and the saturation pressure acts as a switch function determining the evaporation and condensation rates. The saturation pressure is calculated as [73]

$$\log_{10} P_{sat} = -2.1794 + 0.02953(T - 273.15) - 9.1837 \times 10^{-5}(T - 273.15)^2 + 1.4454 \times 10^{-7}(T - 273.15)^3 \quad (53)$$

The liquid water velocity is calculated by Darcy-law approximation to momentum conservation as

$$\mathbf{u}_{H_2O,l} = \frac{K_{rl}K}{\mu_{H_2O,l}} \nabla P_{H_2O,l} \quad (54)$$

where K_{rl} is the relative permeability of liquid water. The liquid pressure in the porous media can be written as

$$P_{H_2O,l} = P_g - P_c \quad (55)$$

where P_c is the capillary pressure which is the gas flow induced viscous drag effect. Assuming constant absolute gas pressure, differentiation of $P_{H_2O,l}$ results in

$$\nabla P_{H_2O,l} = -\frac{dP_c}{ds} \nabla s \quad (56)$$

There are number of ways for developing saturation dependent capillary pressure functions. Here, the approach is developed based on Leverett $J(s)$ function [76] as

$$P_c = \sigma \cos\theta \left(\frac{\varepsilon}{K}\right)^{0.5} J(s) \quad (57)$$

in which σ is the liquid-gas surface tension, and θ is the pore scale contact angle.

$J(S)$ is given as [32]

$$J(s) = \begin{cases} 1.42(1-s) - 2.12(1-s)^2 + 1.26(1-s)^3 & \theta < 90^\circ \\ 1.42s - 2.12s^2 + 1.26s^3 & \theta > 90^\circ \end{cases} \quad (58)$$

Based on the fact that GDL is also impregnated with a PTFE, both GDL and MPL use the correlation for hydrophobic materials assuming contact angles of 95° and 130° respectively. Combining equations given above yields a differential equation for saturation distribution in the cathode GDM. In this study, homogeneous mist flow is assumed in the channel and hence s is taken as zero at the channel-GDL interface. Moreover, to account for the liquid-vapor phase change and to couple the water and heat transports in PEFC, the latent heat of vaporization is enabled in whole GDM domain.

4.2.6 Deformation

Deformation of all solid components are modeled using plane-strain formulation of the linear elasticity:

$$-\nabla \cdot \sigma_{ij} = S_f \quad (59)$$

where σ_{ij} are the stress components for $i, j = \{x, y, z\}$ and defined as [68]:

$$\sigma_{ij} = \frac{E}{(1+\nu)} \left(\epsilon_{ij} + \frac{\nu}{1-2\nu} \epsilon_{kk} \delta_{ij} \right) \quad (60)$$

In Equation (60), E is the Young's modulus and ν is Poisson's ratio of the material. $\epsilon_{ij} = \partial w_i / \partial x_j$ are the strain components and ϵ_{kk} is the volumetric bulk strain ($\epsilon_{kk} = \epsilon_{xx} + \epsilon_{yy}$). S_f represents the clamping force applied on the cell.

4.3 Boundary conditions

4.3.1 Mass fractions in the Maxwell-Stefan equation

Flow in gas channels are considered as laminar flow. At interfaces between gas channels and GDLs, convection mass transfer is assumed as follows:

$$\rho w_i [\mathbf{u} - \sum_{j \neq i} D_{ij} \nabla x_j] \cdot \mathbf{n} = h_{i,ch} (w_i - w_{i,ch}) \quad (61)$$

where $w_{i,ch}$ is the mass fraction of the i th species in the flow channel, and $h_{i,ch}$ is the mass transfer coefficient determined from Sherwood number, Sh , which is constant for gas flow in a square-cross-section [72] as:

$$Sh = \frac{h_{i,ch} l_{ch}}{D_{i,mix}} = 2.7 \quad (62)$$

where l_{ch} is the length of the channel, and $D_{i,mix}$ is the diffusion coefficient of the i th species in the gas mixture.

At membrane-GDM interfaces, flux boundary conditions are assumed to simulate the sinks and sources regarding the consumption rates of species and water flux from the membrane as

$$\rho w_i [\mathbf{u} - \sum_{j \neq i} D_{ij} \nabla x_j] \cdot \mathbf{n} = \frac{M_i i_{\{a,c\}}}{n_i F} + \delta_{i,H_2O} \rho_{H_2O} \mathbf{u}_m \cdot \mathbf{n} \quad (63)$$

where M_i is the molar mass of the i th species. n_i is the stoichiometric coefficient of each species and negative for H_2 and O_2 and positive for H_2O . δ_{i,H_2O} is Kronecker delta which is 1 for H_2O and \mathbf{u}_m is the velocity of membrane water. i_a and i_c are the anode and cathode exchange current densities, respectively. At the symmetry surfaces the fluxes of all species are set to zero in the normal directions [68].

4.3.2 Conservation of charge

The electric potential is set to ground at the anode side. The normal current density is set as the ratio of the potential difference between the GDL and the rib to the contact resistance at the anode-rib boundary:

$$\mathbf{J}_e(x_{0-l_{rib}/2}, 2h_{ch}) = \frac{\Phi_{BP} - \Phi_{GDL}}{R_{cr}} \quad (64)$$

$$\mathbf{J}_e(x_{0-l_{rib}/2}, 2h_{ch} + 2\delta_{GDL} + 2\delta_{MPL} + \delta_{mem}) = \frac{\Phi_{BP} - \Phi_{GDL}}{R_{cr}} \quad (65)$$

At membrane-GDM interfaces, electric and ionic currents are given by the exchange current densities as:

$$\mathbf{J}_e(x, 2h_{ch} + \delta_{GDL} + \delta_{MPL}) \cdot \mathbf{n}_a = i_a \quad (66)$$

$$\mathbf{J}_e(x, 2h_{ch} + \delta_{GDL} + \delta_{MPL} + \delta_{mem}) \cdot \mathbf{n}_c = -i_c \quad (67)$$

$$\mathbf{J}_m(x, 2h_{ch} + \delta_{GDL} + \delta_{MPL}) \cdot \mathbf{n}_m = -i_a \quad (68)$$

$$\mathbf{J}_m(x, 2h_{ch} + \delta_{GDL} + \delta_{MPL} + \delta_{mem}) \cdot \mathbf{n}_m = i_c \quad (69)$$

In Equations (66-69), \mathbf{n}_a , \mathbf{n}_c , and \mathbf{n}_m are the outward surface normals with respect to the anode, cathode, and membrane, respectively.

4.3.3 Conservation of membrane water

It is recognized that dissolved water entering or leaving the electrolyte phase is far from equilibrium in an operating PEFC. Accordingly, the source term of water content is taken as the difference between water content and equilibrium sorption values. The equilibrium water sorption, λ_{eq} , at the boundary is calculated as [75]:

$$\lambda_{eq} = \begin{cases} 0.043 + 17.81a_{H_2O} - 39.85a_{H_2O}^2 + 36a_{H_2O}^3 & T = 303 \text{ K} \\ 0.3 + 10.8a_{H_2O} - 16a_{H_2O}^2 + 14.1a_{H_2O}^3 & T = 353 \text{ K} \end{cases} \quad (70)$$

where a_{H_2O} is the water activity, which is defined as

$$a_{H_2O} = x_{H_2O} \left(\frac{P}{P_{sat}} \right) \quad (71)$$

4.3.4 Deformation

Equation (59) is solved by the principle virtual work [68] using the displacement vector, $w = [\xi, \zeta]'$, where the strain-tensor components are

$$\epsilon_x = \frac{\partial \xi}{\partial x}, \quad \epsilon_y = \frac{\partial \zeta}{\partial y}, \quad \epsilon_{xy} = \frac{1}{2} \left(\frac{\partial \xi}{\partial y} + \frac{\partial \zeta}{\partial x} \right) \quad (72)$$

As presented in Figure 8, the bottom side of the model is assumed to be fixed and can not move in the y-direction, i.e.,

$$\zeta(x < l_{tot}, 0) = 0 \quad (73)$$

where $l_{tot} = (l_{rib} + l_{ch})/2$ is the total width of the PEFC section. While the left and right sides are fixed in x-direction, they can move in the y-direction as

$$\xi(0, y) = 0 \quad (74)$$

$$\xi(l_{tot}, y) = 0 \quad (75)$$

The top section is subject to constant compressive load due to clamping and free to move in the y-direction.

4.4 Parameters

4.4.1 Physical properties and base operating conditions

In Table 4, physical properties used in PEFC model as well as the base operating conditions are listed. Most of the values are taken from [1,2].

Table 4 Physical properties and base operating conditions.

Property, symbol	Value, unit
Rib length, l_{rib}	2×10^{-3} m
Channel height, h_{ch}	1×10^{-3} m
Channel length, l_{ch}	2×10^{-3} m
GDL thickness, δ_{GDL}	200×10^{-6} m
MPL thickness, δ_{MPL}	30×10^{-6} m
Membrane thickness, δ_m	60×10^{-6} m
Faraday's constant, F	96487 C mol ⁻¹
Universal gas constant, R	8.31 J kg ⁻¹ mol ⁻¹
Molar volume of oxygen, ϑ_{O_2}	16.6×10^{-6} m ³ mol ⁻¹
Molar volume of nitrogen, ϑ_{N_2}	17.9×10^{-6} m ³ mol ⁻¹
Molar volume of water vapor, ϑ_{H_2O}	12.7×10^{-6} m ³ mol ⁻¹
Initial porosity of GDL, ε_{GDL}	0.78
Initial porosity of MPL, ε_{MPL}	0.7
Initial porosity of CL, ε_{CL}	0.2
GDL permeability, $K_{0,GDL}$	1×10^{-11} m ²
MPL permeability, $K_{0,MPL}$	1×10^{-14} m ²
Operating temperature, T	343 K
Thermal conductivity of BP, k_{BP}	110 W m ⁻¹ k ⁻¹
Thermal conductivity of GDM, k_{GDM}	20 W m ⁻¹ k ⁻¹
Thermal conductivity of membrane, k_m	0.45 W m ⁻¹ k ⁻¹
Surface tension, σ	0.0625 N m ⁻¹

Property, symbol	Value, unit
Anode and cathode inlet pressure, $P_{\{a,c\}in}$	1.5 atm
H ₂ and O ₂ reference concentrations, $c_{\{H_2,O_2\}}^{ref}$	{56.4, 3.39} mol m ⁻³
Electro-osmotic drag coefficient, n_d	1.2
Flow field plate conductivity, σ_{BP}	1×10^5 S m ⁻¹
GDL in-plane conductivity, σ_{xx}	2×10^4 S m ⁻¹
GDL through-plane conductivity, σ_{yy}	1000 S m ⁻¹
MPL in-plane conductivity, σ_{xx}	200 S m ⁻¹
MPL through-plane conductivity, σ_{yy}	60 S m ⁻¹
Poisson's ratio of GDLs, ν_{xy}	0.3
Poisson's ratio of bipolar plate, ν_{xy}	0.3
Poisson's ratio of the membrane, ν_{xy}	0.35
Young's modulus of bipolar plate, E_b [12]	10 GPa
Young's modulus of GDLs in in-plane direction, E_x	1 GPa
Initial values for anode and cathode relative humidity, RH_a , RH_c	0.4, 0.4
Condensation rate constant, k_{cond} [16]	100 s ⁻¹
Evaporation rate constant, k_{evp} [16]	100 atm ⁻¹ s ⁻¹
Enthalpy of vaporization, h_{lg} [19]	2.36×10^6 J kg ⁻¹
Membrane water absorption and desorption rate constants, k_λ	5.2×10^{-6} , 2.11×10^{-5} s ⁻¹

4.4.2 Mechanical properties

4.4.2.1 Membrane

Young's modulus of Nafion 112 is determined by Tang et al. [58] in terms of relative humidity and temperature. The corresponding values, given in Table 5, are entered into the model in terms of membrane's water content and cell temperature employing

the figure given in [73] for the relation between the relative humidity and water content.

Table 5 Young's modulus values at various temperatures and relative humidities for Nafion 112 [58].

Young's modulus (MPa)	Relative humidity (%)			
	30	50	70	90
$T=65^\circ\text{C}$	148	117	92	63
$T=85^\circ\text{C}$	121	85	59	46

The membrane is assumed to undergo linear deformation when subject to hygro-thermal loading. Visco-elasto-plastic behavior of the membrane was considered in the modelling using a combination of elastic-perfectly plastic model. The total strain in the membrane consists of elastic, hygral, thermal, and plastic strain components:

$$\epsilon = \epsilon^{el} + \epsilon^{sw} + \epsilon^{th} + \epsilon^{pl} \quad (76)$$

The amount of hygral and thermal strain is assumed to be linearly proportional to the water concentration and temperature, respectively as follows [69]:

$$\epsilon^{sw} = \beta(\lambda - \lambda_{ref}) \quad (77)$$

$$\epsilon^{th} = \alpha(T - T_{ref}) \quad (78)$$

where β is the membrane swelling-expansion coefficient and α is the thermal expansion coefficient. The values used for these coefficients are given in Table 6. λ_{ref} and T_{ref} are the values for stress free states for hygral and thermal expansions, respectively. In the simulations, the membrane is assumed to be initially hydrated at 30%. Swelling strain for Nafion 112 has been given as a function of relative humidity in [57]. However, in this study we relate the hygral strain to the membrane water content. Therefore, similar to [69], a polynomial is fitted to the swelling data at 65°C given in [57] in terms of membrane water content as:

$$\epsilon^{sw} = 0.0161\lambda - 0.04 \quad (79)$$

Assuming the membrane as an elastic material, stress-strain relationship is given as [69]:

$$\sigma = \underline{\mathcal{D}}\epsilon^{el} \quad (80)$$

which can be rewritten using Equation (76) as:

$$\sigma = \underline{\mathcal{D}}(\epsilon - \epsilon^{sw} - \epsilon^{th} - \epsilon^{pl}) \quad (81)$$

where σ represents the stress and $\underline{\mathcal{D}}$ is the elasticity matrix. Using the isotropic Hook's Law and assuming a linear response in the elastic region, the stress tensor, σ_{ij} can be obtained as [30, 57, 60, 70]:

$$\sigma_{ij} = \frac{E}{(1+\nu)(1-2\nu)} [\nu\epsilon_{kk}^{el}\delta_{ij} + (1-2\nu)\epsilon_{ij}^{el}] \quad (82)$$

where E is Young's modulus, $\epsilon_{kk}^{el} = \epsilon_{xx}^{el} + \epsilon_{yy}^{el}$, and δ_{ij} is Kronecker delta which is defined as:

$$\delta_{ij} = \begin{cases} 1 & \text{if } i = j \\ 0 & \text{if } i \neq j \end{cases} \quad (83)$$

To model the plastic constitutive response, J2-flow theory [78] is adopted where the von Mises yield function is defined as follows:

$$f(\sigma_{ij}, \epsilon^{pl}) = \sqrt{\frac{3}{2}S_{ij}S_{ij}} - \sigma^Y \quad (84)$$

where S_{ij} are the components of the deviatoric stress:

$$S_{ij} = \sigma_{ij} - \frac{1}{3}(\sigma_{xx} + \sigma_{yy})\delta_{ij} \quad (85)$$

and σ^Y is the yield strength of the material which is a function of water volume fraction and temperature. Membrane loses its strength and becomes softer with an increase in its water content. As reported in [58], the yield strength for membrane content of 2.48, 3.48, 4.72, and 7.51 is given inside the model as 4.43, 3.91, 3.48, and 2.69 MPa, respectively.

Table 6 Physical properties of different cell components.

Component	Behavior model	Coefficient of thermal expansion (α) (10^{-6} K^{-1})
BP	Linear elastic	5 [29, 30, 57]
GDL	Orthotropic, linear elastic	-0.8 [29, 30, 57]
Membrane	Elasto-visco-plastic	123 [29, 30, 57]

The plastic deformation happens when the components of stress tensor reach the yield stress and when $f(\sigma_{ij}) = 0$. Based on J2-flow theory, the plastic increment tensor directly correlates with the derivative of the yield function as:

$$d\epsilon_{ij}^{pl} = -\frac{\partial f}{\partial \sigma_{ij}} d\lambda \quad (86)$$

where $d\lambda$ is the plastic multiplier which is proportional to the increment of equivalent plastic strain [59] and calculated by the consistent relation ($df = 0$) during stress-hardening. Perfectly plastic model is assumed as the hardening model.

4.4.2.2 GDMs

Stress-strain relationship for a linear elastic material is given by:

$$\sigma = \underline{\mathcal{D}}\epsilon^{el} \quad (87)$$

where σ is stress, $\underline{\mathcal{D}}$ is elasticity matrix, and ϵ^{el} is the elastic strain in the medium. The calculation of the stress distribution in the GDMs is a two-dimensional problem accounting for stress components in x and y directions. Unlike other studies [25,29,30,40,41,43,68] where a constant Young's modulus is assumed for GDMs, in this model an orthotropic material is adopted where the inverse of elasticity matrix, stress and strain matrices are defined as:

$$\underline{\mathcal{D}}^{-1} = \begin{bmatrix} 1/E_x & -\nu_{xy}/E_y & 0 \\ -\nu_{xy}/E_x & 1/E_y & 0 \\ 0 & 0 & 1/G_{xy} \end{bmatrix}; \quad \sigma = \begin{bmatrix} \sigma_x \\ \sigma_y \\ \psi_{xy} \end{bmatrix}; \quad \epsilon = \begin{bmatrix} \epsilon_x \\ \epsilon_y \\ \epsilon_{xy} \end{bmatrix} \quad (88)$$

where E_x and E_y are the Young's modulus of the GDM for in-plane and through-plane directions, respectively. ν_{xy} is the Poisson's ratio and G_{xy} is the shear modulus for the shear stress ψ_{xy} and defined as $G_{xy} = 0.5E_x/(1 + \nu_{xy})$. The parameters are

uncoupled and can be calculated separately. The only coupling between two directions is defined by Poisson's ratio, ν_{xy} . The in-plane and through-plane mechanical properties for 20wt.-% PTFE-impregnated carbon paper of the type TORAY TGPH-060, comprising of microporous layer on one side, have been investigated by Reum [2]. Values for in-plane Young's modulus as well as Poisson's ratio are listed in Table 2. However, E_y is not a constant and changes according to the force applied over it. Clamping force applied on the boundary of cell in the y -direction, on the BP will directly influences the GDM structural properties since this component has the lowest Young's modulus compared to all other parts and therefore experiences the highest deformation upon application of compressive stress. According to [2], and the stress-strain curve extracted from their experiment on the mechanical strength test of GDM, Young's modulus changes approximately between 25 and 35 MPa, for the applied forces between 8 and 16 MPa corresponding to the GDL compression ratios of 35% and 45%, respectively (Figure 9). Same forces are applied on the cell to simulate the clamping force effect on the cell.

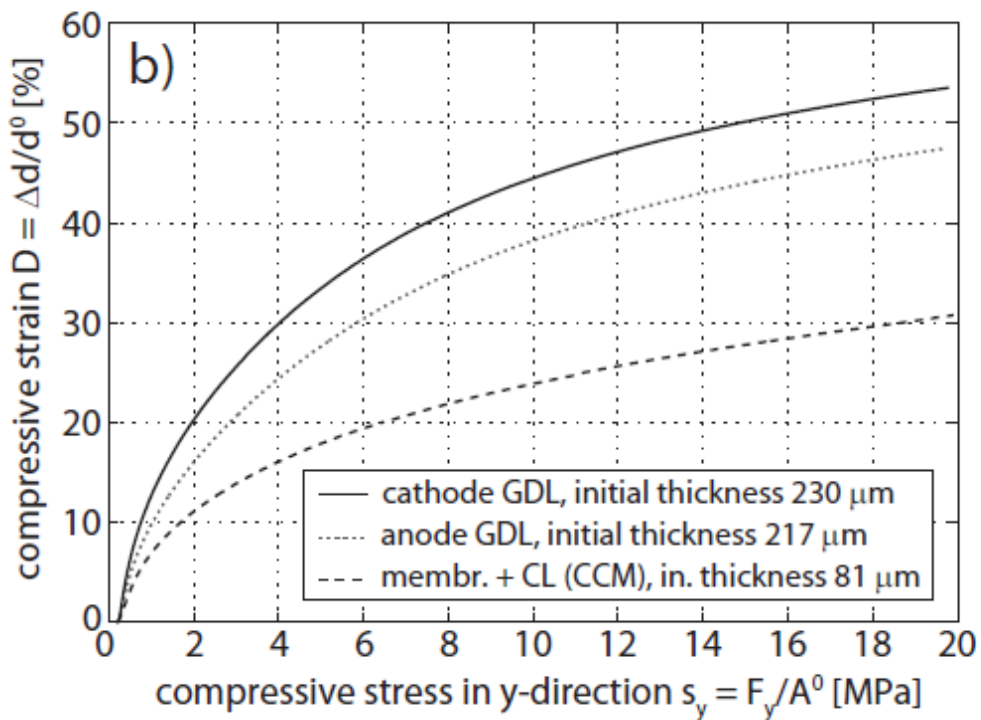


Figure 9 Compressive strain in terms of compressive stress given in [2].

4.4.3 Effective diffusivity and permeability

In order to properly simulate the effect of an inhomogeneous compression on the GDMs and their transport abilities, the model accounts for locally varying porosity field employing the volumetric strain of every element in the media. The new porosity, ε , after applying compressive force on the GDM can be defined as [80]:

$$\varepsilon = \frac{\varepsilon_0 + \epsilon_{kk}}{1 + \epsilon_{kk}} \quad (89)$$

where ε_0 is the initial porosity and ϵ_{kk} is the measured volumetric strain.

Diffusivity of the porous medium is a required parameter in Maxwell-Stefan Equation (40). There are several investigations available in the literature [6] evaluating the diffusion resistance of GDLs by estimating their effective diffusivity. Effective diffusivity is generally expressed as follows [36]:

$$D_{ij,eff} = (1 - s)^2 f(\varepsilon) D_{ij} \quad (90)$$

where $f(\varepsilon)$ is a relative function of porosity, which is incorporated in the form factor ε/τ where τ is the tortuosity. s represents the fraction of the GDL pores filled with liquid water and $(1 - s)^2$ accounts for the gas diffusivity in the pores of GDL.

The main finding in almost all reviewed investigations in [6] is that the Bruggeman correlation (based on idealized morphology model) [17] commonly used for $f(\varepsilon)$ significantly overestimates the effective diffusivity of the GDL. Therefore, it is strongly recommended to use empirical relations rather than the Bruggeman assumption. There are few ways to measure this parameter in a porous media. Flückiger et al. [5] used electrochemical diffusimetry method for this measurement in the GDL. They reported the values of effective relative diffusivity, ε/τ , in both directions in terms of porosity. Those given data in [5] are used to set up a case in which the anisotropic nature of the GDL is captured. This has been done by multiplying these form factors in diffusive flux equations in both directions. The data given for TGP-H-060 with 20% PTFE in [5] and illustrated in Figure 10 were fitted to exponential functions for in-plane and through-plane directions as:

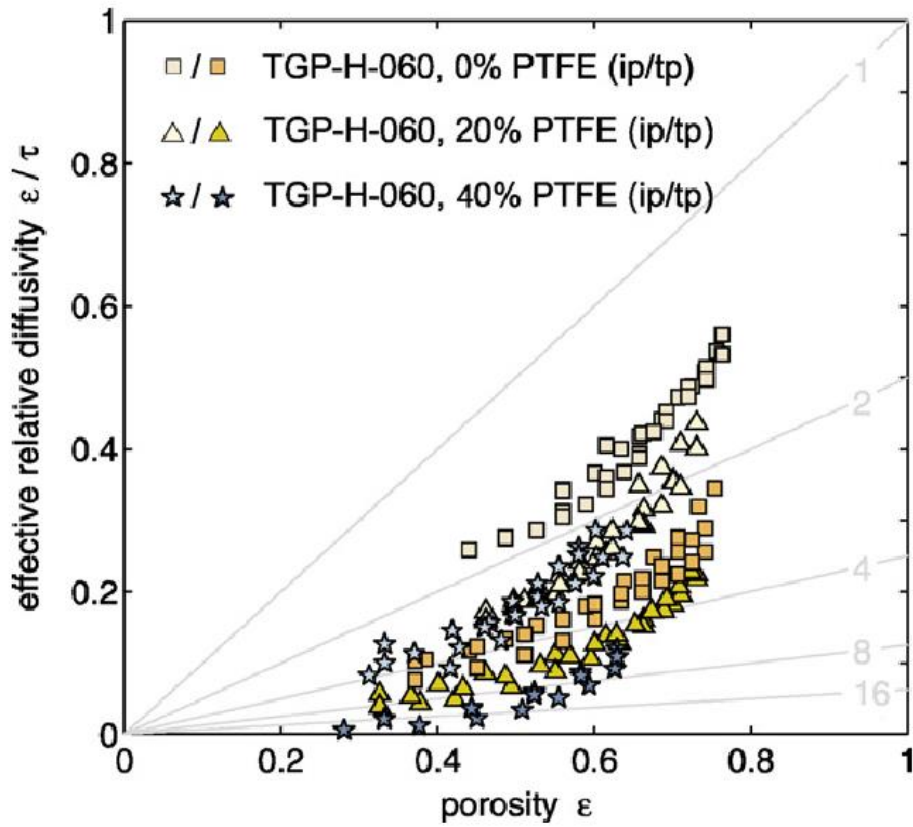


Figure 10 Effective relative diffusivity as a function of porosity for TGP-H-060 (adapted from [5]).

$$\varepsilon/\tau = \begin{cases} 0.04 \cdot \exp(3.6\varepsilon) & \text{in-plane} \\ 0.01 \cdot \exp(4.4\varepsilon) & \text{through-plane} \end{cases} \quad (91)$$

GDL's permeability is also changing due to compressive force. Distribution of permeation under the compressive force is in direct connection with the porosity. To model the relationship between porosity and permeability Kozeny-Carman equation is used [77]:

$$K = K_0 \frac{\varepsilon^3}{(1-\varepsilon)^2} \quad (92)$$

where K_0 is the absolute permeability and given for GDL and MPL in Table 4.

4.4.4 Contact resistance

The decrease of electrical and thermal contact resistances at interfaces under compressive force is an expected outcome on the cell performance. The relation between the compressive force and contact resistance at the interface between BP and GDM, is taken from [2]. Accordingly, electric-contact resistance changes between 4×10^{-7} to $0.7 \times 10^{-7} \text{ m}\Omega\text{cm}^2$, under compressive force between 0 to 20 MPa. Thermal-contact resistance is also assumed proportional to electric-contact resistance at the same interfaces. These data are entered into the model as boundary conditions at GDM-BP interfaces to account for the change in contact resistance between these two segments under compression

4.4.5 Reaction kinetics

Anodic volume reaction rate is calculated directly by the Butler-Volmer equation [36]:

$$j_a = j_{0,a}^{ref} \left(\frac{P_{H_2}}{P_{H_2}^{ref}} \right)^{0.5} \left[\exp \left(\alpha_a^{ox} \frac{F}{RT} \eta_a \right) - \exp \left(-\alpha_a^{rd} \frac{F}{RT} \eta_a \right) \right] \quad (93)$$

To account for the impact of the CL morphology on oxygen transport in the cathode CL, and accurately capture the activation and concentration losses, the reaction rate is modeled by an agglomerate approach given by Lin et al. [35]:

$$j_c = \frac{4F}{\frac{\delta_{NaF}}{a_{ratio} D_{O_2}^{NaF}} + \frac{\delta_{H_2O}}{a_{ratio} D_{O_2}^{H_2O}} + \frac{H_{O_2}^{H_2O}}{H_{O_2}^{NaF}} + \frac{1}{\xi k \eta}} \frac{P_{O_2}}{H_{O_2}^{NaF}} \quad (94)$$

The definitions and values of all parameters used in Butler-Volmer equations and agglomerate model are taken from [35, 36] and summarized in Table 7.

Table 7 Parameters in kinetic and agglomerate models [35,36].

Parameter	Relationship/Definition
Anode reference exchange current density	$j_{0,a}^{ref} = 1 \times 10^{11} \text{ A m}^{-3}$
Hydrogen reference concentration	$P_{H_2}^{ref} = 56.4 \text{ mol m}^{-3}$
O_2 diffusivity in nafion phase	$D_{O_2}^{Naf} = 3.1 \times 10^{-7} e^{(-2768/T)} \text{ m}^2 \text{ s}^{-1}$
Effective diffusivity of O_2 in the Nafion phase within catalyst pellets	$D_{O_2}^{Naf,pell} = D_{O_2}^{Naf} [(1 - \varepsilon_{CL}) \varepsilon_{pell}^{Naf}]^{1.5} \text{ m}^2 \text{ s}^{-1}$
O_2 diffusivity in liquid phase	$D_{O_2}^{H_2O} = 2.41 \times 10^{-9} \text{ m}^2 \text{ s}^{-1}$
Reference oxygen concentration	$C_{O_2}^{ref} = 5.24 \text{ mol m}^{-3}$
Henry's constant	$H_{O_2}^{Naf} = 1.33 \times 10^5 e^{(-666/T)} \text{ Pa m}^3 \text{ mol}^{-1}$ $H_{O_2}^{H_2O} = 5.08 \times 10^5 e^{(-498/T)} \text{ Pa m}^3 \text{ mol}^{-1}$
Overpotential	$\eta = \phi_e - \phi_m - \phi_{eq}$
Transfer coefficient	$\alpha_a^{ox} = \alpha_a^{rd} = \alpha_c^{ox} = \alpha_c^{rd} = 1$
Volume fraction of Nafion in catalyst pellet	$\varepsilon_{pell}^{Naf} = 0.39$
Radius of catalyst pellet	$r_{pell} = 1 \times 10^{-7} \text{ m}$
Thickness of Nafion around catalyst pellet	$\delta^{Naf} = 1 \times 10^{-8} \text{ m}$
Surface area of the agglomerates per unit volume of CL	$a_{ratio} = 2(1 - \varepsilon_{CL}) / (r_{pell} + \delta^{Naf})$
Reaction rate constant	$k_\eta = \frac{1}{4FC_{O_2}^{ref}} j_{0,c}^{ref} e^{[-(\alpha_c^{rd} F/RT)\eta_c]}$
Effectiveness factor	$\xi = [3\phi \coth(3\phi) - 1] / (3\phi^2)$
Water film thickness around catalyst pellet	$\delta_{H_2O} = s\varepsilon_{CL} / a_{ratio}$
Thiele modulus for spherical pellet	$\phi = \frac{r_{pell}}{3} \sqrt{k_\eta / [D_{O_2}^{Naf,pell} (1 - \varepsilon_{CL})]}$

4.5 Numerical approach

Finite-element code COMSOL Multiphysics® is used to solve the governing equations with corresponding initial and boundary conditions for steady state condition. Mesh independency criteria in the model is reached with a total of 4695 elements, with both quadratic and triangular Lagrange shape functions. A direct solver, MUMPS, with undamped Newton and relative tolerance of 10^{-6} is used in the simulations.





CHAPTER 5

RESULTS AND DISCUSSIONS

5.1 Preliminary results

Simulations were performed under basic parameters and different conditions and the outcomes were collected and presented in this section.

5.1.1 Force field

Figure 11(a) shows the cell configuration under the compressive force and its influence which is substantial on GDLs. The legend shows the von Mises stress distributions in the cell under compression. The corners in GDMs where they touches the BPs are shown to be critical and highly susceptible for deformation. Below that, Figure 11(b) is obtained from the experimental study done by Reum [1]. The structure of the GDMs and membrane under compressive force are almost identical in overall. The force is being applied in one side of the cell while the other sides taken as stationary walls (rollers) and the force mostly influences the GDL due its lowest Young's Modulus compared to other parts. The wireframe shows the cell when there is no compressive force on the model. The GDL thickness stays almost the same under the channel. The most significant effect of compression is on the region under the rib. The part under the rib gets thinner while the part under the channel remains as its initial thickness. This directly affects the porosity, permeability and diffusivity in the GDMs. The average of these parameters will be higher under the channel than under the rib. The change in thickness is symmetric in both electrode sides, so as the distribution of parameters, such as porosity and permeability.

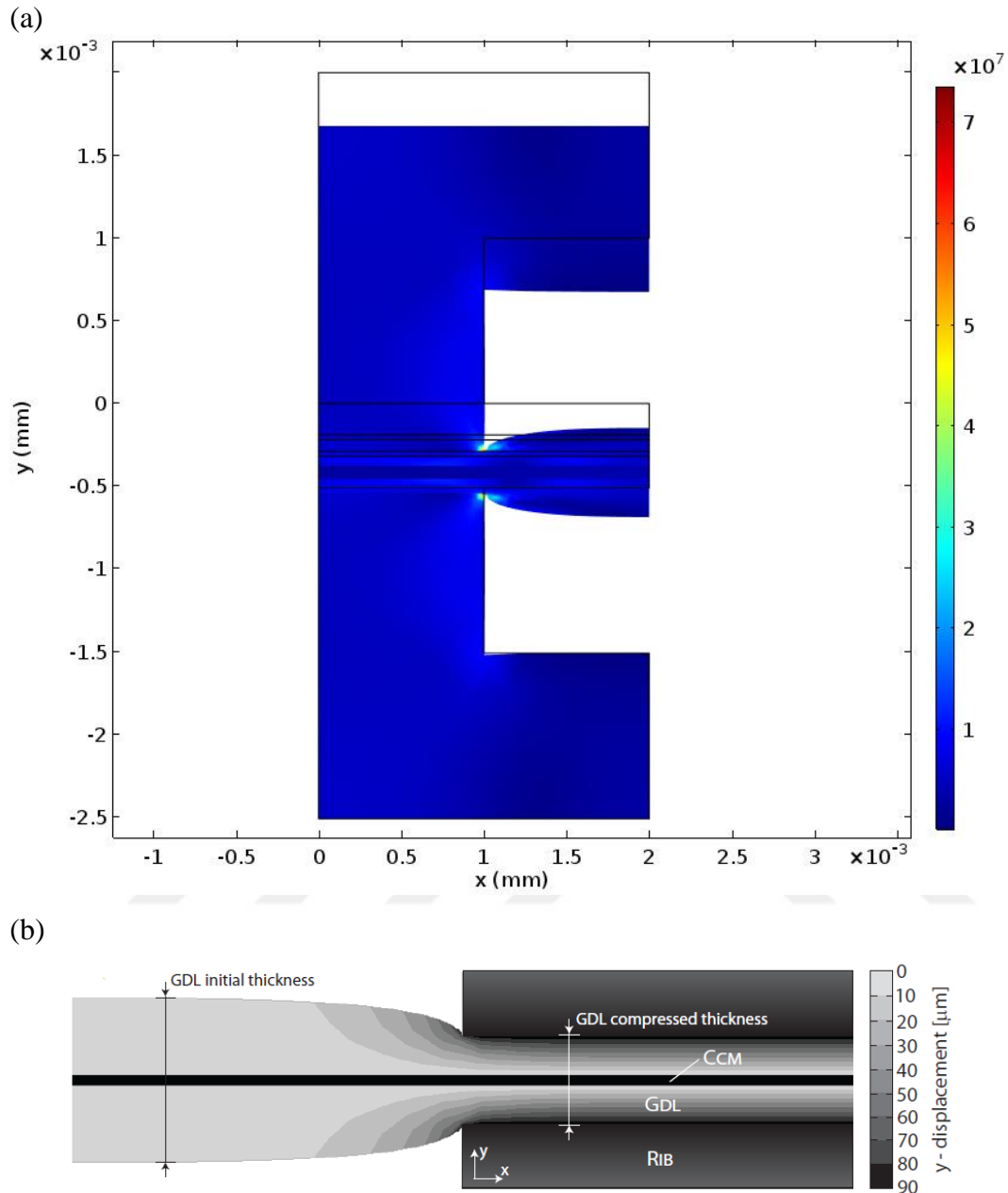


Figure 11 Cell configuration under compressive force (a) obtained from simulation and (b) given in [2].

5.1.2 Porosity distribution

The porosity distribution in GDMs is shown in Figure 12. As expected porosity under the rib where the compressive force is imposed is lower than the area under the channel where no force is acting. The porosity values are at the lowest at the corners

of the interface between the GDMs and BPs. The porosity variation is not substantial in the through-plane direction. However, the porosity difference between the GDL and MPL can be distinguished from the figure. As expected the porosity is lower in MPLs than GDLs.

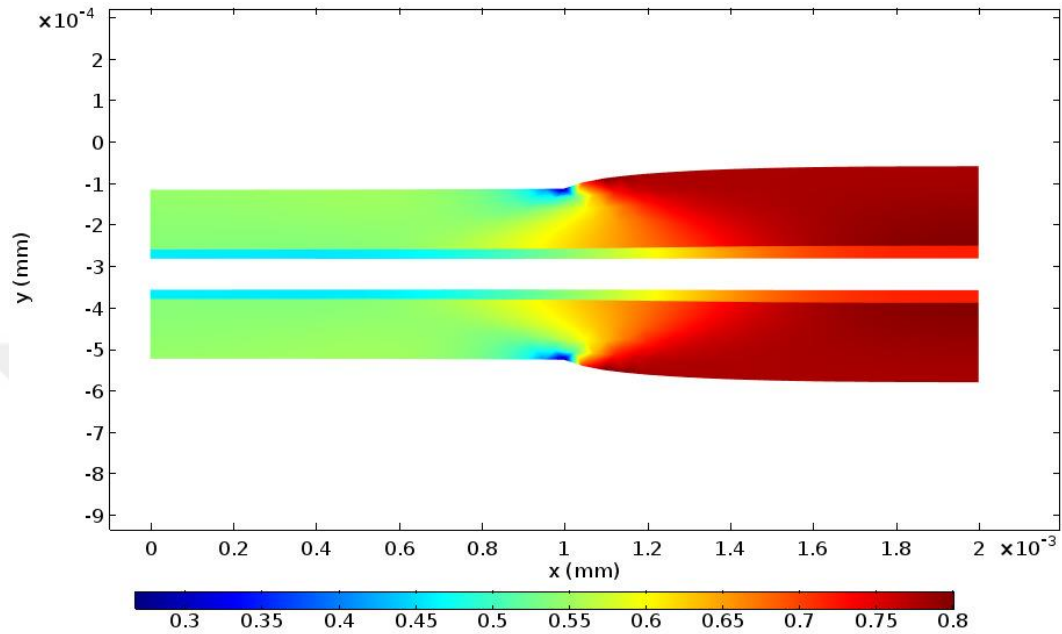


Figure 12 Porosity distribution in the GDMs.

5.1.3 Permeability distribution

Since permeability and diffusivity are in direct relation with the porosity distribution, thus similar results are expected for the distribution of these parameters throughout the GDMs as well. Figure 13 demonstrates the permeability contour in GDMs under compressive force. The distribution is consistent with the distribution of porosity; low under the rib section where force is applied and high under the channel section where no force is applied.

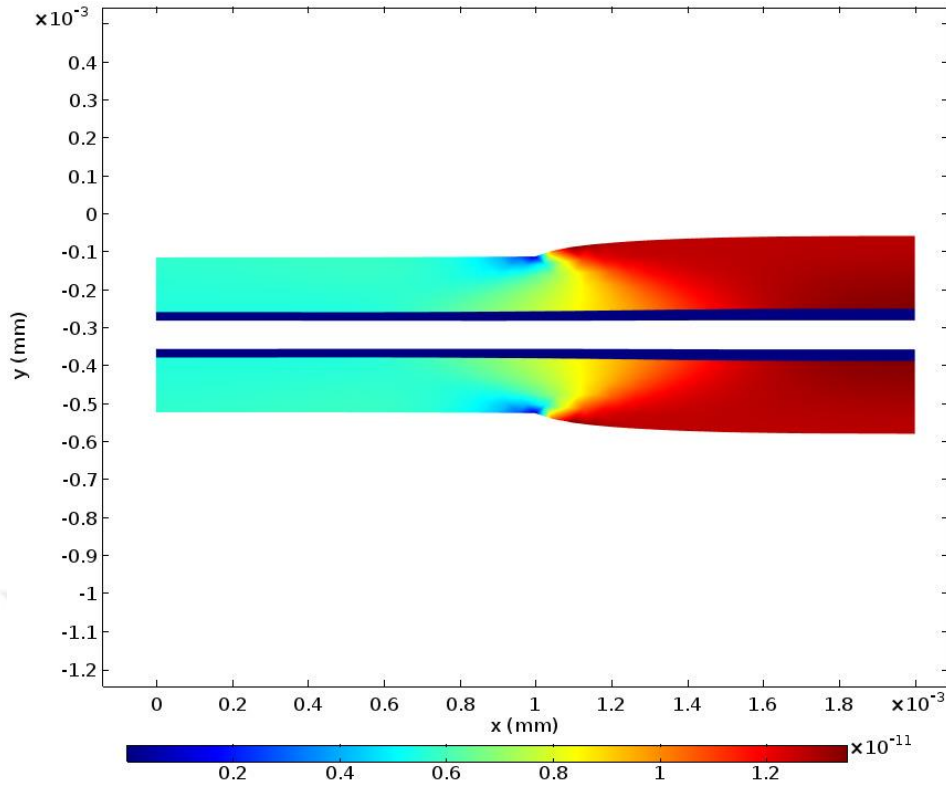


Figure 13 Permeability contour in GDMs (m^2).

5.1.4 In-plane and through-plane effective relative diffusivity distributions

The in-plane and through-plane diffusivity distributions are illustrated in Figure 14. Since the carbon fibers are generally lie on each other horizontally, therefore the diffusivity capability of GDLs are higher in the in-plane direction than through-plane direction. In-plane diffusivities are around double the through-plane diffusivities in the same locations throughout the GDMs. Applying compressive force the resistivity of the GDL to the mass transport increases under the rib. This is due to the reduction in the porosity values in this region under the compression. Since MPLs have lower porosities than GDLs, they show lower diffusivity values compared to GDLs.

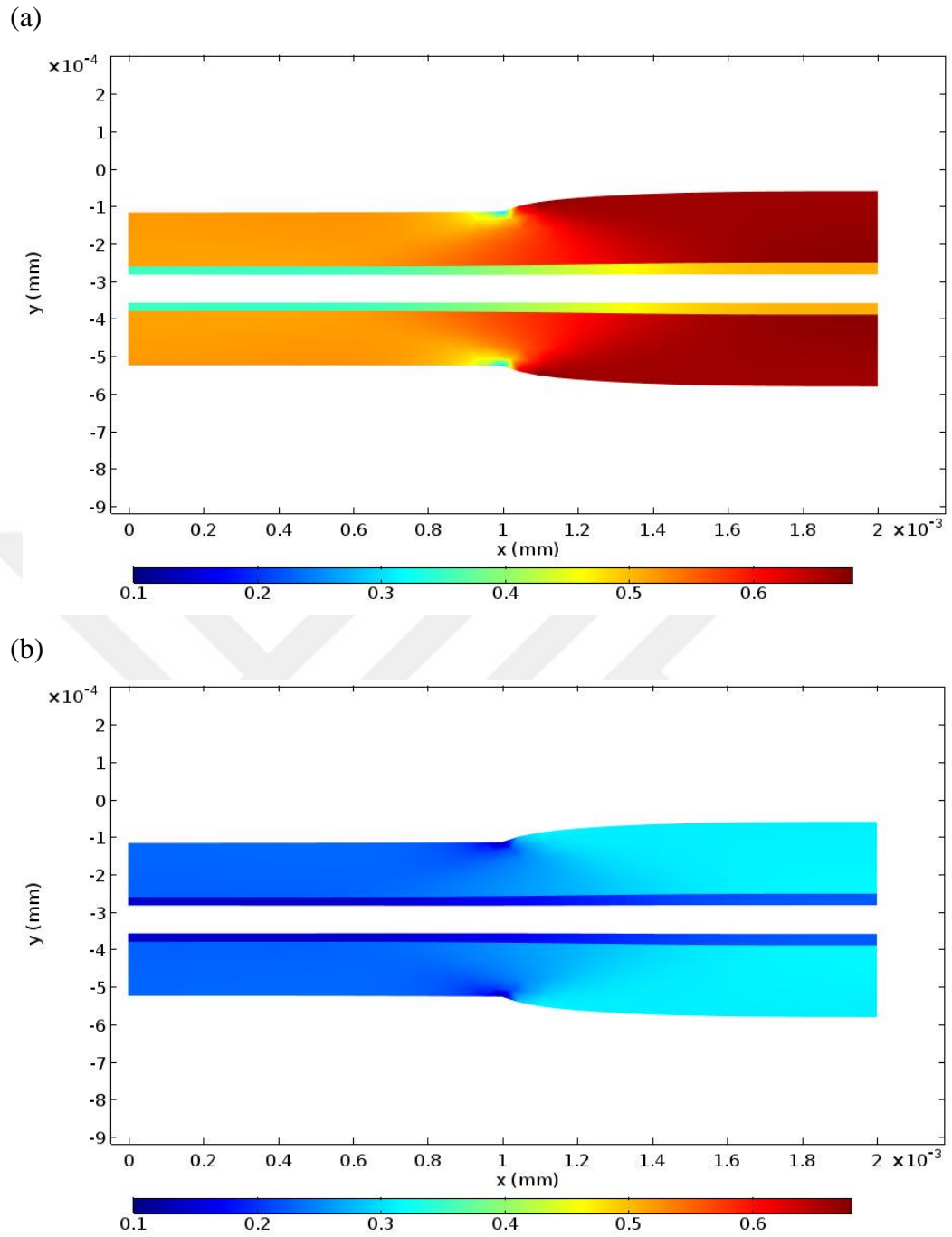


Figure 14 (a) In-plane and (b) through-plane effective relative diffusivity distributions.

5.1.5 Temperature distribution in an operating cell

Figure 15 illustrates the temperature distribution in the cell for a sample case. Heat generated from the electrochemical reaction and the condensation process take place in the cathode side, subject this side to higher temperatures. Highest temperature is seen under the channel compared to the region under the rib as expected due to higher reaction rate. Compression has also a direct impact over the local current density distribution over the channel/rib area. The current maxima move towards the region under the channel. This cause an increase in temperature rise in the area. This will be further explained in the next sections. The saturation pressure is in direct relation with the temperature. It was found that the temperature can rise by a few degrees leading to evaporation of liquid water. However, due to low temperature variation throughout the GDM, it does not present a significant impact on saturation pressure in this model.

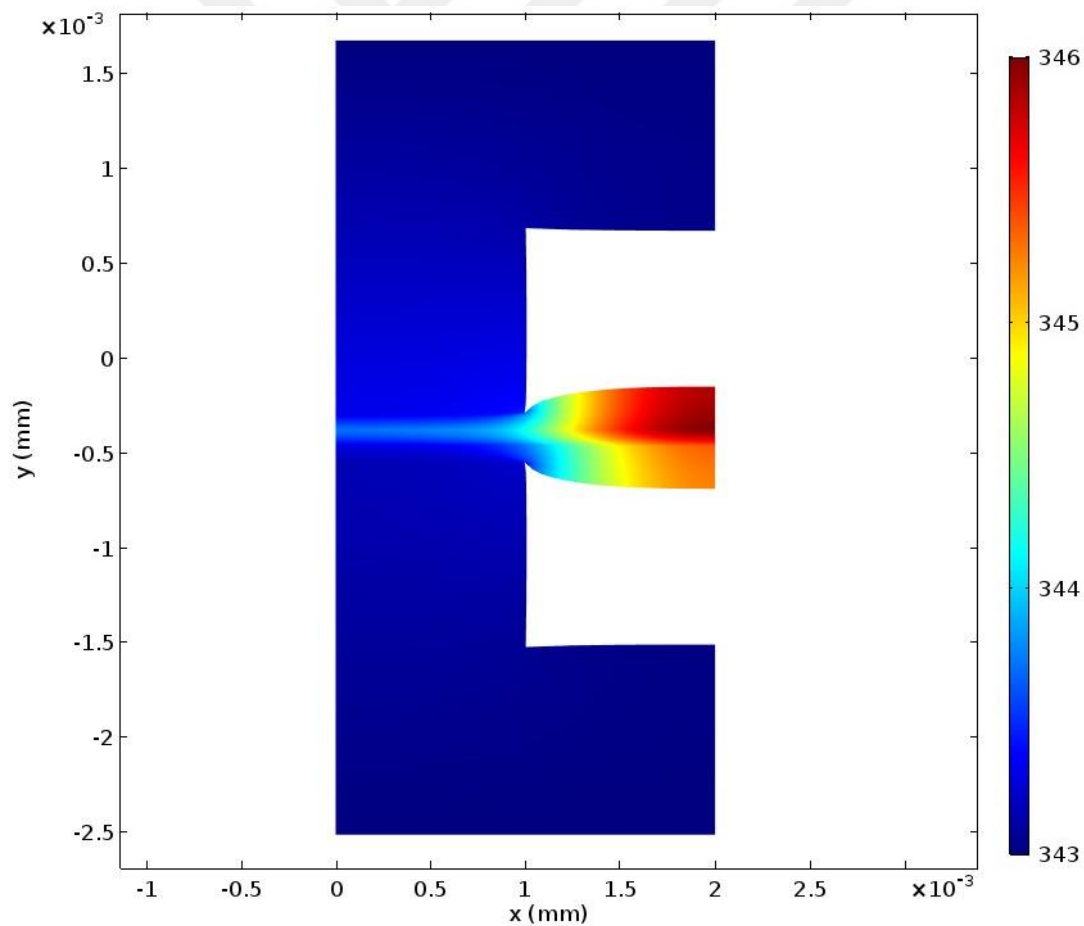


Figure 15 Temperature contour (K) [$I=1.2 \text{ A/cm}^2$, $\text{RH}_c=0.6$, $\text{RH}_a=0.4$].

5.1.6 Water distribution in an operating cell

Water production and evolution depends on both the water generated in the cathode side due to electrochemical reactions and water that presents in the anode inlet. The water transports by diffusion and convection throughout the cell. Water diffusing in anode GDM, carried though convection inside the membrane to cathode. Also water generated in cathode side, due to electro-osmotic drag can be brought to the anode side. Figure 16 shows the water concentration in the cell for the load current 0.4 A/cm^2 . The concentration is larger in the cathode side than the anode side throughout the cell. According to the figure for a specific operating parameters, minimum water concentrations in both electrodes as well as membrane are seen to occur under the channel. This can limit the cell performance. If anode gas becomes too dry, the membrane dries out, resulting in decreasing ionic conductivity. However, in the cathode side increase in water level, especially in this case under the rib, can clog the pores, brings flooding and hinder the gas transport to the active layer.

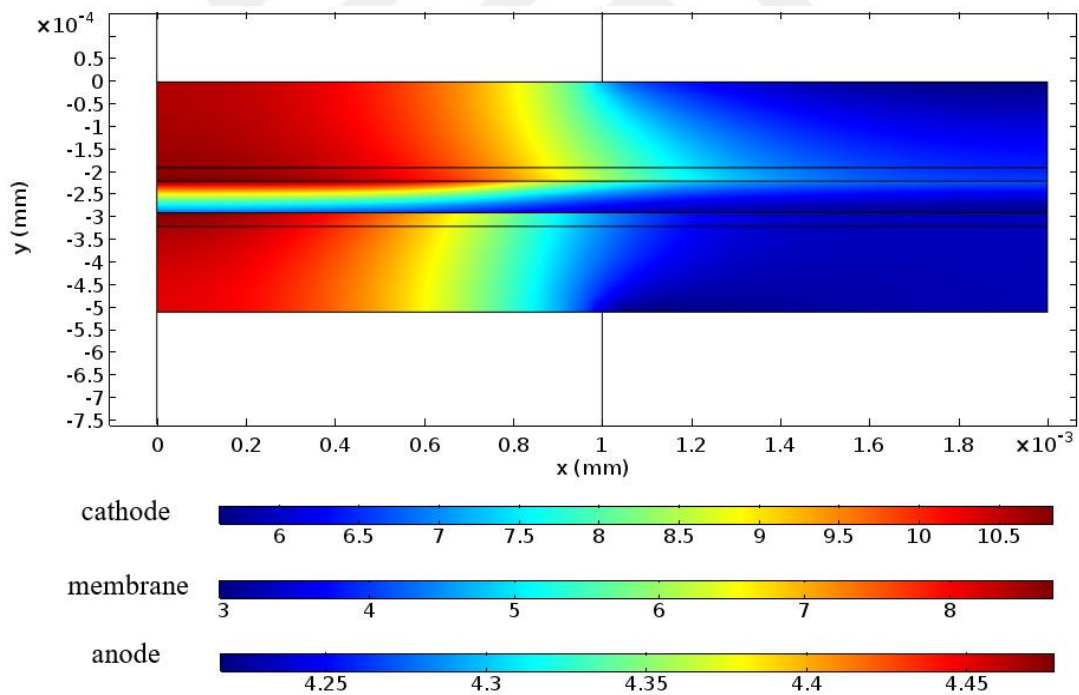


Figure 16 Water concentration distribution in a sample operating cell (mol/m^3).

The conductivity of the membrane is proportional to the temperature and its water content. The higher the water content the higher the conductivity. However, there are some controversies in the literature on the effect of temperature over its conductivity. Dehydration mostly happens in anode due to electro-osmotic drag from anode to cathode. This makes the conductivity and subsequently the water content in the side in contact with anode lower than the side in contact with cathode. Also in this particular case. The water generation magnitude is higher under the rib than under the channel which makes the water content under the rib to be higher than under the channel. The results show a minimum occurring in the lower corner of the membrane on the anode side. Dry gases in the anode cause a dry-out in the membrane, resulting in a decrease in ionic conductivity which limits fuel cell performance and increases the probability of cell failure.

5.1.7 Concentration distribution

Figure 17 and Figure 18 show the Hydrogen and Oxygen concentration in anode and cathode GDM, respectively. The figure shows that concentration variation is small along the thickness of the cathode, while it is substantial along the electrode's width. The concentrations decrease as the distance to the gas inlet increases. As expected, not only the close path under the flow channels lead to high concentration under these areas but also the compressive force has deleterious effect on distribution of mass fractions of Hydrogen and Oxygen by reducing the porosity under the rib. This distribution dictates the electrode's current generation at particular positions.

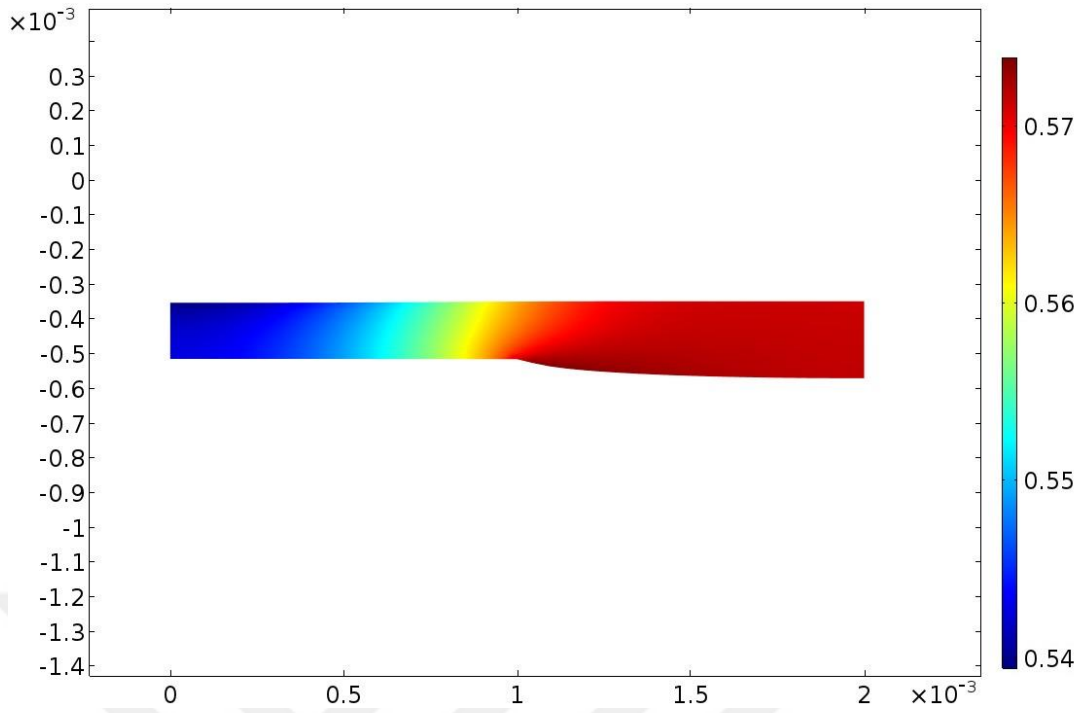


Figure 17 Hydrogen mass fraction distribution in anode.

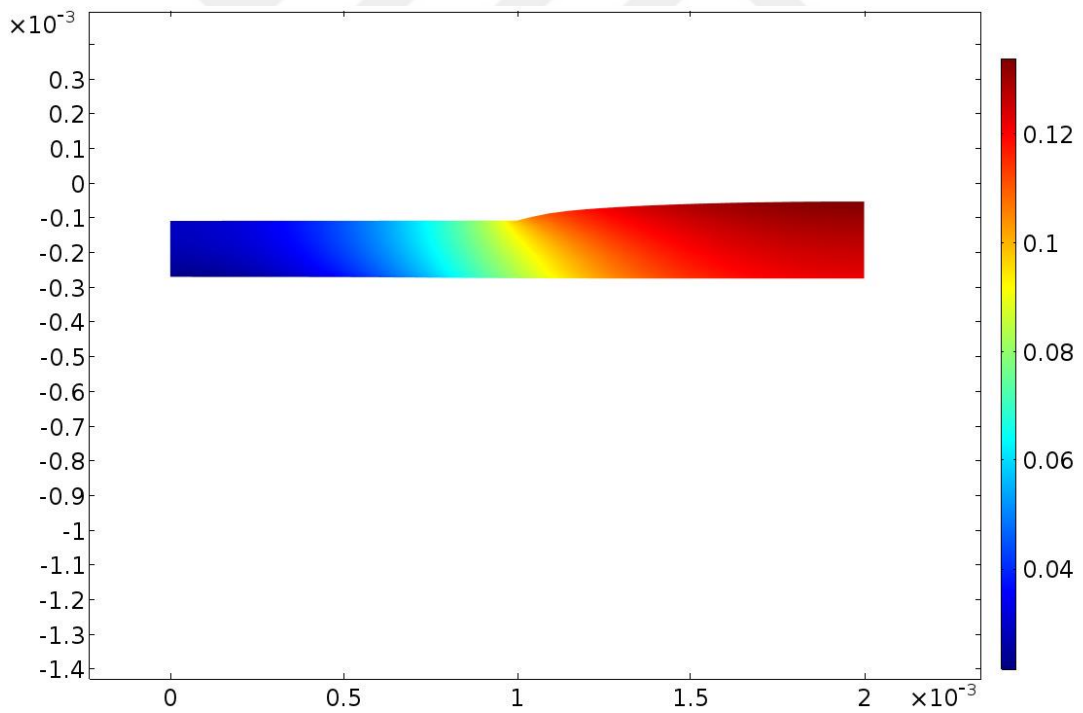


Figure 18 Oxygen mass fraction distribution in the cathode.

5.1.8 Liquid water distribution

Due to condensation/evaporation processes happen in the cathode, it is expected to have water in liquid phase in the cathode side. The result of a sample simulation for the liquid water distribution under current load of 1 A/cm^2 with inlet $\text{RH}_c=0.8$ is shown in Figure 19. Due to longer distance of the region under the rib to diffuse the liquid water towards the channel, the magnitude of liquid water is higher in this region. As seen the MPL at the bottom side of the GDM could help in diminishing the liquid saturation in this layer compared to GDL under the rib.

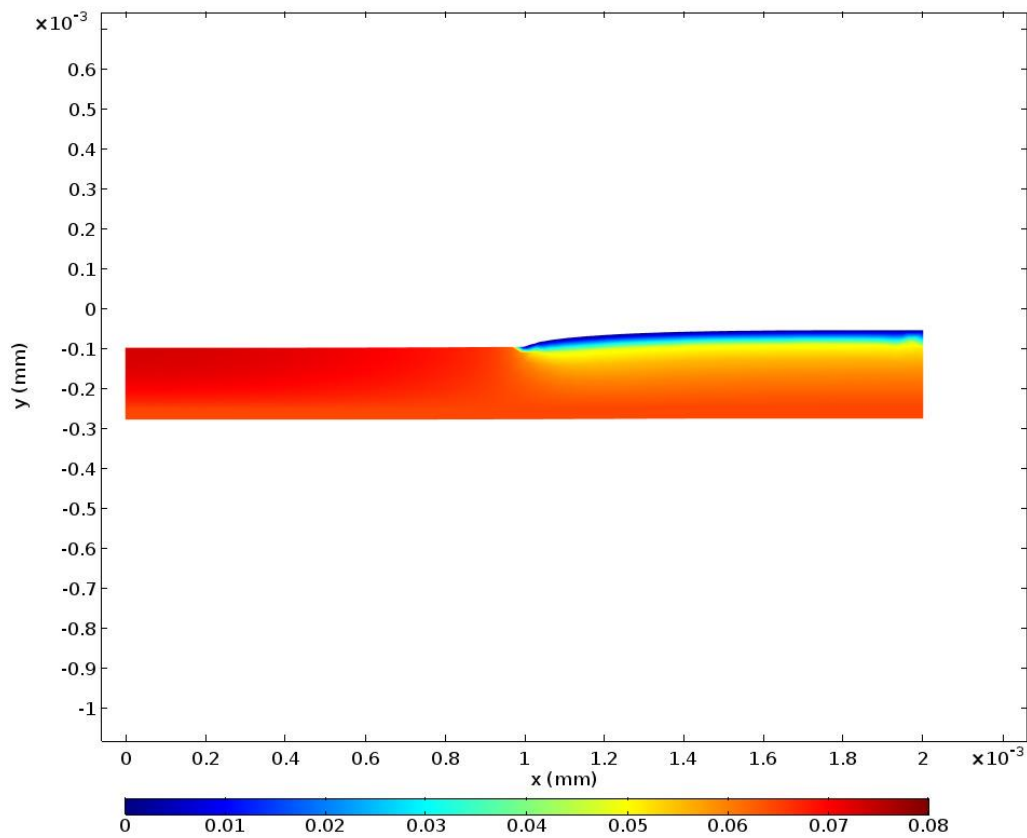


Figure 19 Liquid water distribution in the cathode GDM.

5.2 Parameter sensitivity analyses

Many physical and empirical parameters exist in the developed model that have great influences on the fuel cell characteristic. In this section, the sensitivity analyses performed for measuring the impact of some important parameters are presented.

Based on our model and the influence each parameter has on the cell performance, polarization curve is seen to be very sensitive to temperature, relative humidity, porosity and the associated diffusivity while it is less sensitive to permeability and inlet pressure.

Polarization curves for the cell with different operating pressures at both anode and cathode sides ranging from 1 to 2.25 atm are presented in Figure 20. Fuel cell performance improves with the rise in inlet pressure even though it is not substantial. Partial pressure increase of the reactant gases is the reason for the improved performance. The effect of temperature on the cell performance is also depicted in Figure 21. Among three cases chosen for the analyses, the cell performs better at higher temperatures. Improved diffusivity, membrane conductivity, and reaction kinetics are the reasons behind this performance enhancement.

The effects of humidity ratio, in both anode and cathode inlet streams, on overall cell performance are demonstrated in Figure 22. The higher the relative humidity in the anode side the better the cell performs. However, in the cathode side, by increasing the relative humidity of inlet air stream, the cell performs poorly due to water flooding. Despite the drop in performance predicted by this model, it is a common practice among fuel cell experimentalists to humidify both the anode and the cathode streams. While anode humidification is essential and showed to have a positive influence on the cell performance at all current densities by avoiding dehydration effects in the membrane, cathode humidification seems to be unnecessary and even harming by inducing significant reduction in performance.

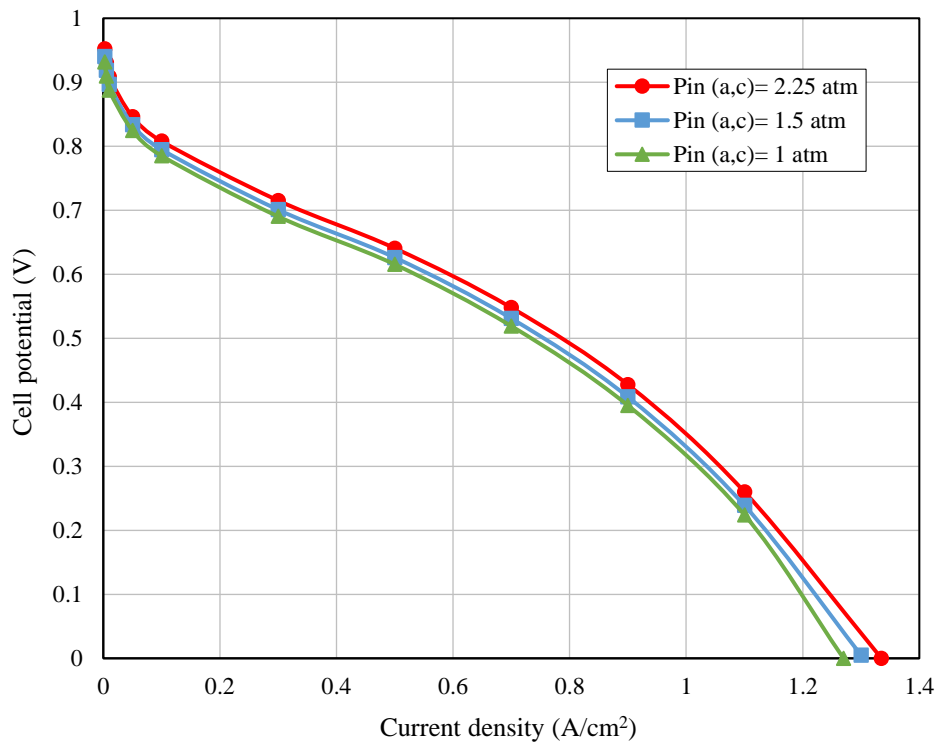


Figure 20 Polarization curves for different inlet pressures at anode and cathode.

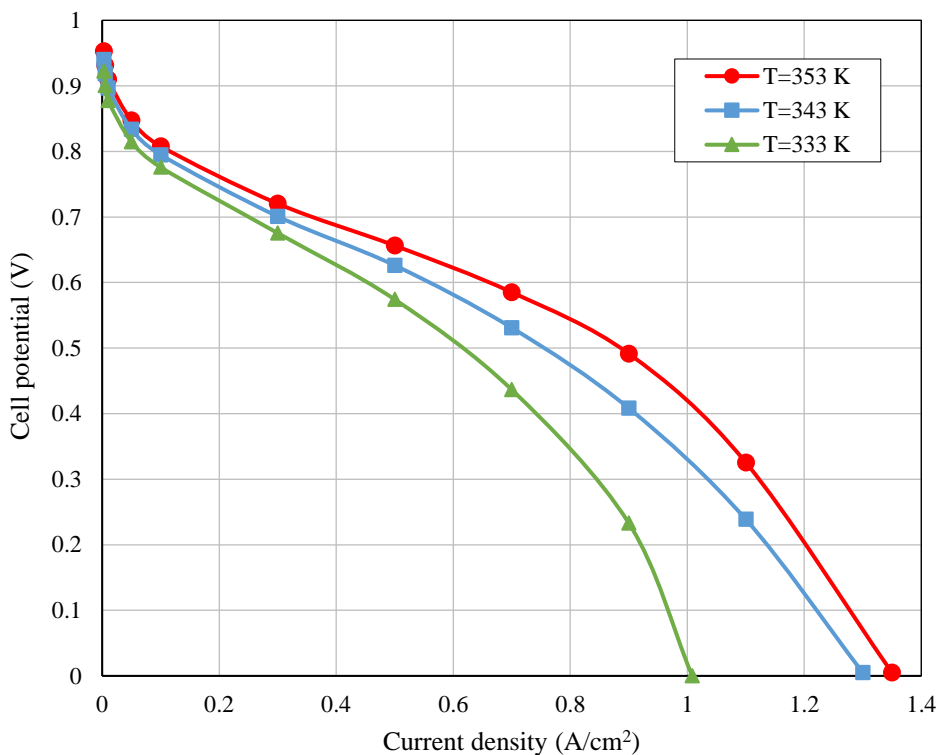


Figure 21 Polarization curves for different cell operating temperatures.

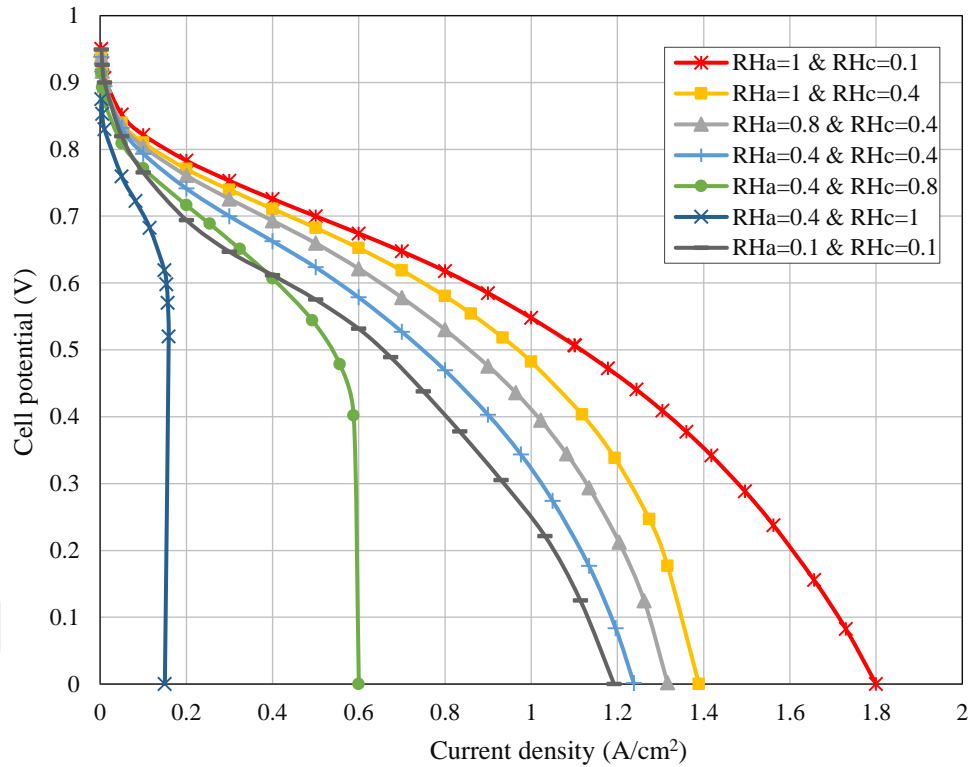


Figure 22 Polarization curves for various inlet humidification conditions.

Limiting current density is controlled by transport ability of the reactant which depends on the porosity and the liquid water distribution. With an increase in the relative humidity, the saturation of liquid water also increases, resulting in performance reduction. The worst cell performance is found under fully humidified air stream as a result of a greatly reduced oxygen transport rate.

The effects of the diffusion layer porosity on the performance of PEFC is exhibited in Figure 23. Low levels of porosity brings higher mass transfer resistance in the cell and deteriorates its performance. The simulation results show that the effect of the diffusion layer porosity on the PEFC performance is significant in high current loads between 0.6 to 1.3 A/cm². The porosity has the most impact on the concentration polarization region as expected.

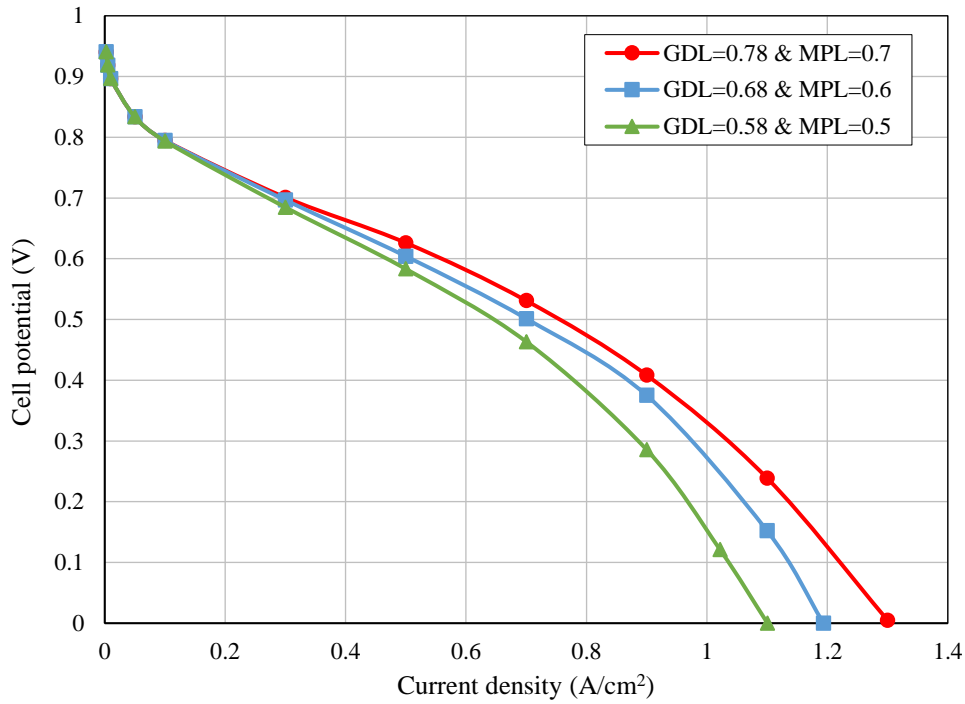


Figure 23 Polarization curves for different porosity values assumed in GDL and MPL.

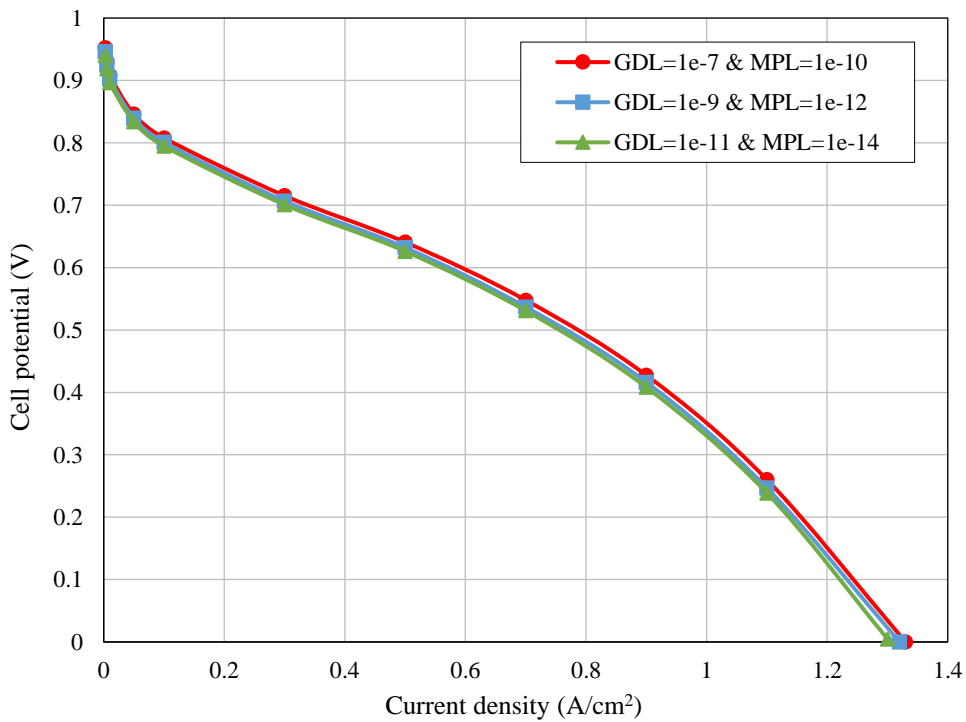


Figure 24 Polarization curves for different permeability values assumed in GDL and MPL.

The effect of the diffusion layer absolute permeability on the PEFC polarization curve is shown in Figure 24. Three cases with specified intervals starting from the base case permeability values which are 10^{-11} for the GDL and 10^{-14} for the MPL are examined. As seen, raising the permeability does not enhance the performance significantly.

In order to find out the effect of the selected effective relative diffusivity model on the cell performance, two cases are simulated which differ only in the relation between the effective relative diffusivity in terms of porosity; one assuming the anisotropic nature of GDL, and one using the Bruggeman assumption. Figure 25 shows the polarization curves generated for those two cases. According to this figure, performance has been overpredicted using Bruggeman assumption compared to the much realistic anisotropic case. This is attributed to the overestimation in the amount of oxygen for the reaction that can easily be justified by the calculated effective relative diffusivity in terms of porosity which is higher than the case where the GDL assumed as anisotropic media.

Of great interest is the influence of changing each parameter for diffusive flux either in through-plane or in-plane direction to see their influences on overall cell performance. In an attempt, diffusivity coefficients are doubled in each direction keeping other parameters as before. The result is presented in Figure 26. As seen doubling through-plane merely improves section related to concentration polarization in higher load values. Therefore, higher through-plane diffusivity is essential to reach higher limiting current densities. But doubling in-plane diffusivity has an impact on longer range of current load values and improves the performance more noticeable than modifying the diffusivity in through-plane direction. Increasing the diffusivity in the in-plane direction improves the diffusion in the in-plane direction and helps in providing the gas along the membrane surface and over the reactive surfaces especially in the region under the rib where compressive force has been applied.

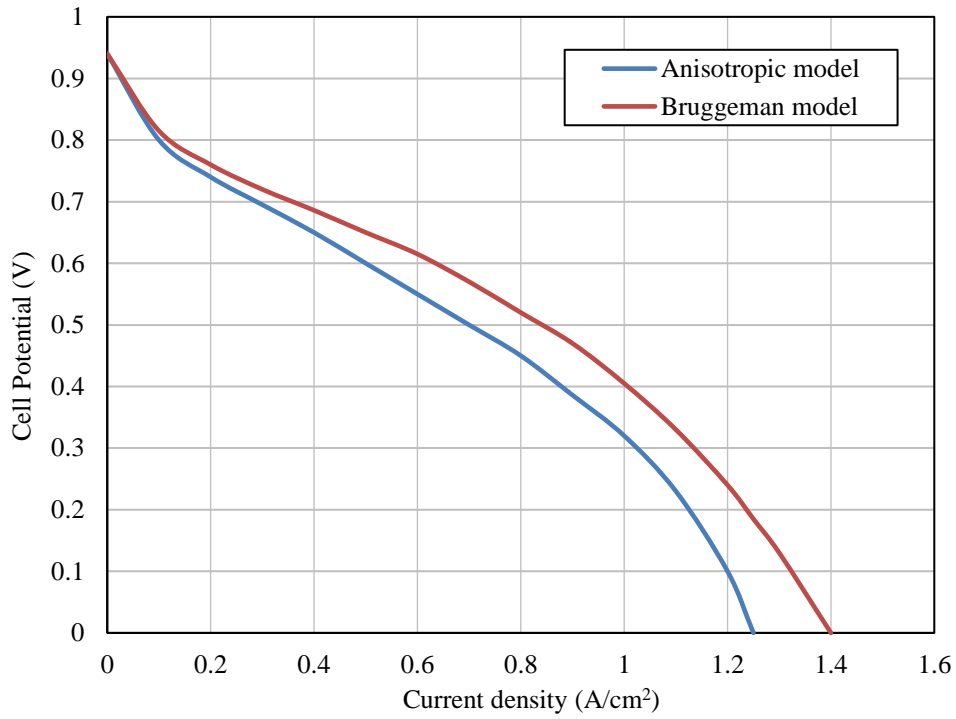


Figure 25 Performance comparison between cases with anisotropic effective relative diffusion and Bruggeman assumption assumed in GDLs.

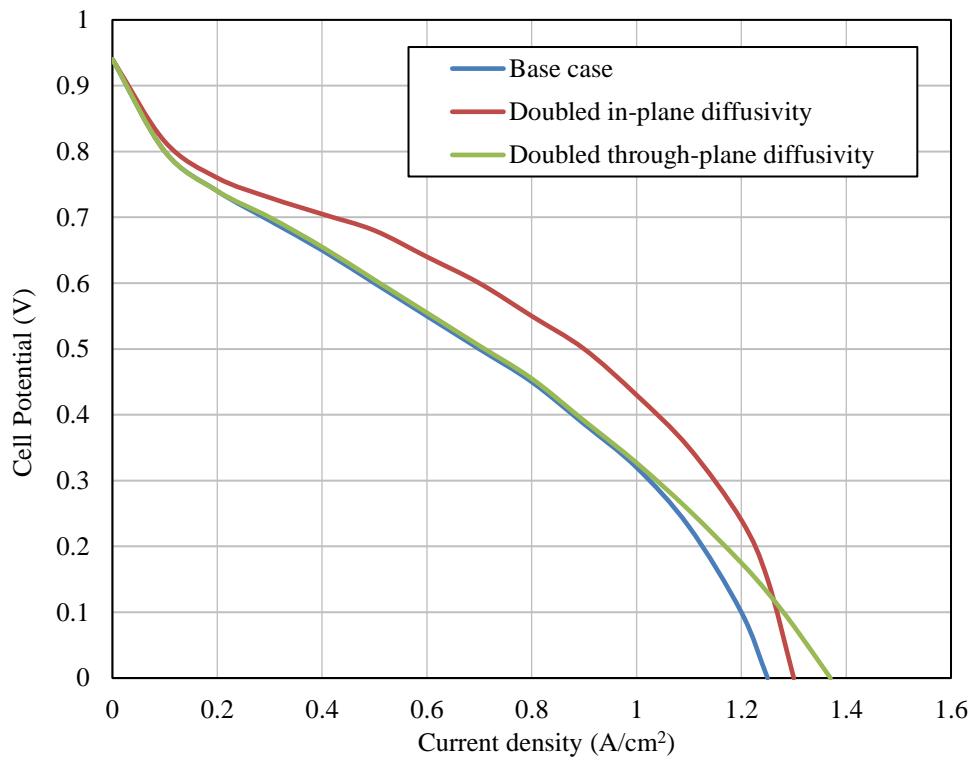


Figure 26 Performance curves for different cases of diffusivities in GDLs.

5.3 Model validation

All the parameters and variables used in the model are discussed in previous work and similar to the ones given in the experimental study [2]. However, as discussed in Section 5.2, different parameters can bring the same voltage-current characteristics in the cell. Therefore, the process of validation with polarization curve is not sufficient and local current density curves are also required to be verified.

As a first step, the simulation results are validated against the measurements of experimental study reported in [2]. The computed polarization curve from the model for three GDL compression cases, starting from the initial value of 35% and increasing stepwise by 5%, are compared with the ones given in [1,2] in Figure 27(a). The compression ratio used for the GDL indicates the percentage of GDL squeezed, which is defined as the ratio of reduced GDL thickness versus its uncompressed thickness (compression ratio = $1 - \delta/\delta_0$). A good agreement with only 6.92% deviation in whole range from low to high current densities has been achieved. Mechanical deformation of fuel cell components under compression on one hand reduces the contact resistance inducing maximum local current density. But on the other hand, it reduces porosity and permeability via volumetric shrinkage and impedes gas and liquid transport, leading to reduction in cell performance. However, based on Figure 27(a), the overall cell performance is decreased even with small variation of compression showing that mass transport resistance has a significant impact compared to contact resistance.

Channel-rib current distribution data calculated in this study for the base case ($RH_c=RH_a= 0.4$, compression ratio= 35%) is shown in Figure 27(b) together with ones measured in [2]. The distribution is taken at the membrane-GDM interface in the anode side. As expected, local current density is lower under the rib area due to limited oxygen transport. A reasonable agreement is achieved for all current loads. It should be noted that the current distribution given in [2] had a symmetrization process over its data obtained from the cell. Loading conditions directly impact the patterns of current density distribution. At low load, the maximum current density is seen

under the land area. As the load increases, the current density maxima shift towards the center of the channel. In our numerical simulations, local current density decreases under the rib and increases under the channel, while, in the experimental study, local current density increases in both regions, unexpectedly.

While this is not consistent with the experimental results, it agrees with the current distribution given by [49,50] implying the need for further experimental research with equipment capable of spatial resolution finer than 0.5 mm.



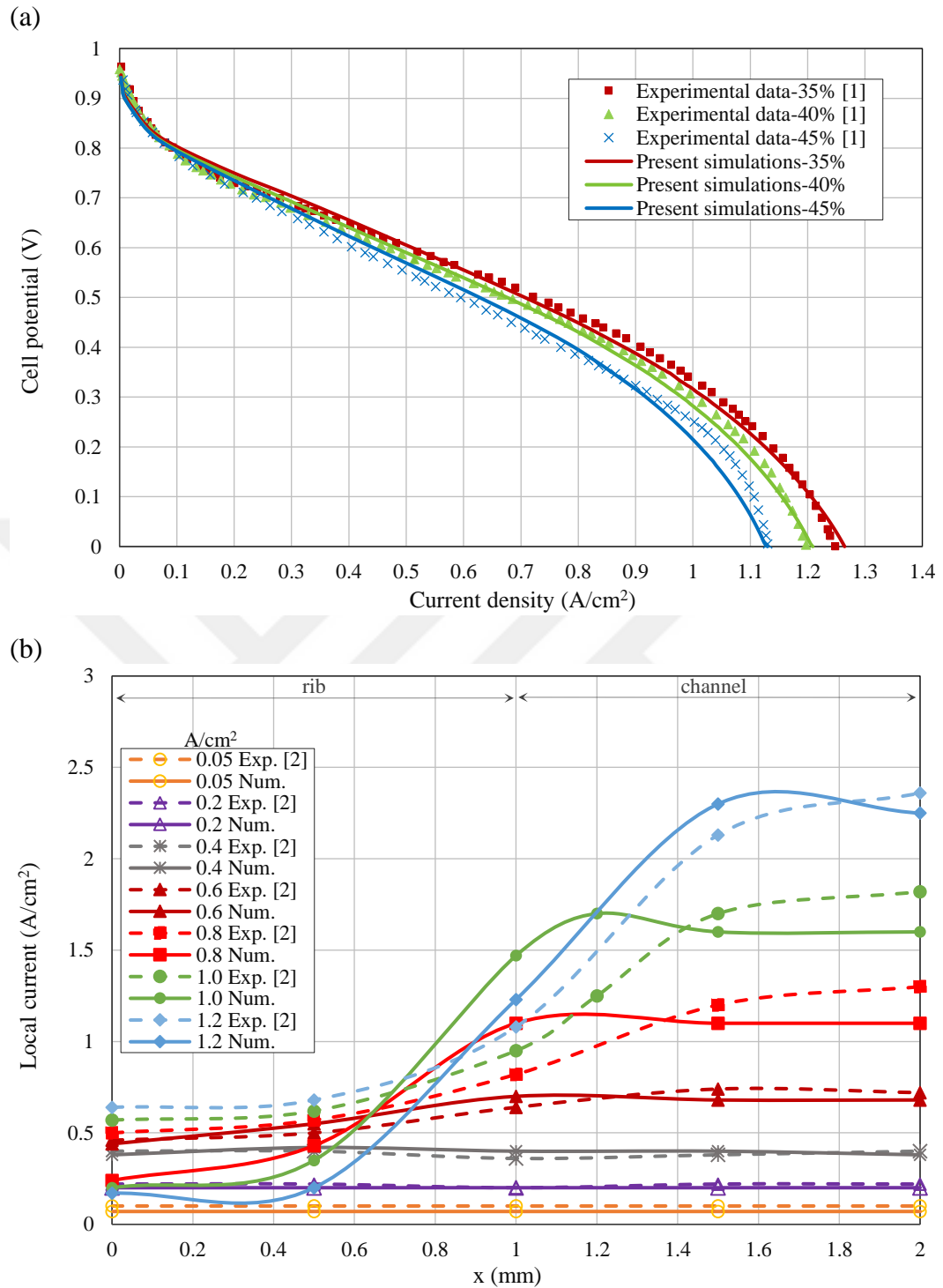


Figure 27 (a) Performance curves and (b) in-plane current density distributions for different current loads and comparison with experimental data [1,2]. The in-plane current density distribution is probed at the membrane-GDM interface in the anode side ($RH_c=RH_a=0.4$).

5.4 Influence of operating parameters on local performance

5.4.1 Effect of compression on porosity and effective relative diffusivity distributions

Implementing the compressive force directly affects the porosity values in GDMs. This impact is non-uniform, meaning the porosity under the rib will be lower than the area under the channel. Moreover, as discussed in Section 4.4.3, effective diffusivity is in direct correlation with form factor, ε/τ . According to Equation (91), porosity change influences the form factors in both in-plane and through-plane directions.

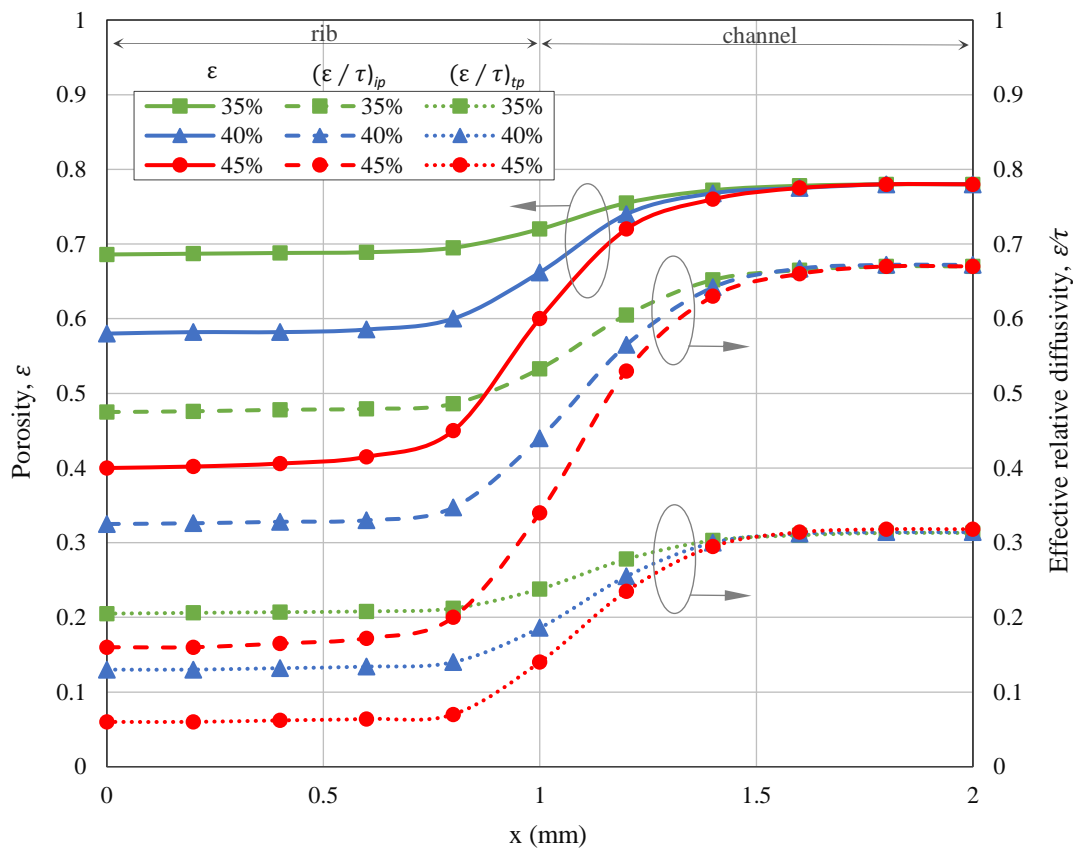


Figure 28 Porosity (lines), in-plane (dashed lines) and through-plane (dotted lines) effective relative diffusivity distributions for three different compression cases.

Data are extracted over the mid-plane section of GDL.

Local values for porosity, in-plane effective relative diffusivity, $(\varepsilon/\tau)_{ip}$, and through-plane effective relative diffusivity, $(\varepsilon/\tau)_{tp}$, with three compression cases are

given in Figure 28. Those values are collected over the mid-plane section of GDL in the model. As expected compressive force mostly deforms the domain under the rib, decreasing the thickness and the porosity while central region under the channel almost has no deformation and does not undergo a significant change in porosity and dependent values. As the compression increases, the values for porosity, $(\varepsilon/\tau)_{ip}$, and $(\varepsilon/\tau)_{tp}$ decrease under the rib. Due to inherent horizontal preferential directions of carbon fibers in GDL, in plane form factors are greater than the through-plane ones.

5.4.2 Effect of compression on in-plane local properties

In order to clarify how the compression affects the local cell performance, the modeling results are compared with an ordinary model excluding the compression effect and assuming constant GDL parameters. The compression ratio is fixed at 35% for comparisons.

The oxygen mass fractions over the CL for three different current loads and for two cases, one with compressive force and one free from compression, are shown in Figure 29. The distributions are taken at the GDM-membrane interface in the cathode side. Inherently, compressive force decreases the oxygen transport under the rib when porosity and permeability decrease, and tortuosity increases. Oxygen concentrations drop due to diffusion limit at high current densities, and liquid water formation worsens that limit.

Under the channel, the biggest distinction between two cases is seen with 0.75 A/cm^2 current load, where the liquid water formation intensifies and further obstructs the oxygen transport to CL. Almost half of the total area under the rib exhibits very low mass fraction of oxygen, implying that the GDL under the rib is severely flooded.

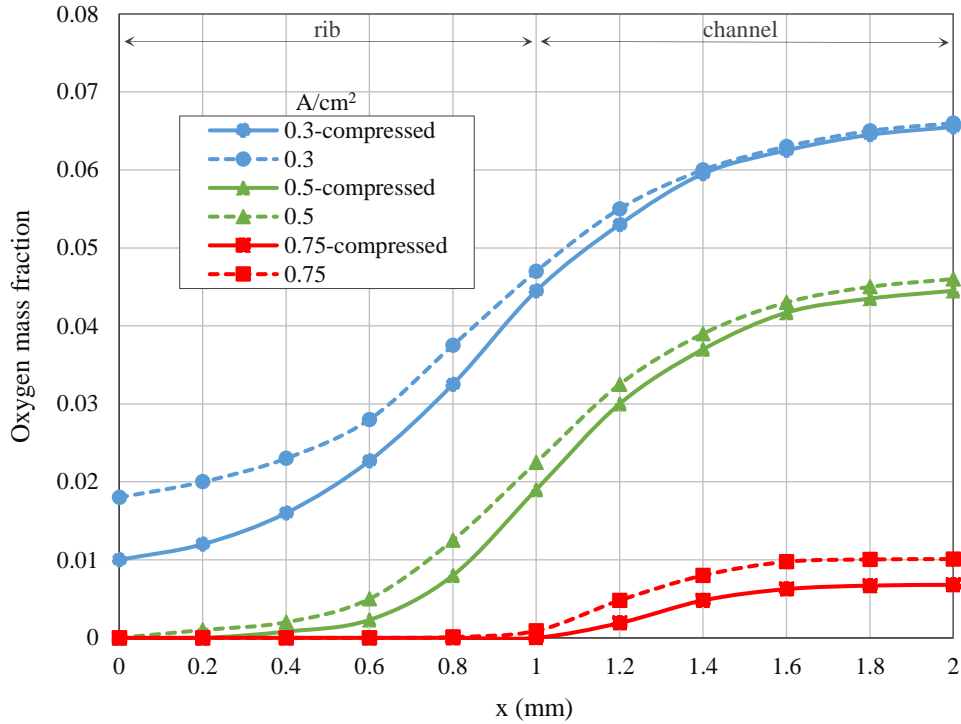


Figure 29 In-plane oxygen mass fraction distribution for three different current loads with and without compression ($I=0.75 \text{ A/cm}^2$, $\text{RH}_c=0.7$, $\text{RH}_a=0.4$).

Compression impacts on the in-plane current distribution and the rate of phase change are illustrated in Figure 30 for a sample current load of 0.75 A/cm^2 . Data are collected at the membrane-GDM interface. Under compression, water accumulation becomes higher under the rib because of the reduction in the porosity and the permeability. Oxygen concentration is therefore lower in that region, leading to lower local current density. Under galvanostatic operation, local current density decreases under the rib and increases under the channels exacerbating the non-uniformity of the current distribution in the cell.

Similar trends are also observed in the phase change rate distribution. Negative and positive values indicate evaporation and condensation, respectively in the figure. The compressive force influences both the condensation and evaporation rates. The rate of condensation increases under the channel while the rate of evaporation increases under the rib. This leads to higher rates of water production and thus greater amounts of liquid water under the channel at higher current loads. Not accounting for the

compression impact on the phase change rate would underpredict or overpredict the liquid water fraction in the GDMs. However, the liquid volume accumulation is not only controlled by the production rate, but also transport rate, which itself depends on Darcy resistance and operating conditions.

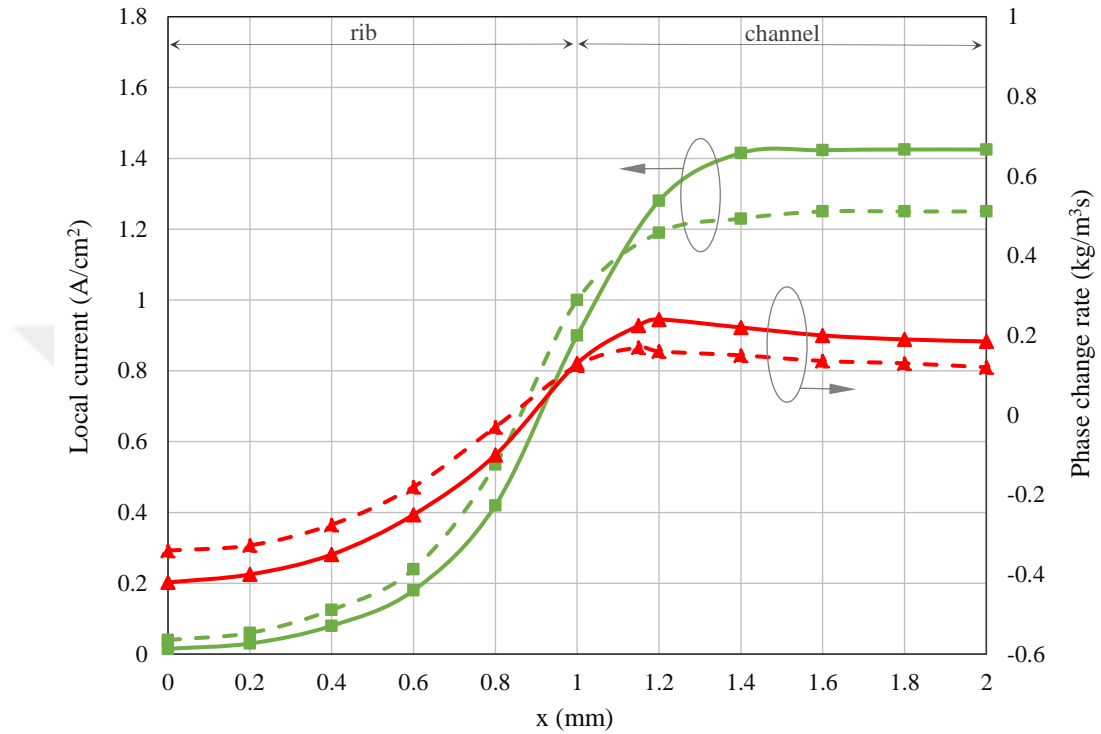


Figure 30 In-plane current density and phase change rate distributions for the case with compression (normal lines) and the case free from compression (dashed lines) ($I=0.75 \text{ A/cm}^2$, $RH_c=0.7$, $RH_a=0.4$).

The analyses reveal the importance of effective transport of reactants and liquid water formation on in-plane current distribution. The local transport properties of the compressed GDL i.e. porosity and diffusion pathways are responsible for gradients of oxidant and water, leading to inhomogeneous reaction and phase change rates across the channel and rib.

5.4.3 Effect of inlet relative humidity on local cell performance

At the same current load of 0.65 A/cm^2 , local current densities at the GDM-membrane interface predicted by the model are compared in Figure 31 for different air stream relative humidity values. With dry gases, $\text{RH}_c \leq 0.1$, very little water is available from the gas channel for membrane hydration. Therefore, ionic conductivity relies on hydration by product water [2]. However, the water available for the membrane hydration is in competition with evaporation to the channel. Therefore, membrane is better protected from drying under the rib with longer water diffusion pathways, resulting in the majority of the current to be produced in this region. At high relative humidity values, $\text{RH}_c \geq 0.6$, transport of water from the membrane to the channel is restricted to excess water from the electrochemical reaction in the GDL. The area under the channel, with short diffusion pathways, benefits from lower mass-transport restrictions compared to area under the rib and generates higher local current densities.

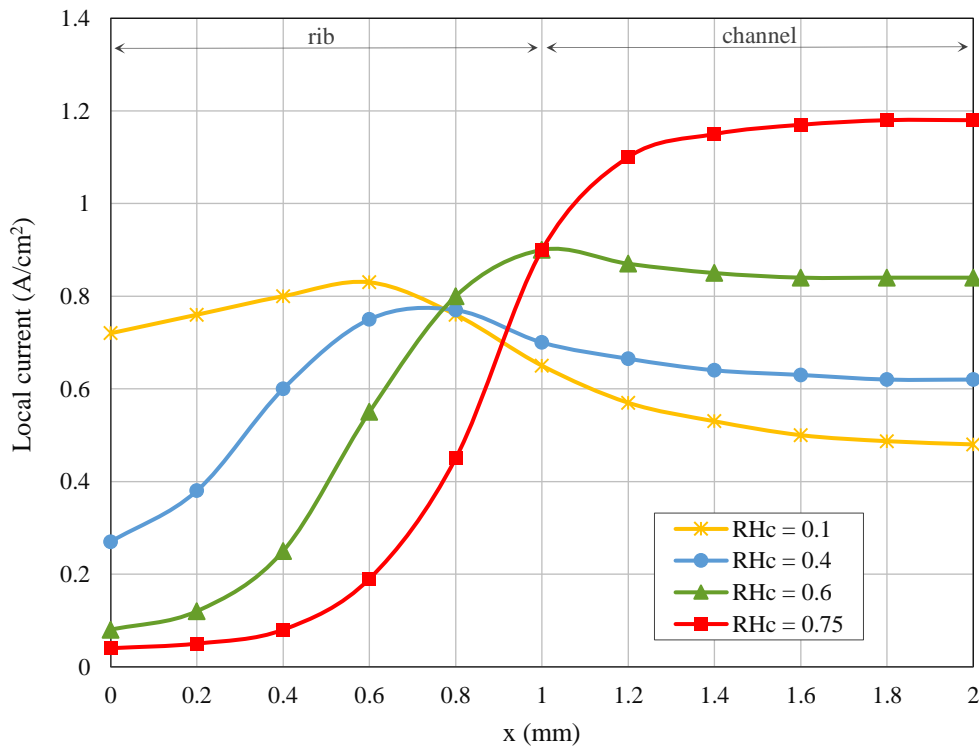


Figure 31 In-plane current distribution for different air stream relative humidities ($I=0.65 \text{ A/cm}^2$, $\text{RH}_a=0.4$, compression ratio=35%).

5.4.4 Effect of compression on liquid water formation

Transport ability of GDMs depends on their porosity values. Clamping force seen to reduce porosity and negatively influence the cell performance. Formation of liquid water is expected to have an additional detrimental impact on the cell performance by occupying the pore spaces. The liquid water saturation in the cathode GDM is shown in Figure 32 for two cases; one free from compression and one with compression.

The water in the cell is being removed by two mechanisms, namely, capillary flow and diffusion of vapor upon evaporation. Under the rib, a greater accumulation of water and a lesser availability of oxygen in the diffusion layer are expected since the reactants and products have to diffuse through a longer path across the width and the thickness of the diffusion layer. Additionally, under compression, the liquid water saturation under the rib intensifies due to the reduced porosity and permeability. In the compressed case, the liquid water saturation is slightly increased under the channel as well. However, this is in consequence of the elevated condensation rate at high current loads. Less saturated media is also detected in the MPL compared to GDL, illustrating the better water expelling characteristic of this hydrophobic layer which is beneficial for the diffusion of oxygen to the CL.

Locations of condensation and evaporation are also quantified and shown in Figure 32. Phase change rate is highly coupled with relative humidity of inlet gas stream and local distributions of temperature, and liquid water saturation. The phase change source term given in Table 3 allows supersaturation and undersaturation to take place, bringing about condensation and evaporation, respectively. The greater the deviation of water vapor pressure, P_g^{H2O} , from the saturated vapor pressure, P_{sat}^{H2O} , the higher the phase change rate. From the analyses, by applying compressive force, the supersaturation region shrinks in length under the channel and the undersaturation region extends under the rib. However, both of these regions become thicker under compression. As it is seen, the region in the vicinity of the CL and under the channel undergoes condensation. This observation is in agreement with the results of the

numerical study done by Basu et al. [37]. In their study, the condensation was mainly seen in CL and GDL adjacent to it (due to water production). They also observed that by increasing the relative humidity level on the cathode side the condensation zone extends from the area under the rib to the area under the channel.

A condensation zone is also observed in [37] in the cathode GDL adjacent to the rib area due to the contact with cooler surface. However, in our model, there is a little temperature variation in that region, most likely due to consideration of thermal-contact resistance at GDM-BP interface and assuming a constant temperature boundary condition at the BP outer edges. Temperature gradient is also seen to be negligible throughout the cell creating a relatively homogenous saturation pressure field.

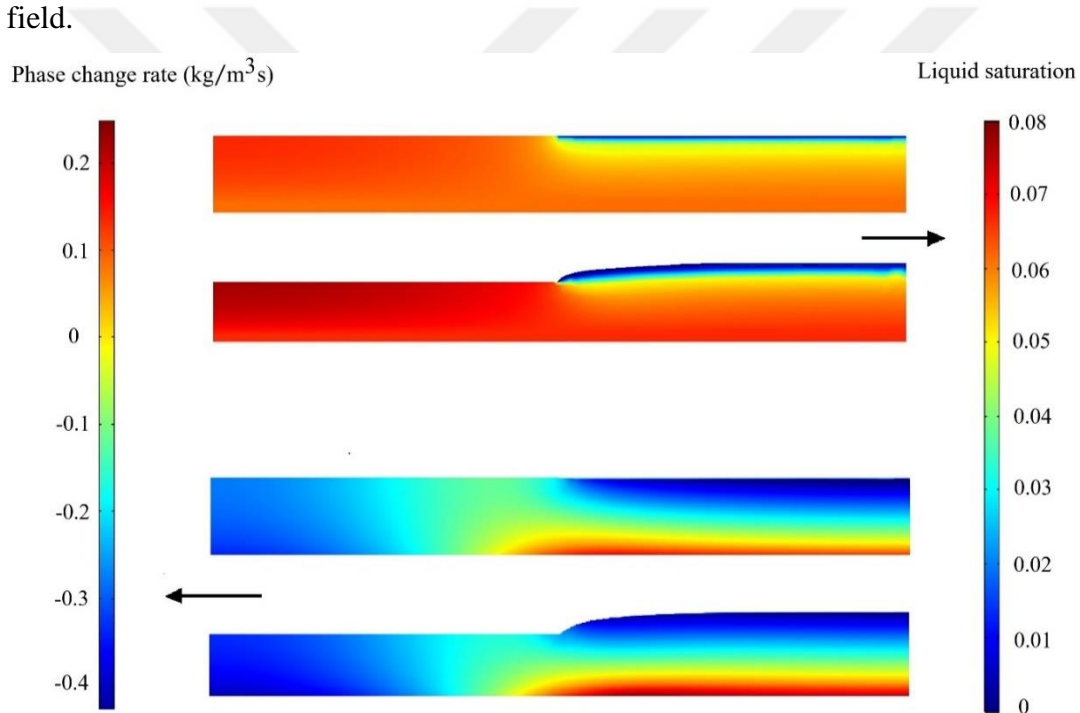


Figure 32 Compression effect on liquid water saturation and phase change rate distribution in cathode GDM ($I=0.75 \text{ A/cm}^2$, $RH_c=0.7$, $RH_a=0.4$, compression ratio=35%).

5.4.5 Effect of liquid water flooding on cell performance

Liquid water saturation in the cell increases with an increase in inlet relative humidity. This directly affects the transport ability of the porous media, resulting in subsequent reduction in limiting current density. To study the influence of activating the phase change process and evolution of liquid water in the cell, three different simulation cases are chosen which differ in the inlet relative humidity on the cathode; $RH_c = 0.6, 0.8, 1$. For each case, two different curves are extracted one with the phase change phenomena activated with accompanying liquid water generation and one free from phase change phenomena. Figure 33 illustrates the polarization curves obtained for those cases. Water flooding affects the slopes of the cell performance curves. At higher current densities, these slopes become much steeper due to higher magnitude of water production that greatly reduces the oxygen transport rate.

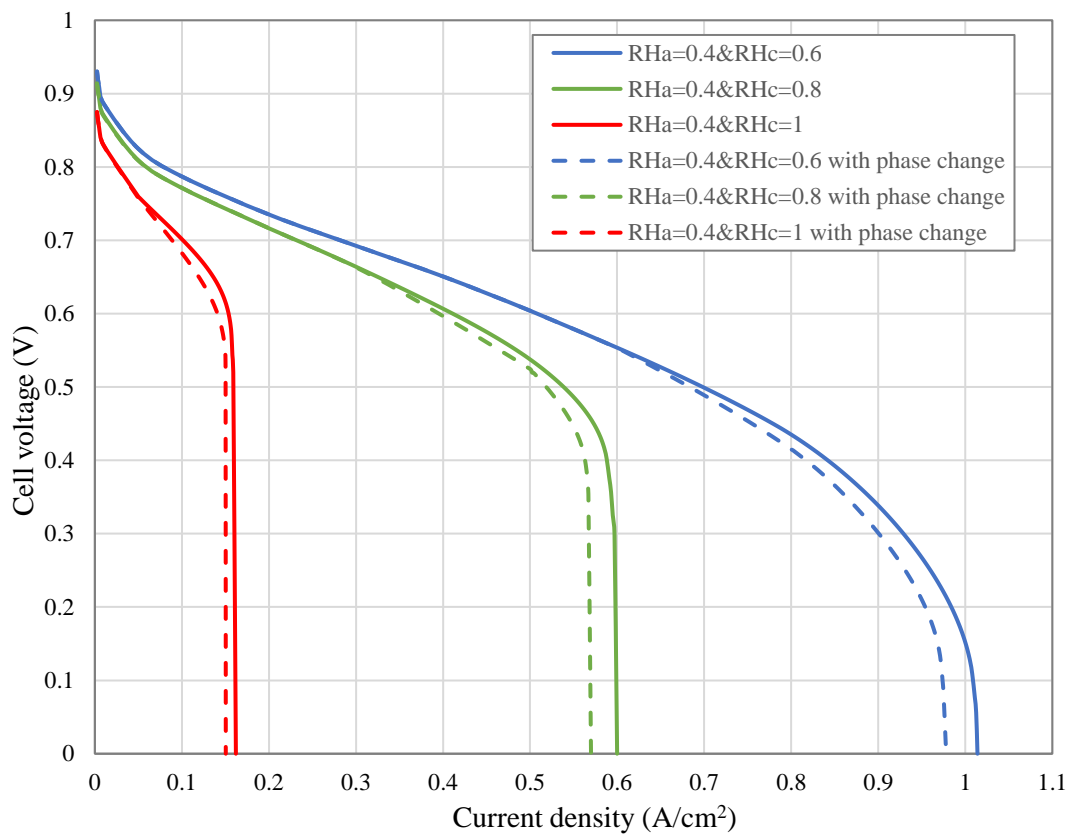


Figure 33 Liquid water generation effects on cell performance.

In the low current density range, kinetics and ohmic resistance dominate and the predicated performances by single phase and two phase models overlap. For higher current densities (close to concentration polarization range in the curve), the single-phase model overestimates the fuel cell performance compared to the two-phase model, with deviations from 4% to 8%.

This curve shows that ignoring the liquid water and its mass-transfer hindering effects predicts the diffusive gas transport rates more than the real value leading to high current densities which are practically not achievable.

5.5 Influence of operating parameters on membrane's local mechanical degradation

Operating conditions such as potential, temperature and relative humidity strongly influence the stress distribution in a PEFC which directly affects its durability. The stress concentration points localized at the membrane-GDL interface cause compression and tension on the microscopic level. When their effects are superimposed on the macro scale, cracks, pinholes and delamination are created in localized areas of MEA. Therefore, strain distribution along the membrane can be used as a key parameter to characterize the deformation behavior in the membrane and to find the potential sites for failure. In particular, compressive force due to clamping pressure, load current and anode and cathode relative humidity values are very important. In Table 8, cases considered in this study are summarized.

Table 8 Simulation cases for the analyses on the effect of different parameters on the mechanical degradation.

	case	Compression force (MPa)	Current load (A/cm ²)	Inlet relative humidity
Effect of clamping force	1	1	0.7	RH _a =0.4, RH _c =0.4
	2	4	0.7	RH _a =0.4, RH _c =0.4
	3	8	0.7	RH _a =0.4, RH _c =0.4
Effect of current load	4	1	0.1	RH _a =0.4, RH _c =0.4
	5	1	0.6	RH _a =0.4, RH _c =0.4
	6	1	1.2	RH _a =0.4, RH _c =0.4
Effect of inlet relative humidity	7	1	0.5	RH _a =0.4, RH _c =0.4
	8	1	0.5	RH _a =0.8, RH _c =0.4
	9	1	0.5	RH _a =0.4, RH _c =0.8

5.6 Effect of clamping force

Clamping force influences all components but particularly the GDL due to its lower Young's modulus. In order to obtain the swelling patterns of the membrane, effects of clamping force on the GDL deformation and water distribution must be taken into account. Volumetric contraction in the GDL changes the porosity and permeability and impedes the gas and liquid transport in the porous medium resulting in an increased mass transport resistance and concentration losses in the electrochemical performance of the cell. Local stress/strains in the membrane are calculated by our proposed model.

Based on the in-plane distribution of mechanically induced strains given in Figure 34(a), the most probable failure sites of the membrane are identified. According to the figure, while the portion of the membrane under the rib is mostly under compression, the portion under the channel is observed to be in tension. Under the clamping force, contraction is an expected behavior which mostly happens under the rib. However, this contraction does not damage the integrity of the membrane. The membrane integrity fails when the induced stress exceeds the local yield strength.

According to postmortem analyses of humidity cycled membranes, cracks and pinholes usually appears under the channel regions of the flow-field [54]. Local cavities in the membrane which eventually forms crazes are also the results of tensile stresses [61]. Therefore, the tensile stress is assumed to be the damaging factor for a membrane.

The application of clamping force results in a change in water distribution in GDL and equilibrium water content in the membrane, and in turn causing a change in swelling profile. With an increase in the clamping force, the local maxima for hygral strain move towards the region under the channel.

According to Figure 34(a) following observations are made on the effect of compression:

- Compression has a significant effect on the elastic strain.
- Thermal strains are insignificant.
- Hygral and plastic strains change with changing compressive force, while later being greater.
- Plastic strains decrease by increasing the compressive force under the rib.

By raising the compressive force, the magnitude of the total strain changes substantially. Under the rib, the magnitude of negative elastic strain increases as a result of the increased clamping force, whereas the elastic and plastic strains rise due to swelling under the channel. Both regions under the rib and under the channel experience tensile stresses in case 1. However, in cases 2 and 3, only the region under the channel experiences tensile stress. Plastic strain follows the total strain trend for all cases. Since the plastic deformation is sensitive to tensile stresses, increasing the clamping force decreases (increases) the total strain under the rib (under the channel) along with the elastic strain.

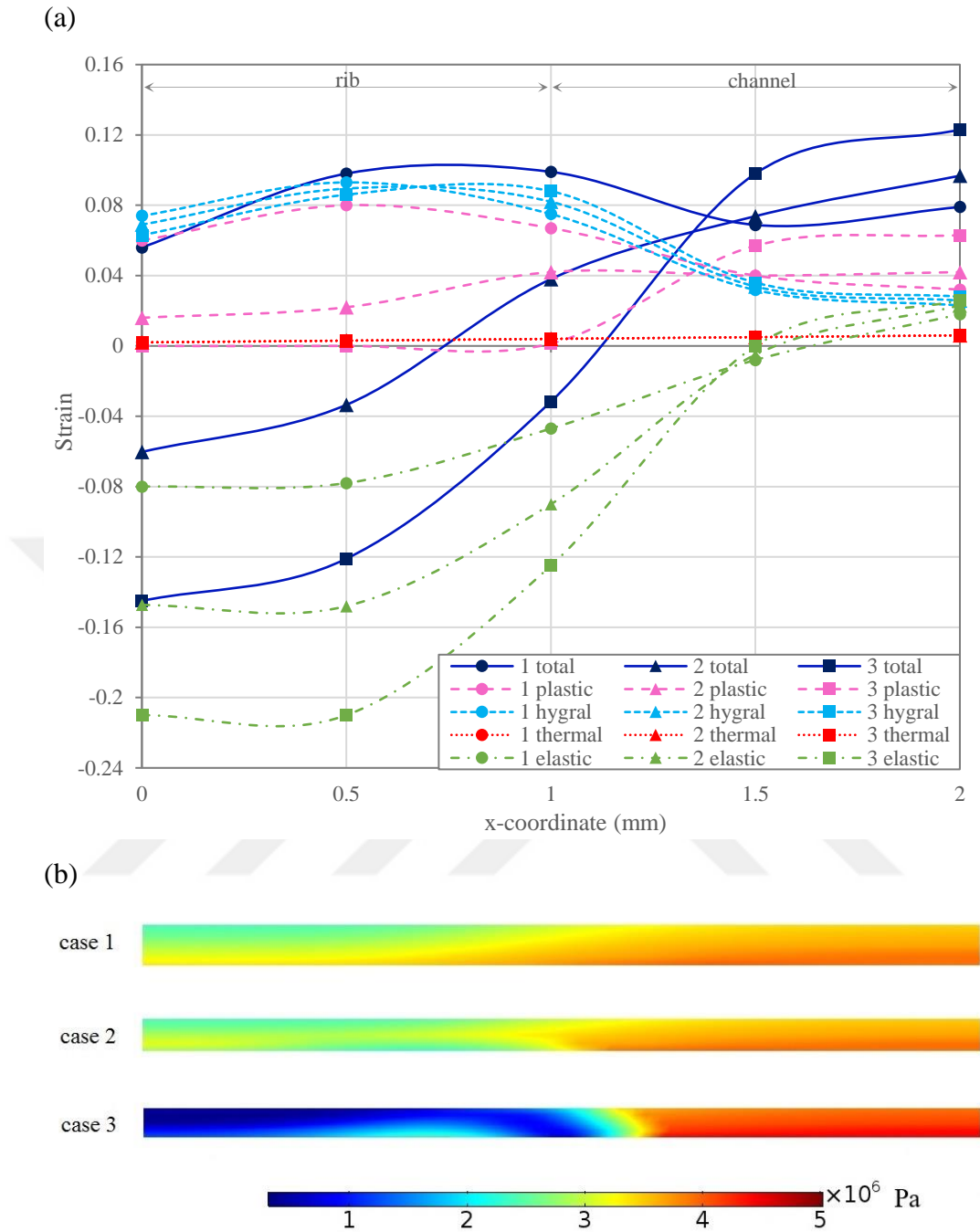


Figure 34 (a) Strain distribution along the membrane's interface with cathode and (b) von Mises stress distribution in the membrane for study cases 1-3.

For cases 1-3, distribution of the von Mises stress is shown in Figure 34(b), and the potential failure sites in the membrane can be identified where the von Mises stress becomes close to or exceeds the yield strength. Overall thickness of the membrane

decreases with increasing clamping force over the cell. Portion of the membrane under the rib is subject to compressive force and as the compression increases so does the magnitude of compressive strain in this region while the magnitude of tensile strain increases under the channel. Consequently, increasing compression leads to higher von Mises stresses under the channel almost as high as the yield stresses. Thus, the membrane defects are expected in this region.

5.7 Effect of the load current

Current density distribution has a strong influence on hygro-thermal stresses. Changes in load current induce non-uniform water distribution in the GDL and the membrane and cause hydration/dehydration in the membrane. As can be seen in Figure 35(a), local current density is maximum under the rib due to contact with the plates. However, this local current maximum shift towards the area under the channel due to mass transport resistance as the load current increases in the cell. This current maximum causes a sharp local elevation in temperature, humidity and stress.

Figure 35(b) illustrates the strain distributions along the membrane interface and the fraction each stress has on the total strain. In the cell, the inlet relative humidity in both anode and cathode are kept as 0.4, clamping force as 1 MPa, and the current density is varied between 0.05 and 1.2 A/cm²; cases 4 to 6 in Table 8 are representatives of low, medium and high load cases.

According to Figure 35(b) following observations can be made on the effects of load current:

- Load current has a significant effect on the hygral strain.
- By increasing the load current, the total strain maxima shift towards the region under the channel.
- Thermal strains are insignificant.
- Elastic strain is almost fixed during the change in load current.
- Plastic strain distribution depends on the hygral strain pattern over the membrane.

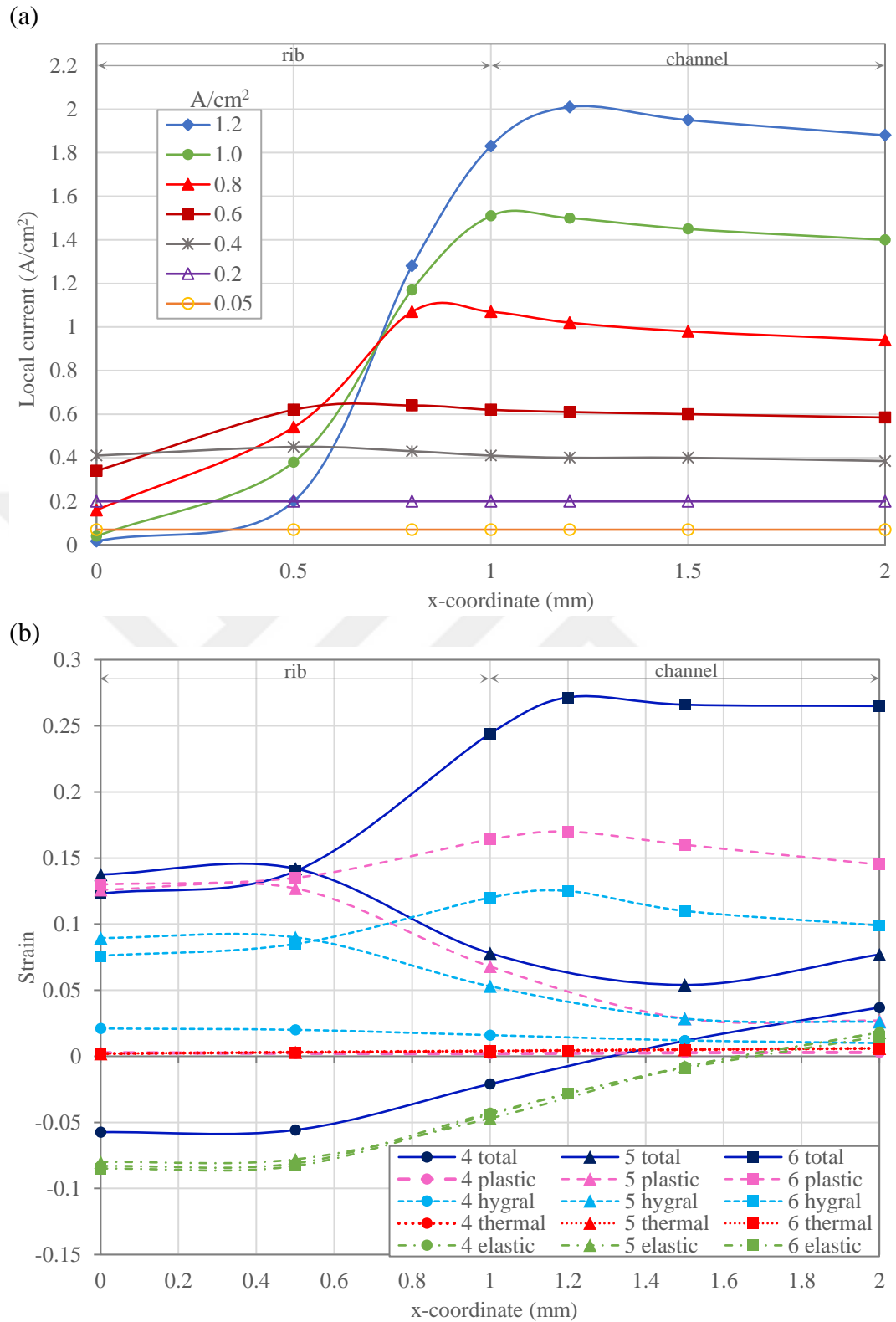


Figure 35 (a) Local current density distribution and (b) strain distribution along the membrane's interface with cathode for different operating current loads.

For low currents, negative strain in the membrane is observed under the rib indicating thinning in the membrane caused by the clamping force. The dominant in-plane stress state during cell operation is compressive under the rib and is tensile under the channel. However, in higher current loads the magnitude of hygral strain underneath the rib increases leading to total tensile stress in this region.

5.8 Effect of inlet relative humidity

The level of hydration in the membrane strongly affects its proton conductivity. While dry operating conditions degrade the membrane rapidly, high humidity conditions may lead to GDL flooding and block the diffusion of reacting gases. Water management has a great impact on cell durability besides its influence on PEFC performance. Water formation and its transport mechanisms within the cell have direct influences on membrane dissolution and creation of corrosion and morphological damages in MEA and GDL.

It is unlikely to have an equal saturation at the anode and the cathode in an operating fuel cell. While the cathode side is subject to hydration by water generation, anode side tends to dry-out due to electro-osmotic drag as the load current increases. Membrane tends to absorb water and swell at high relative humidities while it tends to desorb water and shrink at low relative humidities. Therefore, non-uniform distribution of water in the cell brings about different local stress/strain behaviors and causes subsequent mechanical failures in the membrane.

Here, one symmetric and two asymmetrical cases in the inlet relative humidity of the anode and cathode sides are simulated as shown in Table 8 (Cases 7-9). For collecting the simulation data in those figures, current load and compression force were fixed on 0.5 A/cm^2 and 1 MPa, respectively. The water distributions in the cell for these three cases along with the individual contributing factors on the strain over the membrane interfaces are shown in Figures 36-38.

Water concentration gradient across the membrane is expected when inlet relative humidity values at the anode and cathode are different. Major portion of the water

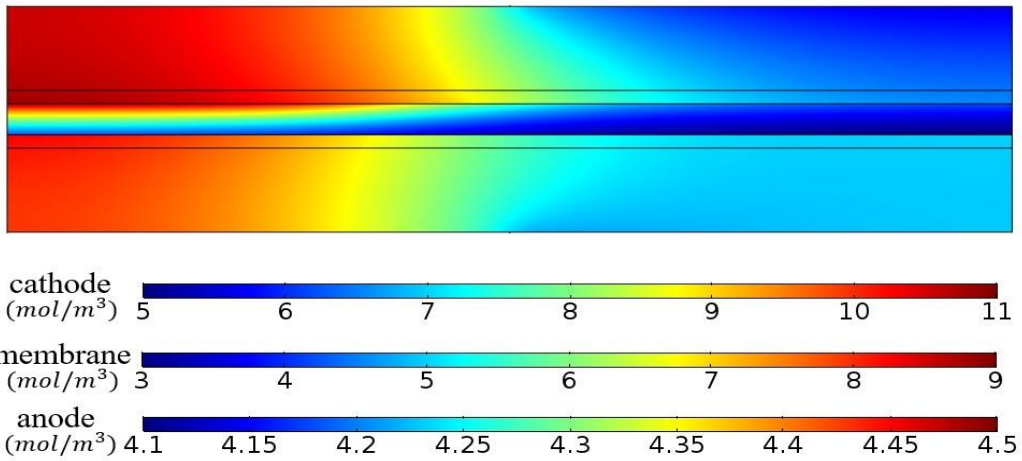
content spreads in locations close to the cathode in all of the three cases due to water generation at the cathode. However, the membrane experiences dehydration on the anode side due to electro-osmotic drag. These are the reasons why the cracks in the membrane occur mainly in the cathode side where it is subjected to higher relative humidity amplitudes. Therefore, more attention should be given to this region of the membrane from the durability point of view.

According to Figures 36-38 following conclusions can be drawn on the effects of inlet relative humidity:

- Inlet relative humidity has a significant impact on the hygral strain.
- While total strain maxima shift towards the region under the channel by increasing the inlet relative humidity in the cathode, this maxima shift towards the region under the rib by increasing the inlet relative humidity in the anode.
- Cathode side experiences higher strain magnitudes than the anode side.
- Thermal strains are insignificant.
- Elastic strain is almost fixed during the change in inlet relative humidities.
- Plastic strain distribution depends on the hygral strain pattern over the membrane.

Having raised the relative humidity to 80%, the magnitude of membrane hygroscopic swelling increased accordingly. Increase in the average current density produced over the interface due to higher membrane conductivity is the reason behind this effect. These effects are most considerable when relative humidity increases in the cathode side where the portion under the channel experiences a higher current generation than the portion under the rib. This is attributed to the fact that the porosity variation in the GDL under inhomogeneous clamping force becomes more significant when inlet relative humidity increases. Transport of reactant gases into the GDL under the rib section becomes more difficult, causing a lower current generation in this area, especially at high current loads

(a)



(b)

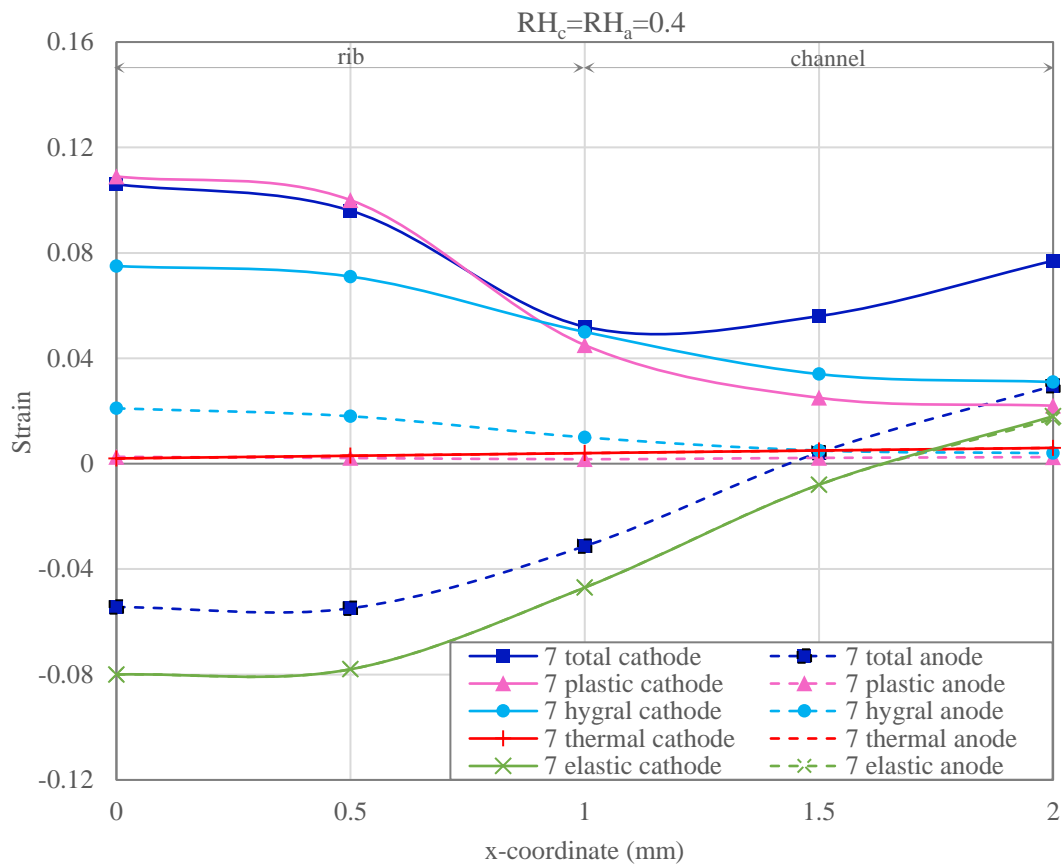


Figure 36 (a) Water distribution in the cell and (b) in-plane strain distribution along the membrane's interfaces with the cathode and anode for the study case 7.

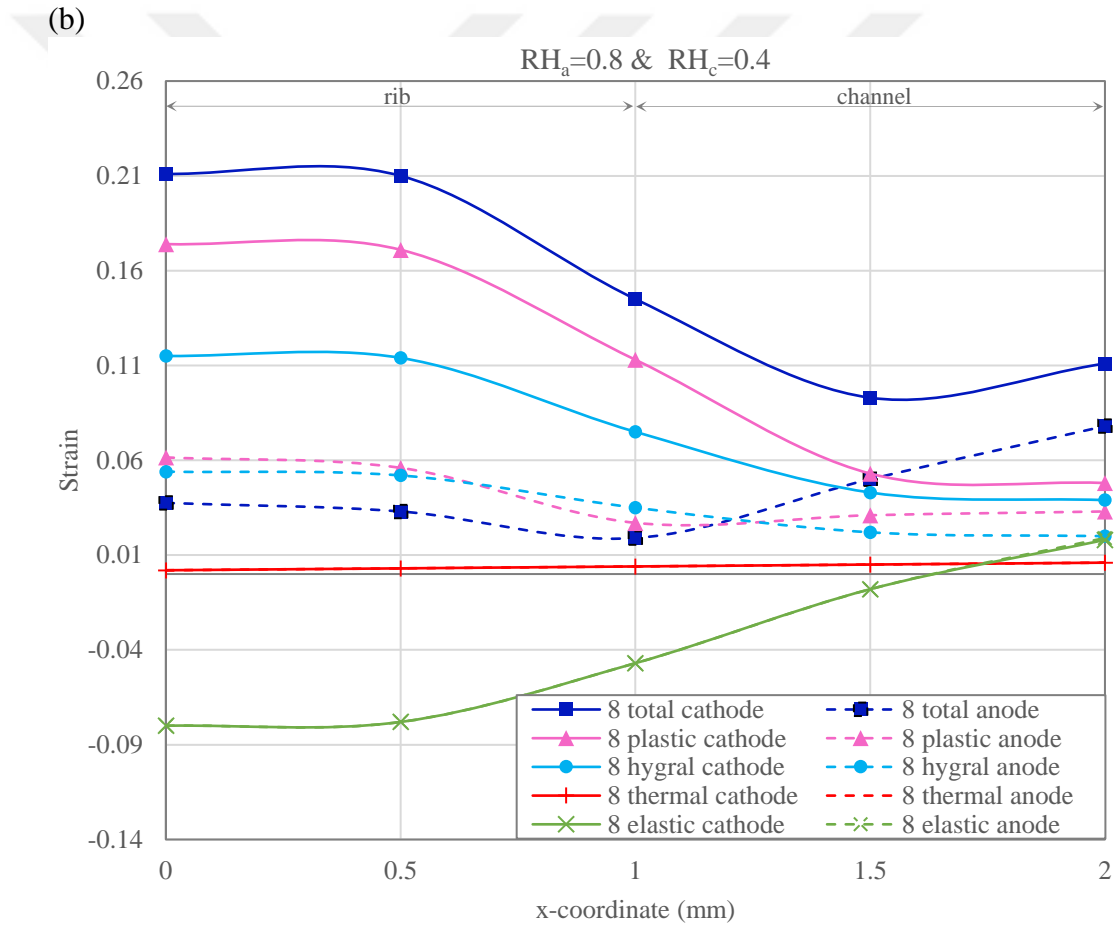
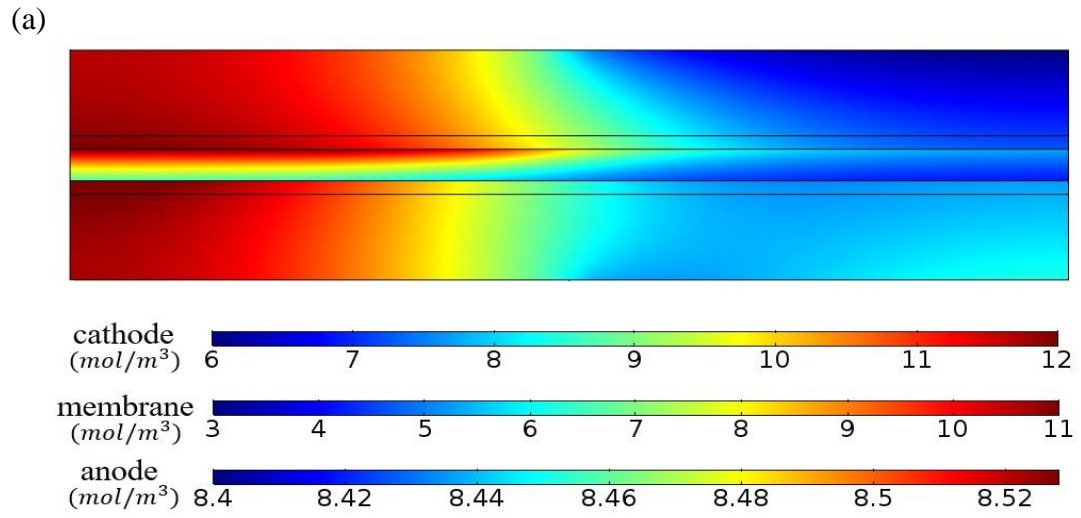


Figure 37 (a) Water distribution in the cell and (b) in-plane strain distribution along the membrane's interfaces with the cathode and anode for study case 8.

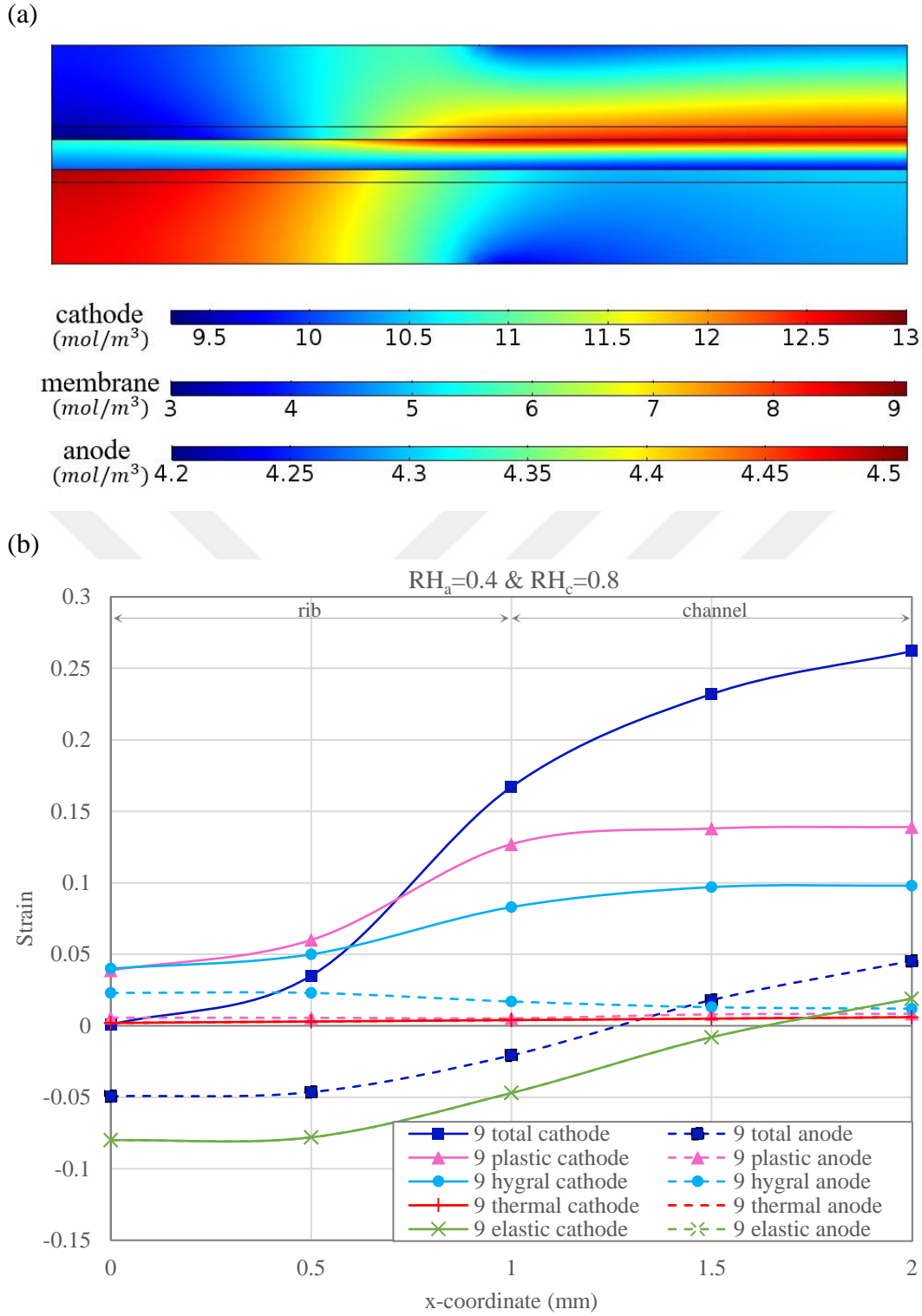


Figure 38 (a) Water distribution in the cell and (b) in-plane strain distribution along the membrane's interfaces with the cathode and anode for study case 9.

The simulation results show that hygral strain has the most deleterious effect on the strength of the membrane. The plastic deformation follows the hygroscopic swelling, because as the hygral strain increases, so does the plastic strain. At higher temperatures and humidities, the yield strength of the membrane decreases, which results in a higher magnitude of plastic strain. Under the channel, due to high tensile stresses the chances of creation and evolution of defects are high. These findings are compatible with the reported observations given in [61] from the actual humidity cycle tests.





CHAPTER 6

CONCLUSION

6.1 Concluding remarks

A fully coupled finite-element model is created to describe the charge and mass transport, electrochemical reactions, phase change phenomena, and structural deformations in PEFC. Impacts of mechanical force on the porosity, diffusivity, and permeability of the GDLs as well as contact resistances and their corresponding effects on cell performance are studied with numerical simulations. In order to validate the model, local current density distribution and polarization curves under compression are compared with the experimental measurements reported in [1,2].

The unique output of this study is the extensive predictions of local properties on channel-rib scale for various input parameters. It is found that the GDL properties can significantly affect the local features. Rib compression causes GDL property variations in the in-plane and through-plane directions, altering reactant gas and liquid water distributions. Lower porosity levels due to compression results in greater mass transfer resistance for both the reactants and the product water and hence inferior performance in the mass-transfer controlled regions. The connection between local current density and phase change rate is also established. Water generation escalates under the channel due to higher local current density values and brings about a condensation zone. Compression enhances the condensation rate by increasing mass transport towards the region under the channel with higher porosity and permeability values.

Inlet relative humidity is identified as a critical parameter over local current generation and overall cell performance. Under dry conditions, current is predominantly produced under the ribs, while the current shifts to the channel under humidified inlet conditions. Highly humidified inlet conditions in addition to acting clamping force intensifies the local current generation, condensation rate, and ensuing flooding under the channel. Therefore, these two key parameters should be rigorously adjusted to reach an efficiently operating cell, to that end, the present model can be used for predicting the behavior of PEFC.

A constitutive two-dimensional finite element model was developed to simulate the in-plane hygro-thermo-mechanically induced plane strain distributions in the membrane. Main objective of this work is to gain a better understanding of the membrane deformation and degradation due to stresses develop in various operating conditions. The swelling and mechanical property changes of the membrane and plastic deformations during hygrothermal cycles in the MEA were modelled, local stress distribution is obtained and the initiation of crazing is identified.

The relations between the operating conditions and cell degradation were analyzed. Strain distributions along the membrane surface were determined via numerical simulations of different applied clamping forces as well as load current and inlet relative humidity ratios. The findings manifest highly localized degradation. Having a low thermal expansion coefficient, membrane does not experience large thermal induced strains. In-plane current distribution found to have a great impact on the strain distribution over the channel/rib in the membrane. The simulation results revealed the hygroscopic induced strain/stress as the most important reason for membrane mechanical degradation. Unsymmetrical hydration cycling results in variations in the non-uniform deformations in the membrane. The failure location predominantly depends on operating conditions and fuel cell configurations. Locations that operate under lower compression and higher humidity and thermal loadings fail faster. These defects were localized and usually aligned along the channel edges.

The life of the membrane can be extended by reducing the hygro-thermo-mechanical stress/strains. Mitigating the mechanically induced degradation is a challenging task requiring a precise balance among different parameters. Different methods can be developed to reduce the mechanical degradation namely customizing the design strategies, adjusting the fuel cell operating conditions, and utilizing durable materials. Although low water content in the membrane has an adverse effect on the cell performance, it is plausible to operate the cell with low inlet relative humidity to minimize the deleterious effects of swelling. Another approach could be to keep the desired hydration level but fortify the MEA using composites or cross-linked polymers to withstand high levels of hygroscopically induced deteriorations. Regulating the inlet relative humidity and the load current transients would also alleviate the mechanical degradation. Studying both in-plane mechanical and through-plane stress/strain behavior employing careful fuel cell experiments would be helpful in developing modern membrane material that can meet the challenges of future operating demands. Further modeling and experimental studies are necessary to improve design and control of fuel cells to mitigate the adverse effects of hygral stresses.

6.2 Future work

Further analyses of the effects of rib on transport phenomena inside the GDLs are needed. This work can be extended into three dimensional configurations with time dependent properties. With that, the evolution of water and its impact over the cell performance as well as mechanical degradation during hygrothermal cycles can be determined.

It is recommended to model the GDL using pore-scale models. An approach to model the multiphase transport phenomena that is best suited with the pore-scale modeling would be to use Lattice Boltzmann Method (LBM). These approaches can be implemented on specific components and locations of the cell and then combined with the current continuum model to reach more accurate results.



REFERENCES

- [1] Reum M., Freunberger S.A., Wokaun A., Büchi F.N., “Measuring the current distribution with sub-millimeter resolution in PEFCs II. Impact of operating parameters,” *J. Electrochem. Soc.* 156(3) (2009) B301–10.
- [2] Reum M., “Sub-millimeter resolved measurement of current density and membrane resistance in polymer electrolyte fuel cells,” Ph.D. Dissertation 2008, Swiss Federal Institute of Technology; Zürich, Switzerland.
- [3] Udell K., “Heat-transfer in porous-media considering phase change and capillarity – the heat pipe effect,” *Int. J. Heat and Mass Transf.* 28(2) (1985) 485–95.
- [4] Bergman T.L., Lavine A.S., Incropera F.P., Dewitt D.P., “Fundamentals of heat and mass transfer,” 7th ed. John Wiley & Sons Inc. (2011).
- [5] Flückiger R., Freunberger S.A., Kramer D., Wokaun A., Scherer G.G., Büchi F.N., “Anisotropic, effective diffusivity of porous gas diffusion layer materials for PEFC,” *Electrochim. Acta.* 54 (2008) 551–9.
- [6] Ismail M.S., Ingham D.B., Hughes K.J., Ma L., Pourkashanian M., “Effective diffusivity of polymer electrolyte fuel cell gas diffusion layers: an overview and numerical study,” *Int. J. Hydrogen Energy* 40 (2015) 10994–1010.
- [7] Nam J.H., Kaviany M., “Effective diffusivity and watersaturation distribution in single-and two-layer PEMFC diffusion medium,” *Int. J. Heat Mass Trans.* 46 (2003) 4595–611.
- [8] Zamel N., Li X., Shen J., “Correlation for the effective gas diffusion coefficient in carbon paper diffusion media,” *Energy Fuels* 23 (2009) 6070–8.
- [9] Unsworth G., Dong L., Li X., “Improved experimental method for measuring gas diffusivity through thin porous media,” *AIChE J.* 59 (2013) 1409–19.

- [10] Kramer D., Freunberger S.A., Flückiger R, Schneider IA, Wokaun A, Büchi FN, et al., “Electrochemical diffusimetry of fuel cell gas diffusion layers,” *J. Electroanal. Chem.* 612 (2008) 63–77.
- [11] Becker J., Flückiger R., Reum M., Büchi F.N., Marone F., Stampanoni M., “Determination of material properties of gas diffusion layers: experiments and simulations using phase contrast tomographic microscopy,” *J. Electrochem. Soc.* 156 (2009) 1175–81.
- [12] Hwang G.S., Weber A.Z., “Effective-diffusivity measurement of partially-saturated fuel-cell gas-diffusion layers,” *J. Electrochem. Soc.* 159 (2012) 683–92.
- [13] Rosen T., Eller J., Kang J., Prasianakis N.I., Mantzaras J., Büchi FN., “Saturation dependent effective transport properties of PEFC gas diffusion layers,” *J. Electrochem. Soc.* 159 (2012) 536–44.
- [14] Wu R., Zhu X., Liao Q., Wang H., Ding Y.D., Li J., et al., “Determination of oxygen effective diffusivity in porous gas diffusion layer using a three-dimensional pore network model,” *Electrochim Acta* 55 (2010) 7394–403.
- [15] Gostick J.T., “Random pore network modeling of fibrous PEMFC gas diffusion media using Voronoi and Delaunay tessellations,” *J. Electrochem. Soc.* 160 (2013) 731–43.
- [16] Zhang X.M., Zhang X.X., “Impact of compression on effective thermal conductivity and diffusion coefficient of Woven gas diffusion layers in polymer electrolyte fuel cells,” *Fuel Cells* 14 (2014) 303–11.
- [17] Bruggeman D., “Calculation of various physics constants in heterogeneous substances I. Dielectricity constants and conductivity of mixed bodies from isotropic substances,” *Annalen der Physik* 24 (1935) 636–64.
- [18] Tomadakis M.M., Sotirchos S.V., “Ordinary and transition regime diffusion in random fiber structures,” *AIChE J.* 39 (1993) 397-412.

- [19] Cindrella L., Kannan A.M., Lin J.F., Saminathan K., Ho Y., Lin C.W., Wertz J., “Gas diffusion layer for proton exchange membrane fuel cells—a review,” *J. Power Sources* 194(1) (2009) 146–60.
- [20] Bazylak A., Sinton D., Liu Z., Djilali N., “Effect of compression on liquid water transport and microstructure of PEMFC gas diffusion layers,” *J. Power Sources* 163(2) (2007) 784–92.
- [21] Zhou P., Wu C.W., Ma G.J., “Influence of clamping force on the performance of PEMFCs,” *J. Power Sources* 163 (2007) 874–81.
- [22] Hottinen T., Himanen O., Karvonen S., Nitta I., “Inhomogeneous compression of PEMFC gas diffusion layer: part II. Modeling the effect,” *J. Power Sources* 171 (2007) 113–21.
- [23] Nitta I., Karvonen S., Himanen O., Mikkola M., “Modelling the effect of inhomogeneous compression of GDL on local transport phenomena in a PEM fuel cell,” *Fuel Cells* 8 (2008) 410–21.
- [24] Su Z.Y., Liu C.T., Chang H.P., Li C.H., Huang K.J., Sui P.C., “A numerical investigation of the effects of compression force on PEM fuel cell performance,” *J. Power Sources* 183 (2008) 182–92.
- [25] Zhou Y., Lin G., Shih A.J., Hu S.J., “Multi-physics modeling of assembly pressure effects on PEM fuel cell performance,” *J. Fuel Cell Sci. Technol.* 6 (2009) 1–7. 041005.
- [26] Li H., Tang Y., Wang Z., Shi Z., Wu S., Song D., et al., “A review of water flooding issues in the proton exchange membrane fuel cell,” *J. Power Sources* 178(1) (2008) 103–17.
- [27] Berning T., Djilali N., “A 3D, multiphase, multicomponent model of the cathode and anode of a PEM fuel cell,” *J. Electrochem. Soc.* 150(12) (2003) A1589–98.

- [28] Pasaogullari U., Wang C.Y., Chen K.S., “Two-phase transport in polymer electrolyte fuel cells with bilayer cathode gas diffusion media,” *J. Electrochem. Soc.* 152(8) (2005) A1574–82.
- [29] Tang Y., Santare M.H., Karlsson A.M., Cleghorn S., Johnson W.B., “Stresses in proton exchange membranes due to hygro-thermal loading,” *J. Fuel Cell Sci. Technol.* 3(2) (2006) 119–24.
- [30] Kusoglu A., Karlsson A.M., Santare M., Cleghorn S., Johnson W.B., “Mechanical behavior of fuel cell membranes under humidity cycles and effect of swelling anisotropy on the fatigue stresses,” *J. Power Sources* 170 (2007) 345–58.
- [31] Wang C.Y., Cheng P.A., “Multiphase mixture model for multiphase, multicomponent transport in capillary porous media I. Model development,” *Int. J. Heat Mass Transfer* 39(17) (1996) 3607–18.
- [32] Wang Y., Wang C.Y., “A non-isothermal, two-phase model for polymer electrolyte fuel cells,” *J. Electrochem. Soc.* 153(6) (2006) A1193–200.
- [33] He W., Yi J.S., Nguyen T.V., “Two-phase flow model of the cathode of PEM fuel cells using interdigitated flow fields,” *AIChE J.* 46 (2000) 2053–64.
- [34] Natarajan D., Nguyen T.V., “A two-dimensional, two-phase, multicomponent, transient model for the cathode of a proton exchange membrane fuel cell using conventional gas distributors,” *J. Electrochem. Soc.* 148(12) (2001) A1324–35.
- [35] Lin G., He W., Nguyen T.V., “Modeling liquid water effects in the gas diffusion and catalyst layers of the cathode of a PEM fuel cell,” *J. Electrochem. Soc.* 151(12) (2004) 1999–2006.
- [36] Ye Q., Nguyen T.V., “Three-dimensional simulation of liquid water distribution in a PEMFC with experimentally measured capillary functions,” *J. Electrochem. Soc.* 154(12) (2007) B1242–51.

- [37] Basu S., Wang C.W., Chen K.S., “Phase change in a polymer electrolyte fuel cell,” *J. Electrochem. Soc.* 156(6) 2009 B748–56.
- [38] Ihonen J., Mikkola M., Lindbergh G., “Flooding of gas diffusion backing in PEFCs: physical and electrochemical characterization,” *J. Electrochem. Soc.* 151 (2004) A1152–61.
- [39] Zhou P., Wu C., “Numerical study on the compression effect of gas diffusion layer on PEMFC performance,” *J. Power Sources* 170(1) (2007) 93–100.
- [40] Shi Z., Wang X., Guessous L., “Effect of compression on the water management of a proton exchange membrane fuel cell with different gas diffusion layers,” *J. Fuel Cell Sci. Technol.* 7 (2010) 1–7. 021012.
- [41] Yoon W., Huang X., “A multiphysics model of PEM fuel cell incorporating the cell compression effects,” *J. Electrochem. Soc.* 157 (2010) B680–90.
- [42] Wang Y., Chen K.S., “Effect of spatially-varying GDL properties and land compression on water distribution in PEM fuel cells,” *J. Electrochem. Soc.* 158(11) (2011) B1292–9.
- [43] Olesen A.C., Berning T., Kaer S.K., “The effect of inhomogenous compression on water transport in the cathode of a proton exchange membrane fuel cell,” *J. Fuel Cell Sci. Technol.* 9 (2012) 1–7. 031010.
- [44] Chippar P., Kyeongmin O., Kang K., Ju H., “A numerical investigation of the effects of GDL compression and intrusion in polymer electrolyte fuel cells (PEFCs),” *Int. J. Hydrogen Energy* 37 (2012) 6326–38.
- [45] Tranter T.G., Burns A.D., Ingham D.B., Pourkashanian M., “The effects of compression on single and multiphase flow in a model polymer electrolyte membrane fuel cell gas diffusion layer,” *Int. J. Hydrogen Energy* 40(1) (2015) 652–64.

- [46] Schulz V.P., Becker J., Wiegmann A., Mukherjee P.P., Wang C.Y., “Modeling of two-phase behavior in the gas diffusion medium of PEFCs via full morphology approach,” *J. Electrochem. Soc.* 154(4) (2007) B419–26.
- [47] Mukherjee P.P., Wang C.Y., Kang Q.J., “Mesoscopic modeling of two-phase behavior and flooding phenomena in polymer electrolyte fuel cells,” *Electrochim. Acta* 54(27) (2009) 6861–75.
- [48] Fazeli M., Hinebaugh J., Fishman Z., Tötze C., Lehnert W., Manke I., Bazylak A., “Pore network modeling to explore the effects of compression on multiphase transport in polymer electrolyte membrane fuel cell gas diffusion layers,” *J. Power Sources* 335 (2016) 162–71.
- [49] Li J., Wang C.W., Su A., “Prediction and experimental validation of in-plane current distribution between channel and land in a PEFC,” *J. Electrochem. Soc.* 155 (2008) B64–9.
- [50] Freunberger S.A., Reum M., Evertz J., Wokaun A., Büchi F.N., “Measuring the current distribution in PEFCs with submillimeter resolution,” *J. Electrochem. Soc.* 153(11) (2006) A2158–65.
- [51] Kusoglu A., Weber A.Z., “New insights into perfluorinated sulfonic-acid ionomers,” *Chem. Rev.* 117 (2017) 987–1104.
- [52] Jahnke T., Futter G., Latz A., Malkow T., Papakonstantinou G., Tsotridis G., Schott P., Gerard M., Quinaud M., Quiroga A., Franco M., Malek K., Calle-vallejo F., Ferreira de Morais T., Kerber R., Sautet P., Loffreda D., Strahl S., Serra M., Polverino P., Pianese C., Mayur M., Bessler W., Kompis C., “Performance and degradation of proton exchange membrane fuel cells: state of the art in modeling from atomistic to system scale,” *J. Power Sources* 304 (2016) 207–33.
- [53] Kusoglu A., Weber A.Z., “Electrochemical/mechanical coupling in ion-conducting soft matter,” *J. Phys. Chem. Lett.* 6 (2015) 4547–52.

- [54] Gittleman C.S., Coms F.D., Lai Y.-H., “Membrane durability: physical and chemical degradation, in: M. Mench, E.C. Kumbur, T.N. Veziroglu (Eds.),” *Polymer Electrolyte Fuel Cell Degradation*, Elsevier Inc., 2012, pp. 15–88.
- [55] Wu J., Yuan X.Z., Martin J.J., Wang H., Zhang J., Shen J., Wu S., Merida W., “A review of PEM fuel cell durability: Degradation mechanisms and mitigation strategies,” *J. Power Sources* 184 (1) (2008) 104–19.
- [56] Weber A.Z., Newman J., “A theoretical study of membrane constraint in polymer-electrolyte fuel cells,” *AIChE J.* 50 (12) (2004) 3215–26.
- [57] Kusoglu A., Karlsson A.M., Santare M.H., Cleghorn S., Johnson W.B., “Mechanical response of fuel cell membranes subjected to a hygro-thermal cycle,” *J. Power Sources* 161 (2006) 987–96.
- [58] Tang Y., Karlsson A.M., Santare M.H., Gilbert M., Cleghorn S., Johnson W.B., “An experimental investigation of humidity and temperature effects on the mechanical properties of perfluorosulfonic acid membrane,” *Mater. Sci. Eng.* 425 (2006) 297–304.
- [59] Bograchev D., Gueguen M., Grandidier J.C., Martemianov S., “Stress and plastic deformation of MEA in running fuel cell,” *Int. J. Hydrogen Energy* 32 (2008) 5703–17.
- [60] Kusoglu A., Santare M.H., Karlsson A.M., Cleghorn S., Johnson W.B., “Numerical investigation of mechanical durability in polymer electrolyte membrane fuel cells,” *J. Electrochem. Soc.* 157 (2010) B705–13.
- [61] Kusoglu A., Santare M.H., Karlsson A.M., “Aspects of fatigue failure mechanisms in polymer fuel cell membranes,” *J. Polym. Sci. Part. B Polym. Phys.* 49 (2011) 1506–17.

- [62] Khattra N.S., Karlsson A.M., Santare M.H., Walsh P., Busby F.C., “Effect of time-dependent material properties on the mechanical behavior of PFSA membranes subjected to humidity cycling,” *J. Power Sources* 214 (2012) 365–76.
- [63] Silberstein M.N., Boyce M.C., “Constitutive modeling of the rate, temperature, and hydration dependent deformation response of Nafion to monotonic and cyclic loading,” *J. Power Sources* 195 (2010) 5692–706.
- [64] Silberstein M.N., Boyce M.C., “Hygro-thermal mechanical behavior of Nafion during constrained swelling,” *J. Power Sources* 196 (7) (2011) 3452–60.
- [65] Vengatesan S., Fowler M.W., Yuan X.-Z., Wang H., “Diagnosis of MEA degradation under accelerated relative humidity cycling,” *J. Power Sources* 196 (11) (2011) 5045–52.
- [66] Kreitmeier S., Schuler G.A., Wokaun A., Büchi F.N., “Investigation of membrane degradation in polymer electrolyte fuel cells using local gas permeation analysis,” *J. Power Sources* 212 (2012) 139–47.
- [67] Al-Baghdadi M.A.R.S., “A CFD study of hygro-thermal stresses distribution in PEM fuel cell during regular cell operation,” *Renewable Energy* 34 (2009) 674–82.
- [68] Yesilyurt S., “Modeling and simulations of PEM fuel cells with poroelastic approach for coupled liquid water transport and deformation in the membrane,” *J. Fuel Cell Sci. Technol.* 7(3) (2010) 1–7. 031008.
- [69] Serincan M.F., Pasaogullari U., “Mechanical behavior of the membrane during the polymer electrolyte fuel cell operation,” *J. Power Sources* 196 (2011) 1303–13.
- [70] Verma A., Pitchumani R., “Influence of transient operating parameters on the mechanical behavior of fuel cells,” *Int. J. Hydrogen Energy* 40 (2015) 8442–53.

[71] Ul Hassan N., Kilic M., Okumus E., Tunaboylu B., Soydan A.M., “Experimental determination of optimal clamping torque for AB-PEM fuel cell,” *J. Electrochem. Sci. Eng.* 6 (2016) 9–16.

[72] Bird R.B., Stewart W.E., Lightfoot E.N., “Transport Phenomena,” 2nd ed. New York: Wiley; 2002.

[73] Springer T.E., Zawodzinski T.A., Gottesfeld S., “Polymer electrolyte fuel cell model,” *J. Electrochem. Soc.* 138(8) (1991) 2334–42.

[74] Eikerling M., Kharkats Y.I., Kornyshev A.A., Volkovich Y.M., “Phenomenological theory of electro-osmotic effect and water management in polymer electrolyte proton-conducting membranes,” *J. Electrochem. Soc.* 145(8) (1998) 2684–99.

[75] Ge S., Li X., Yi B., Hsing I.M., “Absorption, desorption, and transport of water in polymer electrolyte membranes for fuel cells,” *J. Electrochem. Soc.* 152 (6) (2005) 1149–57.

[76] Leverett M., “Capillary behavior in porous solids,” *Trans. Am. Inst. Min. Metall. Pet. Eng.* 142 (1941) 152–69.

[77] Akiki T., Charon W., Iltchev M., Accary G., Kouta R., “Influence of local porosity and local permeability on the performances of a polymer electrolyte membrane fuel cell,” *J. Power Sources* 195 (2010) 5258–68.

[78] Hill R., “The Mathematical Theory of Plasticity,” Clarendon Press, Oxford, 1950.



CURRICULUM VITAE

PERSONAL INFORMATION

Surname, Name: Mehrtash, Mehdi
Nationality: Iranian
Date of Birth: 1 May 1985
Email: mehdi.mehrtash@metu.edu.tr
Phone: +90 553 094 4005

EDUCATION

Degree	Institution	Year of Graduation
MS	METU Mechanical Engineering	2011
BS	Urmia University	2008
High school	National Organization for Development of Exceptional Talents (NODET)	2003

WORK EXPERIENCE

Year	Place	Enrollment
2012-2016	TUBITAK	Research Fellow
2013	University of Nevada, Reno	Research Assistant
2007-2008	Kia Ehsan Industrial Group	Assistant Production Manager

PUBLICATIONS

Mehrtash, M., Tari, I., Yesilyurt, S., “Numerical modeling of visco-elasto-plastic hygro-thermal stresses and the effects of operating conditions on the mechanical degradation of PEFC membranes,” *Journal of Power Sources* (2017) Under review.

Mehrtash, M., Tari, I., Yesilyurt, S., “Impacts of inhomogeneous clamping force on local performance and liquid water formation in polymer electrolyte fuel cells,” *International Journal of Hydrogen Energy* 42(30) (2017) 19227-19245.

Tari, I., **Mehrtash, M.**, “Natural convection heat transfer from inclined plate-fin heat sinks,” *International Journal of Heat and Mass Transfer* 56 (2013) 574-593.

Mehrtash, M., Tari, I., “A correlation for natural convection heat transfer from inclined plate-finned heat sinks,” *Applied Thermal Engineering* 51 (2013) 1067-1075.

Tari, I., **Mehrtash, M.**, “Natural convection heat transfer from horizontal and slightly inclined from horizontal plate-fin heat sinks,” Applied Thermal Engineering 61 (2013) 728-736.

Mehrtash, M., Tari, I., “Dikey ve eğimli Yüzeyle yerleştirilmiş dikdörtgen kesitli kanatçıklı ısı atıcıların doğal taşınım için sayısal incelenmesi,” 18th National Conference on Thermal Sciences (ULIBTK), Zonguldak, Turkey, September 2011.

Mehrtash, M., Pesteei, M., “Heat transfer and flow structure around square-finned circular cylinder,” National Conference of Mechanical Engineering (NCME), Khomeinishahr, Iran, November 2008.

WORKSHOPS

Prof. Dr. T. Nejat Veziroglu Clean Energy Research Center 08/07/2016 – 13/08/2016
Nigde Omer Halisdemir University, Nigde, Turkey

Micro/Nanoscale Heat Transfer Course 07/07/2014 – 11/07/2014
Sabanci University, Istanbul, Turkey

LAMMPS Molecular Dynamics Simulator Workshop 06/08/2013 – 08/08/2013
Sandia National Laboratory, Albuquerque, NM, USA

TECHNICAL SKILLS

Programming C (advanced), Matlab (intermediate), Mathcad (intermediate)

Software Fluent (advanced), Fluent-UDF (intermediate), COMSOL Multiphysics (advanced), Icepak (advanced), ANSYS (intermediate), SolidWorks (intermediate), Tecplot

Others Soft-lithography for the fabrication of microfluidic devices

LANGUAGES

Persian, Azerbaijani, Turkish, English